Space Webs

Final Report

Authors: Gunnar Tibert, Mattias Gärdsback
Affiliation: KTH Engineering Sciences, Royal Institute of Technology,
SE-10044 Stockholm, Sweden

ESA Research Fellow/Technical Officer: Dario Izzo

Contacts:

Gunnar Tibert
Tel: +46(0)8 790 7961
Fax: +46(0)8 796 9850
e-mail: tibert@kth.se

Dario Izzo
Tel: +31(0)71 565 3511
Fax: +31(0)71 565 8018
e-mail: act@esa.int

Ariadna ID: 05/4109
Study Duration: 4 months
Contract Number: 19702/06/NL/HE

Available on the ACT website
http://www.esa.int/act

Abstract

This report presents a study of the controlled deployment of a large web in space. The study is composed of three major parts:

1. The design of the space web starts with a study of different geometries, i.e. three or four corners. For each geometry, three different mesh topologies are investigated, i.e. triangular, square or hexagonal meshes. An analysis by the force method showed that only the web with a square mesh could be prestressed by a centrifugal force field. The triangular mesh had a too high degree of static indeterminacy, which resulted in compressed elements. The hexagonal mesh had a too high degree of kinematic indeterminacy and became too distorted under the centrifugal force field. The square mesh webs were subsequently analysed in terms of out-of-plane flexibility and vibrational characteristics. Preliminary investigations on the choice of material for the web and the probability of web failure due to micro-meteoroid impact were also performed. MATLAB routines that automatically generates the web with an arbitrary size, mesh width and sag-to-span ratio have been developed.

2. A successful deployment requires an adequate folding pattern. A literature review identified the star-like folding pattern as a promising candidate. The folding is performed in two distinctive stages. First, the web is folded towards the central hub in a way so that three or four radial arms are formed, depending on the chosen geometry. Then, the radial arms can be either coiled around the central hub or folded in a zig-zag manner towards the hub. The MATLAB-generated web from part 1 is fed into new MATLAB routines, which folds the web according to the various pattern described above.

3. The dynamic deployment of the space web is analysed by a two-dimensional analytical model in MATLAB and a full three-dimensional model by the commercial finite element software LS-DYNA. The developed analytical models can simulate the deployment of the arms from a position coiled around the hub or reeled up on spools. A simple control strategy was found in literature and implemented in the analytical model with successful results. The MATLAB-generated model of the folded web was inserted into the software LS-DYNA. For an uncontrolled deployment, the finite element model yields the expected coiling off-coiling on oscillating behaviour. The control law with the drooping characteristics is not implemented in the finite

element model, but analyses with a simplified control law shows good agreement between the analytical and the finite element results for the deployment of the star arms.

Contents

List of Symbols and Abbreviations

Roman Symbols

A_{ca}	Cable area, p. 63
A_d	Cross-sectional area of strand, p. 24
A_{sw}	Area of space web, p. 15
b	Number of elements, p. 17
c	Number of kinematic constraints, p. 17
d_c	Distance between parallel web elements, p. 25
E_{ca}	Young's modulus for cable material, p. 63
$\mathcal{E}$	Kinetic energy, p. 52
$\boldsymbol{F}$	Applied force, p. 55
g	Gravitational acceleration (9.80665 m/s^2), p. 12
H	Total length of star arm, p. 56
h	Membrane thickness, p. 23
j	Number of nodes, p. 17
J_z	Moment of inertia of the centre hub, p. 54
ℓ	Length of interior web members, p. 18
L	Deployed length, p. 55
l	Length to mass dm, p. 55
$\boldsymbol{\mathcal{L}}$	Angular momentum, p. 50
M	Applied momentum, p. 54

m	Number of mechanisms, p. 17
m_c	Mass at web corner, p. 22
m_h	Mass of the hub, p. 50
m_p	Particle mass that will just break a cable, p. 36
m_w	Total mass of space web, p. 50
N	Tensile force in tether, p. 54
n	Number of corners in space web, p. 15
n	Number of radial tethers, p. 54
N_f	Number of fractures per unit length and unit time, p. 36
N_p	Micro-meteoroid flux, p. 35
$\boldsymbol{p}$	Vector of consistent nodal loads, p. 19
P_f	Failure probability due to micro-meteoroids, p. 37
$\boldsymbol{q}$	Vector of membrane stresses (N/m), p. 19
R	Radius of edge tether, p. 14
r_0	Radius of central hub, p. 22
$\ddot{\boldsymbol{R}}$	Acceleration of point mass, p. 55
ρ_{ca}	Cable density, p. 63
r_m	Radius of circular membrane, p. 22
S	Side length of space web, p. 14
s	Number of states of self-stress, p. 17
S_{et}	Total length of edge tethers, p. 16
S_{rt}	Total length of radial tethers, p. 16
t_{int}	Force in interior web elements, p. 19
x, y, z	Cartesian coordinates, p. 20

Greek Symbols

Δ	Half the distance between fold lines, p. 45

μ	Mesh topology parameter, p. 17
ω	Angular velocity, p. 22
φ	Deflection angle of tether, p. 55
ψ	Angle between tether and symmetry line, p. 23
ρ	Density, p. 12
ρ_A	Surface density, p. 56
ρ_d	Density of strand, p. 24
ρ_L	Line density, p. 55
ϱ	Sag-to-span ratio of edge tether, p. 15
$\varrho_{\max}$	Maximum sag-to-span ratio of edge tether, p. 16
σ_u	Ultimate strength, p. 12
Btheta	Angle between folds along the centre line, p. 42

Abbreviations

AO	Atomic oxygen, p. 13
IHRT	Institute for Handling Devices and Robotics, p. 2
ISAS	Institute of Space and Astronautical Science, p. 2
LOFT	Low-Frequency Telescope, p. 4
SVD	Singular Value Decomposition, p. 17
VUT	Vienna University of Technology, p. 2

Chapter 1

Introduction

In the space industry there is an increasing need for larger structures, which require new ingenious solutions as the launch fleet practically is unchanged since the early eighties.

The prior trend in large deployed structures was to passively obtain the required accuracy by designing stiff structures that could be reliably tested under the influence of gravity [12, 14]; a typical example is the AstroMesh reflector antenna [54]. The current trend is towards larger and very flexible structures, such as solar sails [8], which makes ground testing absolutely impossible.

ESA Advanced Concepts Team has looked at the possibility of constructing large space antennas and solar power systems by deploying and stabilising a large web in space. The web will not contain any hard structures for prestressing, but rely on the stiffening effect of centrifugal forces by spinning the whole assembly of central satellite, corner satellites and web. Clever deployment strategies are required to control the deployment this very flexible structure. If not properly taken into account, the very high flexibility of the large web during deployment may create chaotic dynamics with high risk of entanglement. Such dynamic phenomena will inevitably lead to failure and loss of the mission. An example of such a chaotic behaviour is the deployment sequence of the Inflatable Antenna Experiment by NASA in 1996. The long inflatable feed booms did not behave as expected due to several reasons, e.g. residual air. As reliable tests cannot be performed under gravity, numerical analysis is required.

1.1 The Japanese Furoshiki experiment

The idea for the space webs originates from the Japanese "Furoshiki Satellite" [36, 37]. That is composed of a large membrane or net held in tension by controlled corner satellites or by spinning the whole assembly. The large aperture of the "Furoshiki" can be used as a phased antenna or as a solar power satellite. An idea put forward by Kaya *et al.* [18] is to build up the antenna or solar power elements by robots that crawls on the web like spiders.

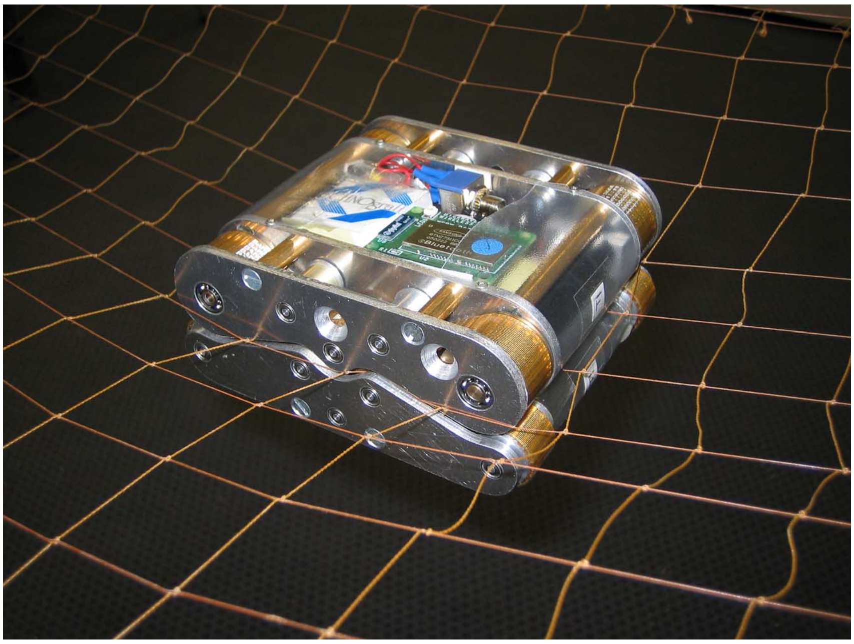

Figure 1.1: Crawling robot Roby Space III (Junior) on web (Courtesy of ESA).

The robots are developed by the Institute for Handling Devices and Robotics (IHRT) at the Vienna University of Technology (VUT) in Austria. The robot has a dimension of $100 \times 100 \times 50$ mm^3 and a mass of less than 1 kg, Figure 1.1. This robot can crawl on the web if the mesh width of the web is between 30 and 50 mm [16].

In early 2006, the Institute of Space and Astronautical Science (ISAS) in Japan performed an in-space deployment experiment of a triangular space web with side length 17 m, [38]. The satellite containing the web was launched by a S-310-36 sounding rocket. Each of the three corner satellites was released radially by a spring at an initial velocity of 1.2 m/s. The satellites reached their maximum distance from the the central satellite (10 m) about 8 s after deployment initiation. Thruster control was installed to prevent the bouncing back of the corner satellites after the deployment. At present, the post-experiment analysis is not complete [38].

1.2 Aims and scope of project

The aims of the present project are:

1. Design a web architecture that can be adequately prestressed by centrifugal forces and study the web behaviour in terms of stiffness and vibration characteristics.

2. Find a suitable folding pattern for the deployment by centrifugal forces.

3. Develop analytical and numerical models for the study of the web deployment.

The report is structured as follows:

- The first chapter (this) introduces the concept and presents the latest results from the Japanese sounding rocket experiment.
- The second chapter contains an extensive literature review of other spin-stabilised structures.
- The third chapter contains the first part of this study, the design of the web architecture. The web design section includes: material, geometry, topology, stresses due to spinning, out-of-plane stiffness, eigenfrequencies and eigenmodes, and fracture probability due to micro-meteoroid impact. Numerical routines are written in MATLAB for the automatic generation of webs with various geometries and topologies. These webs are then analysed by pre-existing MATLAB routines for the static and dynamic analysis of the webs.
- In the fourth chapter, folding patterns suitable for the developed web architectures are analysed. Numerical routines are written in MATLAB for automatic folding of the webs. A literature review on folding patterns precedes the selection of the most suitable one.
- The fifth chapter contains analysis of the space web deployment. Analytical routines are written in MATLAB to quickly assess various deployment control strategies. The folded web from section four is exported from MATLAB to the software LS-DYNA for a full three-dimensional deployment analysis involving contact between centre hub **and cables and between individual cables**. The control strategy identified by the analytical routine is implemented in the LS-DYNA runs.

Chapter 2

Literature review

The use of centrifugal forces to stabilised large space structures is not new, as the literature review below shows.

2.1 The Heliogyro solar sail

The Heliogyro has been the subject of in-depth analysis since its introduction by MacNeal [23] in 1967. The conceptual basis of the Heliogyro is based on a helicopter's rotors. As shown in Figure 2.1, the heliogyro is made up of a centrally located payload and control structure with long thin blades extending outward. The blades constitute the sail of the craft, and can be cyclically rotated to obtain attitude control. The overwhelming advantage of the Heliogyro is its low stowage volume and ease of deployment. This is in part due to the lack of boom structure required by the blades. The blades are typically comprised of very long, 1 to 3 metre wide sheets that can be stowed in rolls, obviating the need for complex folding and packaging. Deployment of the blades is obtained by rotating the base craft and gradually unrolling the stowed blades. This rotation causes a centrifugal force which acts to rigidize the otherwise thin film blades and must be maintained throughout the mission. *Centrifugal force is selected as the preferred method for rigidising the long narrow sails on the basis of minimum weight and minimum complexity* [28, 62].

2.2 The LOFT radio astronomy facility

Schuerch and Hedgepeth [13,49] present a feasibility study of a large-aperture paraboloidal-reflector low-frequency telescope (LOFT). Its central component is a parabolic reflector surface which is deployed and contour-stabilised by a slow spinning motion around its axis of symmetry, orbiting at an altitude of 6000 km. The diameter of the reflector is 1500 m, the focal-length-to-diameter ratio 0.5 and the total height is 1020 m, Figure 2.2. A conductive aluminium web with 0.40 m mesh width is supported by a stainless steel

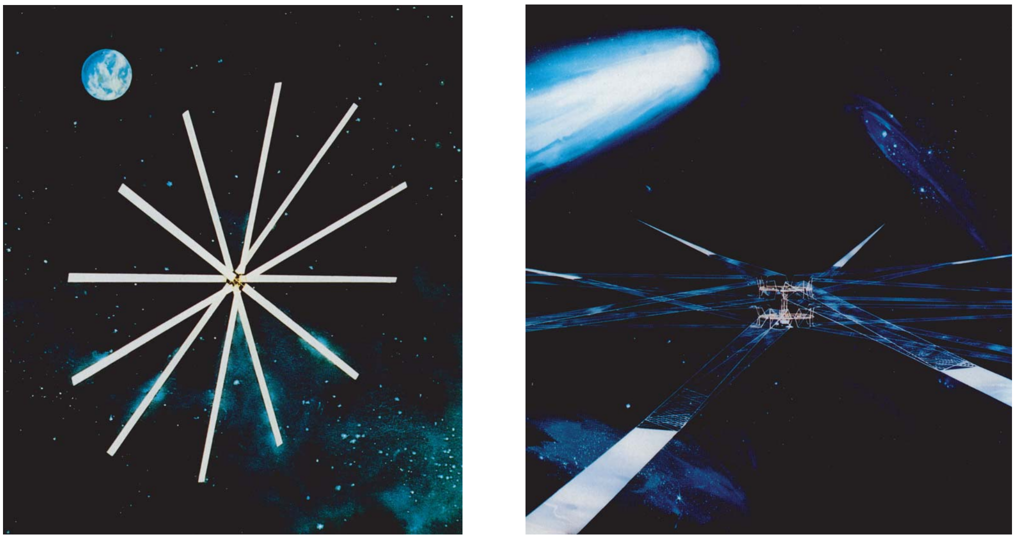

(a) (b)

Figure 2.1: The Heliogyro solar sail, [52].

support net and back stays. The central deployable mast has a diameter 3.04 m and a length of 760 m. The estimated total weight of the system is 2640 kg or 1.5 g/m^2.

Schuerch and Hedgepeth [49] concluded that "the burden of technology development becomes primarily one of structural design. Practical and credible methods must be devised to fabricate, package, deploy in space, and maintain adequate dimensional tolerances in a structure of truly unprecedented size and performance."

The angular velocity of the LOFT was one revolution per 11.4 minutes (0.00916 rad/s). The selected angular velocity was a compromise: fast enough to generate sufficient tensile stresses in the net and to avoid dynamic coupling with the slower orbital frequency, but slow enough to keep the demand for orientation control torques at tolerable levels [49]. The size of the packaged LOFT is 5.5 m in diameter and 5.9 m in height, Figure 2.3(a). During deployment, the spin propulsion system transfer angular momentum through the front stays to the reflector. The system is programmed to provide the total angular momentum to the structure at a time when about 60% of the reflector is deployed. After the propulsion system has been shut down the radial deployment continues, but Coriolis forces slow the rotational speed down as the network is deployed into an approximately flat disk. Calculations performed by Schuerch and Hedgepeth show that complete deployment can be accomplished in less than two days [49].

2.3 The Znamya-2 experiment

The Russians have twice deployed large, sail-like mirrors in space. The wheel-like mirrors, named Znamya, were spun on motor-driven axles to keep their shape through centrifugal

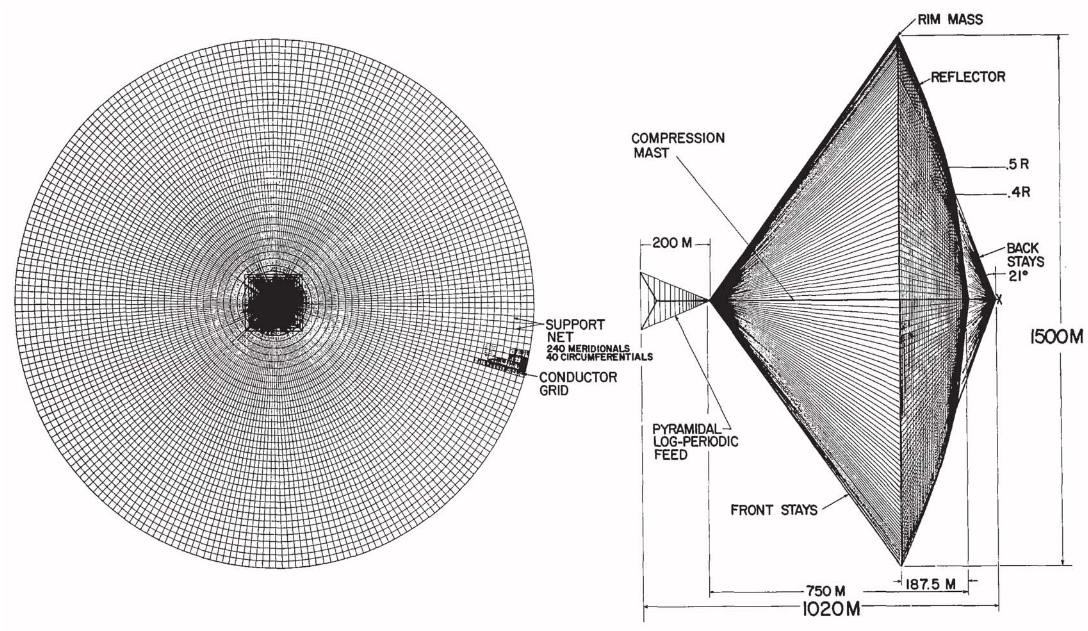

Figure 2.2: The baseline design of the LOFT concept, [49].

force. A 20-metre-diameter version, Figure 2.4, was successfully tested in space in 1993 using a Progress resupply vehicle that had just undocked from the MIR space station. The simple deployment process was driven solely by spinning up the stowed reflector using an on-board electric motor. Observed from the MIR space station, the test demonstrated that such spin deployment can be controlled by simple means. While the reflectors can demonstrate technologies for solar sailing, their principal use was to illuminate northern Russian cities during dark winter months to aid economic development [28, 29].

However, a 25-metre version failed in 1999, when it tangled on an antenna jutting out from the Progress spacecraft that was deploying it. The antenna had been used in the docking maneuver, and was supposed to have been retracted before sail deployment. A mission operations software was to blame [8].

2.4 Other studies

Onoda *et al.* [39] recently performed a preliminary analytical investigation of a spin-stabilised solar sail and verified the concept by a 2.2-m-diameter model experiment under gravity and normal air pressure. The membrane deployed as expected at a constant angular velocity. Miyazaki and Iwai [32] developed a mass-spring network model for the simulation of the deployment phase of a spinning solar sail. A comparison was made between membrane and mass-spring simulations for a 2-m-diameter solar sail model as shown in Figure 2.5. The angular velocity of the hub is not controlled and thus rotates so that the total angular momentum is conserved. After full deployment at around 0.25

s, the sail starts to repackage itself in the opposite direction. They concluded that the differences between the membrane and mass-spring models were small and also that a deployment simulation is difficult using a commercial software [32].

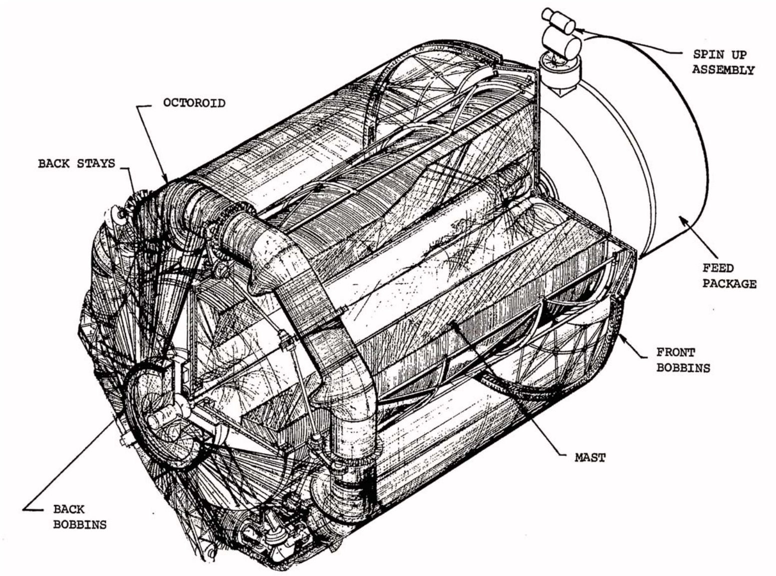

(a)

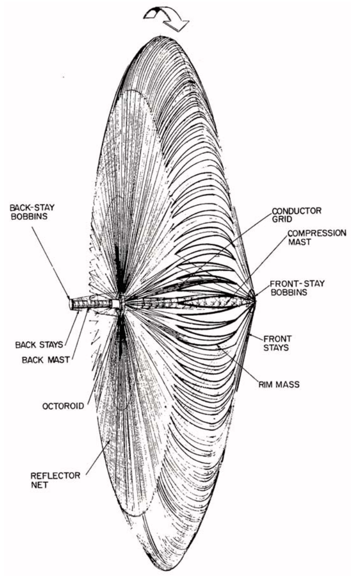

(b)

Figure 2.3: The LOFT concept: (a) packaged configuration and (b) during deployment, [49].

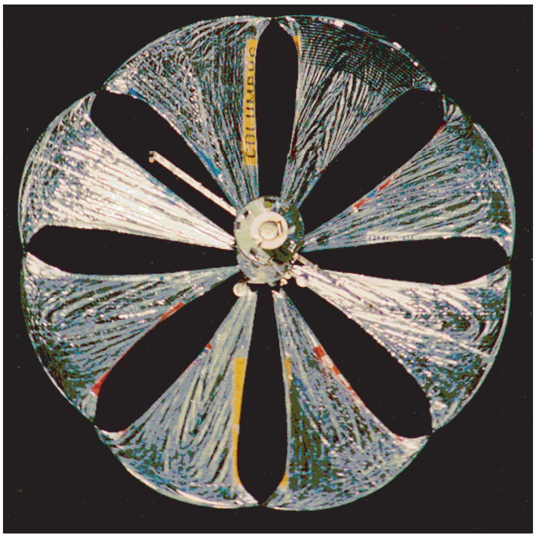

Figure 2.4: Znamya deployment test, 4 February 1993.

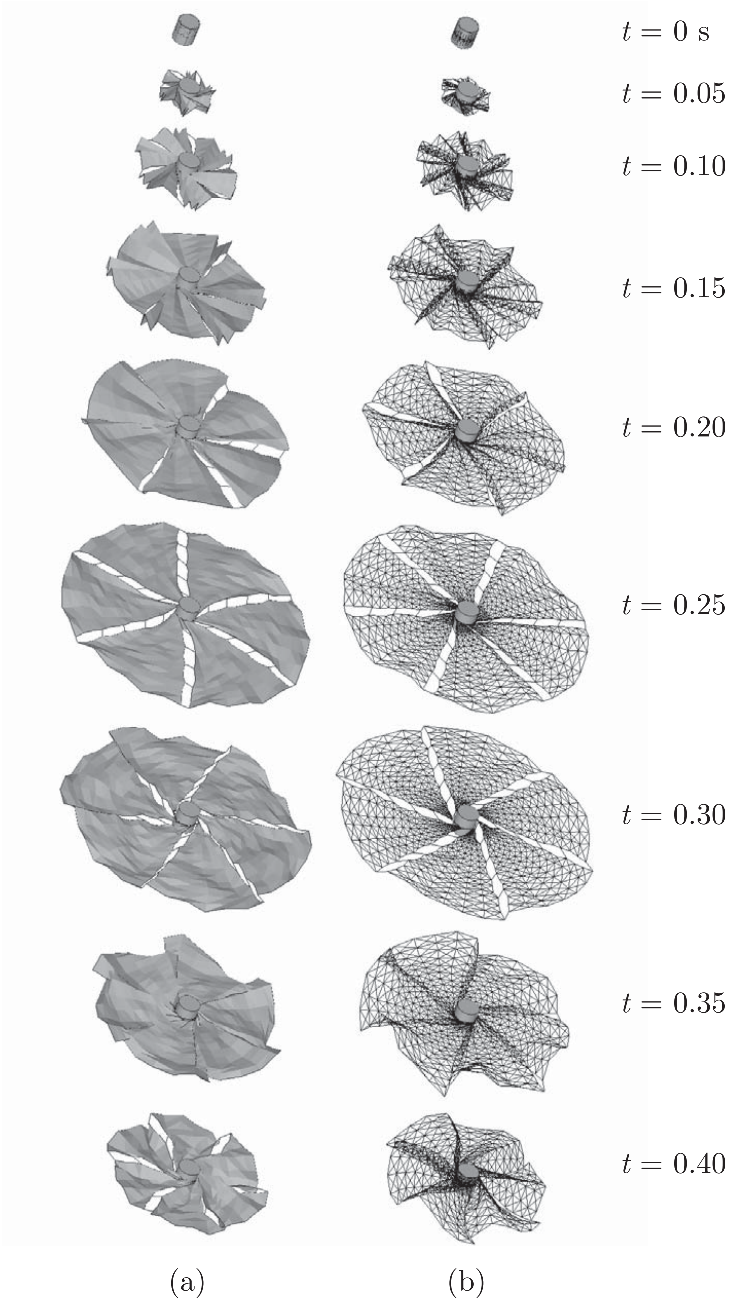

Figure 2.5: Deployment simulations by Miyazaki and Iwai using (a) membrane elements and (b) masses and springs. From [32].

Kanemitsu *et al.* [17] investigated the self-deployment of a 2-metre-diameter antenna by the centrifugal force. The antenna is stowed as a polygonal column before deployment with solar panels on each trapezoidal piece. A series of tests, in which the zero gravity environment of space was simulated by water, was performed. Although the antenna deployed completely under the test conditions, absolute zero gravity could not be simulated.

Therefore, a structural deployment analysis was performed using the multi-body software ADAMS, which showed that the antenna does not deploy completely under the action a centrifugal forces. The reasons for this are believed to be inadequate modelling of interference between different segments and the mechanisms which control the deployment [17].

Mori *et al.* [34, 59] analyse the spinning deployment of clover type solar sail. The clover type sail has a quadratic main sail with two fan parts in each corner, Figure 2.6. The sail is folded in a star-like pattern, so that each section is first line-shaped and then coiled around the central hub. The deployment is performed in two stages. First, the line-shaped parts are coiled off the central hub to form a cross as they are fixed to the hub at their roots. Then, the constraints are released and the remainder of the sail is deployed. Mori *et al.* [34] perform two deployment experiments: a spinning table in ambient environment and an in-orbit experiment using a sounding rocket. The diameter of the sail for the ground experiment was 2.5 m, whereas it for the sounding rocket experiment was 10 m. The ground experiments showed that the coiling off-coiling on phenomenon did not occur due to the air resistance, so in-orbit experiments are required. To adjust the deployment time for the space experiment, tip masses were added. To prevent re-coiling of the sail around the centre hub, a one way clutch mechanism was used. If the centre hub rotates faster than the tip of the sail, the clutch is locked, whereas if the tip rotates faster, the clutch is slipping so that the motions of the sail and centre hub are uncoupled. *The stick-slip clutch is a simple way to achieve a controlled deployment*. A mass-spring model was later used to simulate the two deployment stages, Figure 2.7. The one way clutch was incorporated in the model. Simulations using a coarse model show a behaviour close to that observed in the experiments.

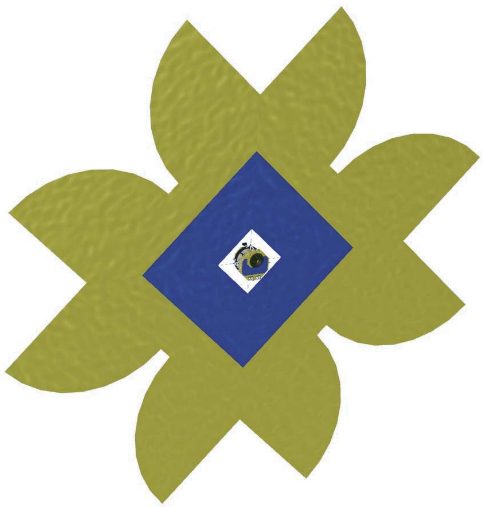

Figure 2.6: The clover type solar sail. From [34].

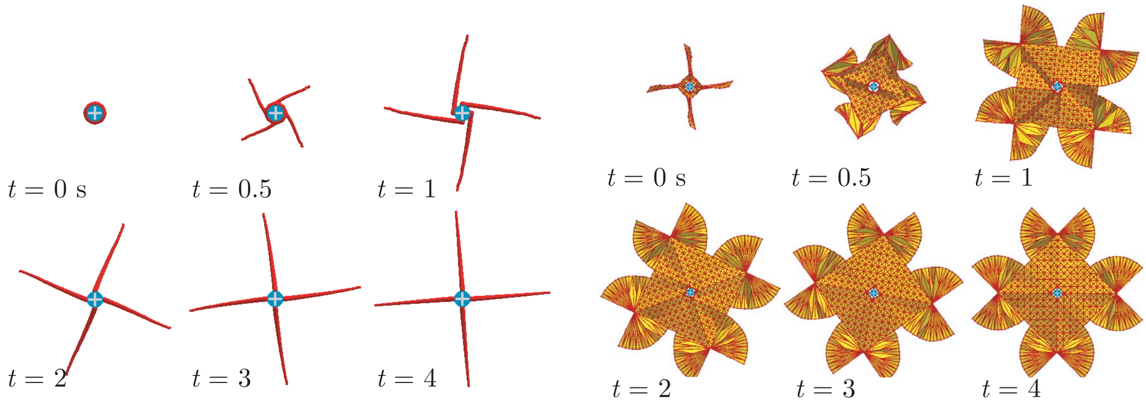

(a) First stage deployment (b) Second stage deployment

Figure 2.7: Deployment of the clover type solar sail. From [34].

Matunaga *et al.* [25, 27] introduce a triangular spinning solar sail that is tether-controlled during and after deployment. The sail is composed of three corner satellites connected by tethers and large triangular film surface, Figure 2.8. The sail is folded in way so that three radial arms are formed. These are then rolled up on special motor-controlled mechanisms attached to the corner satellites. During deployment, the length between the corner satellites are controlled by the tethers, which take all the tension. Hence, the mechanism paying out the sail film does not have to cope with large forces, which simplifies the deployment control. Matunaga *et al.* [27] performed ground experiments with air thrusters on the corner satellites. The corner satellites in the experiment weighed about 42 kg with dimensions $0.6 \times 0.6 \times 0.47$ m^3. The initial side length was 730 mm, whereas the final one was 1760 mm. Although the experiment showed that the model could be made to spin, the corner satellites were too heavy to be controlled by the air thrusters. Matunaga *et al.* also performed simulations using a mass-spring model. Two simulations were run: one without tethers between the corners and one with, in order to show the advantage of having tethers. Their simulations are shown in Figure 2.9, where it can be observed that the simulations starts when the tethers are fully deployed, but where the sail is yet to be deployed. The sail without tethers shows a more uncontrolled behaviour with bouncing motion and distorted shape. Matunaga *et al.* [26] previously analysed the deployment of a 30×30 m^2 quadratic sail with radial tethers. Two tether control option were introduced in the mass-spring model: tension or length control. For the case of no control or tension control, the usual coiling off-coiling on phenomenon was observed, whereas in the case with length control, stable deployment was achieved. A combination of length control in the early phased of deployment and tension control in the latter ones also yielded a stable deployment. Snapshots from a trial simulation is shown in Figure 2.10.

Other studies that investigate various aspects of spin-stabilised space structures are [30, 35, 39, 43, 61]

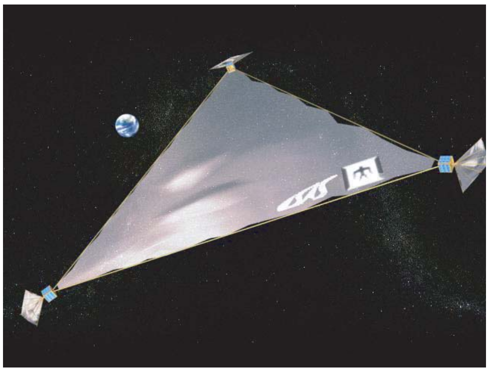

Figure 2.8: Tether-controlled spinning solar sail. From [27].

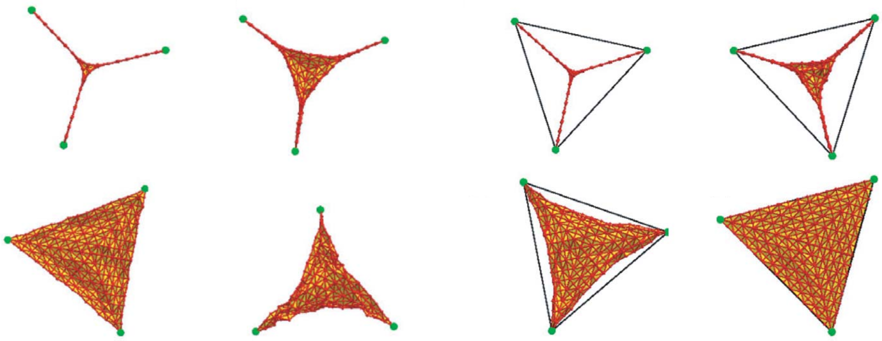

(a) Non-tethered (b) Tethered

Figure 2.9: Deployment of triangular sail: (a) without tethers and (b) with tethers. From [27].

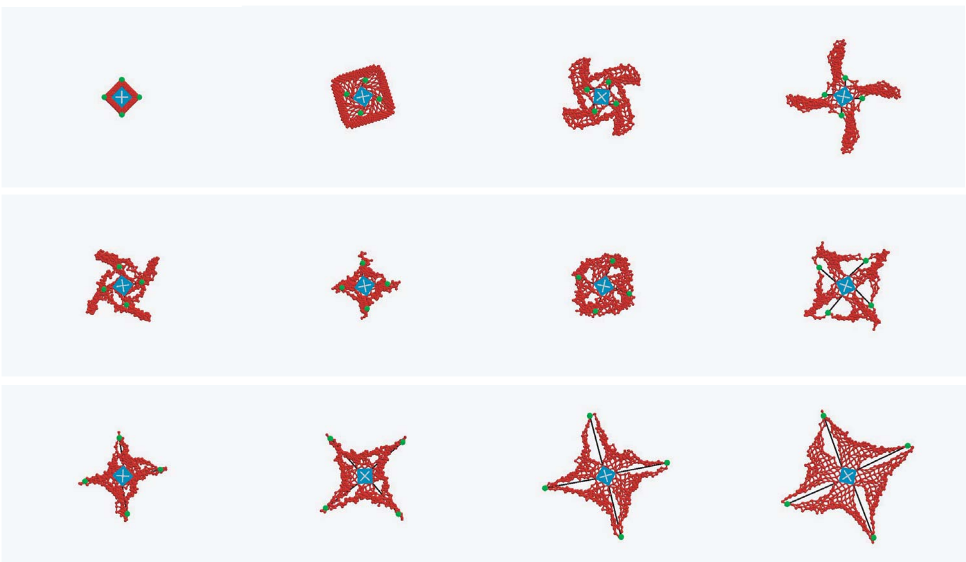

Figure 2.10: Deployment of quadratic solar sail. From [26].

Chapter 3

Web design

The following part of the report studies various design aspects not related to the subsequent folding and deployment of the space webs. Prior studies, [18, 38], have not looked into the various choices of web geometry and mesh topology. The prestress distribution in the web is not uniform due to the centrifugal force field and it is required that the web is in tension everywhere. The prestress in the web provides the out-of-plane stiffness and that stiffness may depend on the choice of mesh topology. The spinning of the web and the low out-of-plane stiffness create undesirable dynamic phenomena, such as travelling waves and excess out-of-plane deformations, which affect the performance of the web. Due to all these aspects, a thorough analysis is required to obtain an adequate design of the web.

3.1 Web material

The web should be manufactured from a very light, but strong and stiff material. A large modulus is not necessarily an advantage since that requires a higher manufacturing accuracy. A fundamental property is that the material should be very flexible in bending so that the web members easily can be folded. Table 3.1 lists properties of fibres for candidate materials. The factor governing the mass of the web is the breaking length, $\sigma_u/\rho \mathrm{g}$, whereas, in a micro-gravity environment, the most important factor is the tensile strength, σ_u. As the Zylon fibre has superior properties compared to the other fibres, Zylon is chosen as the fibre for manufacturing the space web.

Most high performance fibres suffers from strength degradation when exposed to light [11]. The strength of Zylon® decreases with exposure to sunlight and must be protected not only from ultraviolet (UV) light but also from visible light. Experiments by the manufacturer show that the residual strength of Zylon® after six months exposure to daylight is about 35% [58]. Tests performed by Seely *et al.* [50] show that unshielded Zylon® fibres lost 55% of their strength in only 12 months, whereas fibres that has been shielded from light (stored in heavy black polyethylene film) lost only 13% in the same time period

Table 3.1: Properties of some candidate material fibres [11, 50].

Trade name	Generic name	Type	σ_u (GPa)	E (GPa)	ε_u (%)	ρ (g/cm^3)	$\sigma_u/\rho g$ (km)
Zylon	PBO	AS	5.8	180	3.5	1.54	384
Dyneema	HPPE	SK76	3.7	116	3.8	0.97	389
Kevlar	Aramid	49	3.6	130	2.8	1.44	255
Vectran	TLCP	HS	2.9	65	3.3	1.40	211

due to unidentified causes. Gittemeier *et al.* [7] recently analysed the effects of various coatings on the strength degradation rate of the fibres Zylon® and Spectra 2000 (similar to Dyneema) when exposed to UV light and atomic oxygen (AO). Both fibre types show severe strength degradation and slight mass loss, when exposed to the space environment. The general conclusion of Gittemeier *et al.* [7] is that "further coating work is needed to improve the performance of Spectra and Zylon" for long-term space missions. Gittemeier *et al.* [7] also measured the mass loss and found it to be at most 7%, which can be disregarded in the subsequent simulations.

The strength and stiffness of Zylon® are also temperature dependent and at 200°C, the relative strength and stiffness are 75% and 90%, respectively [58]. The knot and loop strength of Zylon® is 30% of its tensile strength, [58], which must be taken into account since the web presumably will be knotted. The abrasion resistance of Zylon® is higher than Kevlar®, but much lower than high molecular weight polyethylene fibres, such as Dyneema® and Spectra® [58].

The company Phillystran® manufactures Zylon® AS strands in a variety of dimensions, which are shown in Table 3.2. The modulus of the strands varies from 68 to 80% of the modulus of the fibre, which is due to the braiding [50].

Table 3.2: Mechanical properties of low modulus Zylon® strands from Phillystran® [42].

Part number	$d_{\min} \times d_{\max}$ (mm^2)	T_u (N)	E (GPa)	$A\rho$ (kg/km)
PSAS Z15	0.43 × 0.66	534	145	0.19
PSAS Z30	0.61 × 0.86	1068	145	0.39
PSAS Z45	0.74 × 1.22	1601	145	0.61
PSAS Z60	0.79 × 1.50	2135	138	0.79
PSAS Z75	0.82 × 1.83	2669	138	0.98
PSAS Z90	0.86 × 1.90	3025	131	1.22
PSAS Z105	0.86 × 2.03	3559	131	1.41
PSAS Z150	0.91 × 3.17	4804	124	2.04
PSAS Z180	1.02 × 3.43	5783	124	2.44

Considering the cumulative effects of light and temperature degradation, knots and loops, and braiding, the following safety factors are suggested for the strength and modulus. If the strength and modulus values are taken from Table 3.2, the effects of the braiding is already accounted for. The reduction factors due to temperature are 0.75 and 0.90 for the strength and modulus, respectively. For a knotted web, only the strength is affected and the reduction factor is 0.30. It is clear from the published tests, that the Zylon® fibres must be shielded from light. The choice of shielding material and its effectiveness is still unclear, so it may be assumed that the strength reduction due to light and atomic oxygen is 50% throughout the mission life (if less than one year). The environmental effects affects the ductility of the material, which means that the stiffness do not necessarily diminish with the same rate as the strength. Due to lack of information, it is assumed that the stiffness reduction due to light and atomic oxygen is 25%. This reasoning leads to the following safety factors for the strength

$$f_{s,\sigma} = \frac{1}{\underbrace{0.75}_{\text{temp.}} \cdot \underbrace{0.30}_{\text{knot}} \cdot \underbrace{0.50}_{\text{light}}} \approx 8.89 \quad \Rightarrow \quad f_{s,\sigma} = 9 \tag{3.1}$$

and for the modulus

$$f_{s,E} = \frac{1}{\underbrace{0.90}_{\text{temp.}} \cdot \underbrace{0.75}_{\text{light}}} \approx 1.48 \quad \Rightarrow \quad f_{s,\sigma} = 1.5 \tag{3.2}$$

Thus, a safety factor a high as 9 is needed for the strength, but one of only 1.5 is required for the modulus. This brief material excursion shows that a careful choice of material is required so that the web does become unnecessarily heavy. *In the remainder of the this report we are using the characteristic strengths and stiffnesses of the web material (Zylon®) and thus assuming that improvements in material technology will take place before the space web will be launched.*

3.2 Web geometry

Two different web geometries will be analysed:

- a central hub and *three* corner masses, and
- a central hub and *four* corner masses.

The hub and the corner masses are all connected by tethers. The tether connecting a corner mass with the hub is called *radial tether* and that connecting two corner masses is called *edge tether*. The radial tethers are straight whereas the edge tethers are circular arches with a radius R. For a given side length S of the web, the radius of the edge tether is

$$R = \frac{1 + 4\varrho^2}{8\varrho} S \tag{3.3}$$

where ϱ is the sag-to-span ratio. For a given sag-to-span ratio, the total area of the space web is computed as

$$A_{\text{sw}} = nS^2 \left[\frac{1}{4} \cot \frac{\pi}{n} + \frac{1-4\varrho^2}{16\varrho} - \left(\frac{1+4\varrho^2}{8\varrho} \right)^2 \arcsin \left(\frac{4\varrho}{1+4\varrho^2} \right) \right] \tag{3.4}$$

where n is the number of corners. For perfectly straight edge cables (which is physically impossible for a non-spinning web since the force in the edge tether would be infinitely large), the area is simply

$$\lim_{\varrho \to 0} A_{\text{sw}} = \frac{nS^2}{4} \cot \frac{\pi}{n} \tag{3.5}$$

For a quick comparison of the total surface area of various web geometries, the relative surface area as a function of the sag-to-span ratio is shown in Figure 3.1. The relative area decreases almost linearly with increasing sag-to-span ratio.

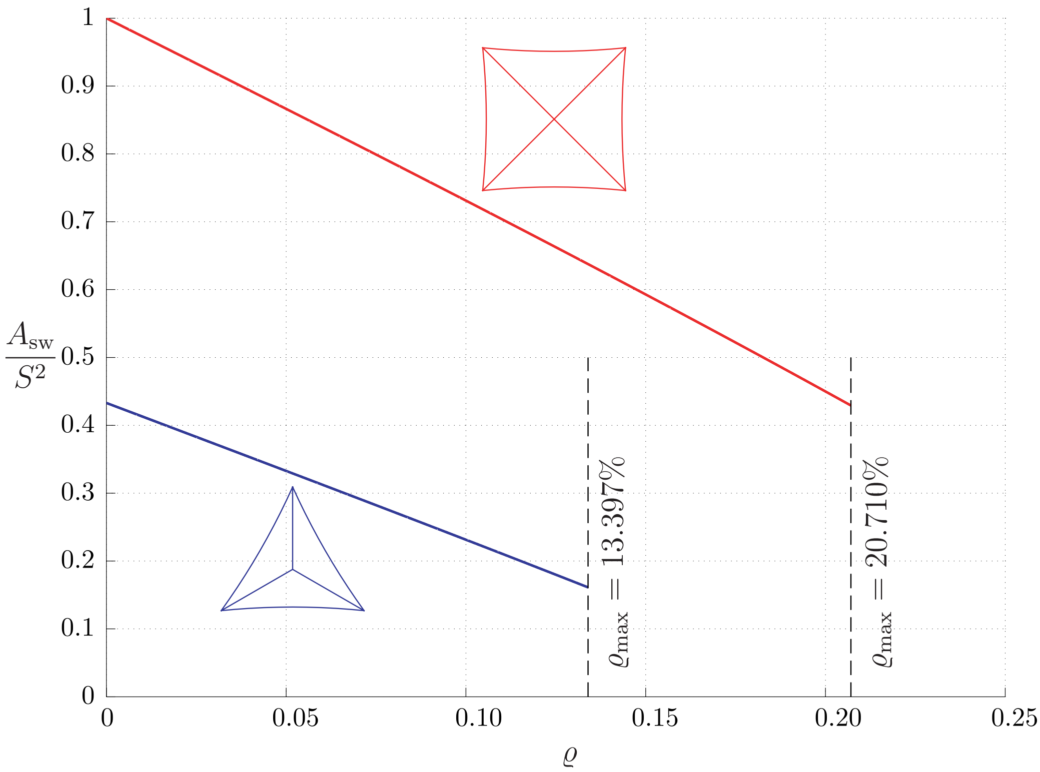

Figure 3.1: The relative surface area of the web as a function of the sag-to-span ratio of the edge cables.

The maximum permissible sag-to-span ratio is found when a radial tether is tangent to the edge circle, which yields

$$\varrho_{\max} = \frac{1}{2} \left(\frac{1}{\sin\left(\frac{\pi}{2} - \frac{\pi}{n}\right)} - \sqrt{\frac{1}{\sin^2\left(\frac{\pi}{2} - \frac{\pi}{n}\right)} - 1} \right) \tag{3.6}$$

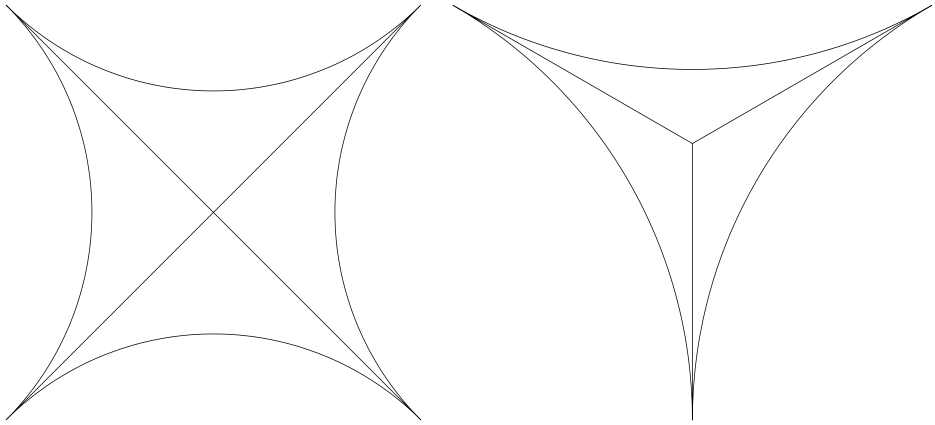

(a) $\varrho_{\max} = 20.710\%$ (b) $\varrho_{\max} = 13.397\%$

Figure 3.2: Configurations with maximum sag-to-span ratios.

For $n = 3$, $\varrho_{\max} = 13.397\%$ and for $n = 4$, $\varrho_{\max} = 20.710\%$. Configurations with the maximum sag-to-span ratios are shown in Figure 3.2. It is clear that a large sag-to-span ratio produces very pointy vertices, which is undesirable. The total length of the radial tethers is

$$S_{\mathrm{rt}} = nS\frac{1}{2\sin\frac{\pi}{n}} = \begin{cases} \sqrt{3}S & \text{for} \quad n = 3 \\ 2\sqrt{2}S & \text{for} \quad n = 4 \end{cases} \tag{3.7}$$

whereas the total length of the circular edge tethers is

$$S_{\mathrm{et}} = nS\left(\frac{1+4\varrho^2}{4\varrho}\right)\arcsin\left(\frac{4\varrho}{1+4\varrho^2}\right) \tag{3.8}$$

3.3 Topology

Once the geometry has been defined, the triangular areas defined by the tethers are to be filled by a mesh. There are several choice for the topology of that mesh. Schuerch and Hedgepeth [49] chose a quadrangular mesh for the LOFT concept, although previous reports on the LOFT, [44, 45], used a triangular mesh. The reasons for finally choosing the square mesh over the triangular one were, [49]:

- the shearing stiffness provided by the diagonal elements were not significantly greater than the stiffening effect derived from centrifugal forces; deleterious out-of-plane motions of the surface were reduced by deleting the diagonals, as vibrational energy then goes into the less harmful in-plane mode of deformation.
- the square mesh has the ability to undergo large shearing deformations, without requiring in-plane strains or creases in the material; characteristics important for packaging purposes.

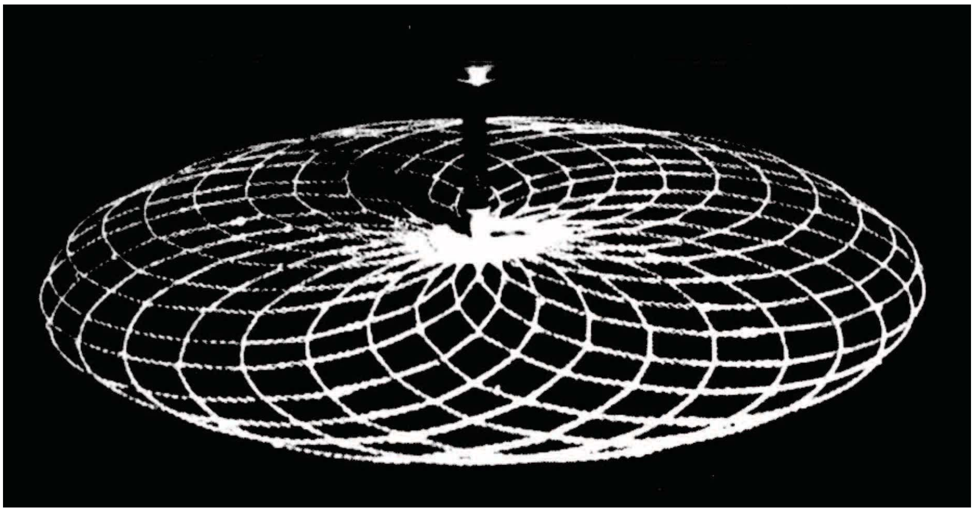

Figure 3.3: A uniform stress spinning web, [19].

Kyser [19,20] derives analytical relationships for mesh geometry of a circular spinning web with uniform prestress. He shows that the elements of the web must be oriented as spirals in order to obtain a uniform prestress, Figure 3.3. A spiral-like web will carry a radially-directed loading in such a way that the resulting tension decreases towards the centre. A uniformly stressed web is obviously interesting structurally, but the non-constant mesh width will create problems for the crawling robots as the mesh width becomes very large far away from the centre of the web. Thus, this web topology is not of interest for the present project.

The web topology is a crucial aspect of the web design as this dictates the static and kinematic properties of the web through the generalised Maxwell's rule [1]

$$3j - b - c = m - s \tag{3.9}$$

where j is the number of joints, b the number of elements, c the number of kinematic constraints, m is the number of mechanisms and s the number of states of self-stress.

A simple comparison between different web topologies can be done by considering a triangle, a square and a hexagon, which are constrained from rigid body motions, i.e. $c = 6$. The triangle has $j = b = 3$ and $s = 0$, which yields $m = 0$. For the square and hexagon, $m = 2$ and $m = 6$, respectively. Thus, the triangle is shear-stiff, whereas the square and the hexagon have several internal mechanisms. The number of mechanisms for a specific web topology must be found by a Singular Value Decomposition (SVD) of the equilibrium matrix [40, 55].

The mesh topology is defined by the parameter μ, which is equal to 3 for a triangular mesh, 4 for a square mesh and 6 for a hexagonal mesh. The six possible space web configurations with the above topologies and three and four corners are shown in Figure 3.4. A MATLAB routine has been written to generate the configurations shown in Figure 3.4. The routine can handle arbitrary values of the element length and the sag-to-span ratio. In terms of manufacturing, the most regular web configurations are:

- Triangular web and triangular mesh (TriTri), $n = 3,\ \mu = 3$,
- Triangular web and hexagonal mesh (TriHex), $n = 3, \mu = 6$, and
- Quadratic web and quadratic mesh (QuadQuad), $n = 4,\ \mu = 4$.

The advantage with these configurations is the irregularities are restricted to the edges, whereas for the other three configurations, i.e. Figs. 3.4(b), (d) and (f), irregularities appear also along the radial tethers. Thus, the subsequent analyses was initially limited to these three regular configurations, but, as will be shown in section 3.5, the TriQuad configuration ($n = 3, \mu = 4$) is also of interest and will therefore be included.

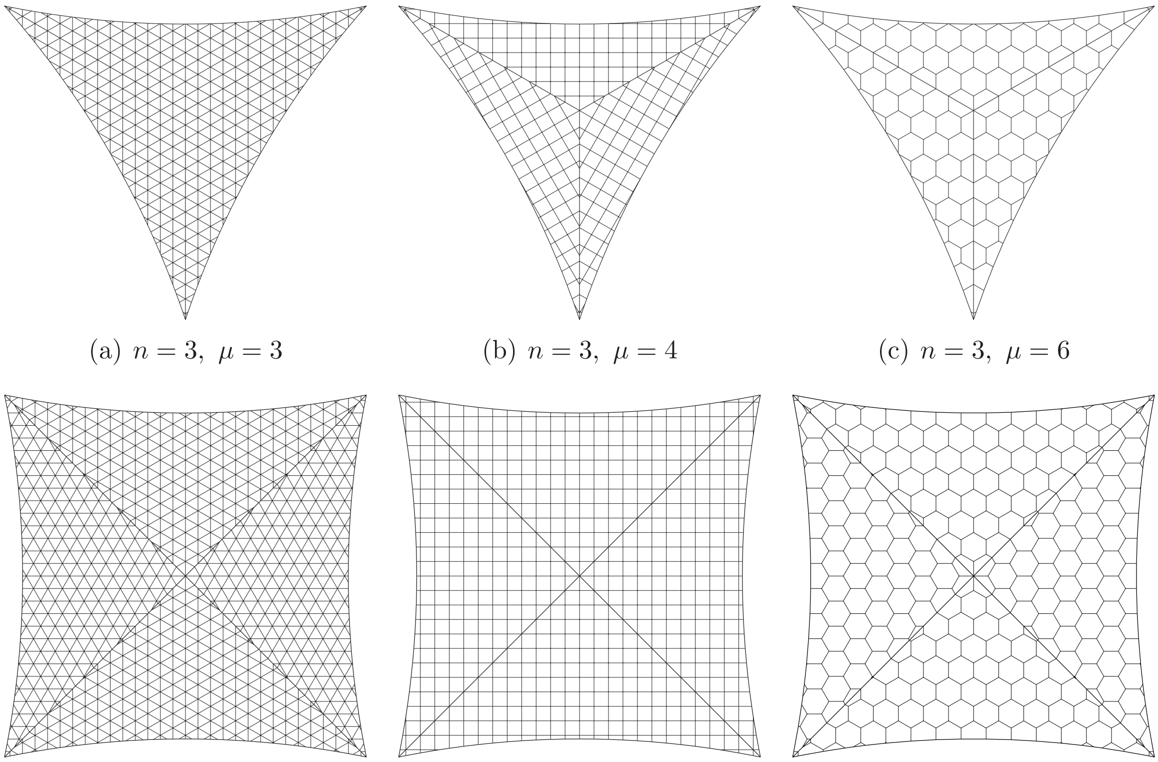

(a) $n = 3,\ \mu = 3$ (b) $n = 3,\ \mu = 4$ (c) $n = 3,\ \mu = 6$

(d) $n = 4,\ \mu = 3$ (e) $n = 4,\ \mu = 4$ (f) $n = 4,\ \mu = 6$

Figure 3.4: Possible web and mesh configurations for $n = 3, 4$ and $\mu = 3, 4, 6$.

The factor governing the mass of the web is the total length of interior elements, i.e. excluding radial tethers and element forming the circular boundaries. Preliminary analyses show that the total length increases exponentially with diminishing ratio ℓ/S, where ℓ is the length of interior web members, but increases almost linearly with the decrease of the sag-to-span ratio, ϱ. However, for an upper bound estimate of the total length of web elements, it is assumed that $\varrho = 0$. This yields the following equation for the total length of interior elements:

$$\log_{10}\left(\frac{\sum \ell}{S}\right) = A_{n,\mu}\log_{10}\left(\frac{\ell}{S}\right) + B_{n,\mu} \tag{3.10}$$

Least squares solutions for the four interesting combinations yield:

$$A_{3,3} = -1.0118,\ B_{3,3} = 0.1469 \quad (\mathrm{R}^2 = 1.0000) \tag{3.11a}$$
$$A_{3,6} = -1.0073,\ B_{3,6} = -0.3197 \quad (\mathrm{R}^2 = 0.9997) \tag{3.11b}$$
$$A_{4,4} = -1.0015,\ B_{4,4} = 0.2973 \quad (\mathrm{R}^2 = 0.9997) \tag{3.11c}$$
$$A_{3,4} = -0.9903,\ B_{3,4} = -0.0391 \quad (\mathrm{R}^2 = 0.9996) \tag{3.11d}$$

Hence, a 100×100 m^2 web with 30 mm mesh width requires $100\cdot10^{(-1.0015\cdot\log_{10}(3\cdot10^{-4})+0.2973)} \approx$ 669 km of cable (excluding radial and edge cables). Using the thinnest Zylon strand in Table 3.2, the total weight of such a web will be at least 127 kg.

3.4 Stresses in a non-spinning web

For a web with several internal mechanisms, $m > 0$, its equilibrium geometry is governed by the force distribution [48,57]. Since three different topologies are to be investigated, i.e. triangular, square and hexagonal, an easy way of comparing them structurally is desired. In addition, an simple analytical relationship between the forces in the web and the forces in the tether is of importance in order to simplify the calculations. In this section, a way comparing the webs in terms of stresses is proposed.

3.4.1 Forces in interior cables and equivalent in-plane stresses

The factor governing the out-of-plane stiffness of the web is the force t_{int} in the interior elements. However, since the mesh size will be very small, the web can be seen as a membrane, with in-plane stresses $\boldsymbol{q}^{\mathrm{T}} = (q_x\ q_y\ q_{xy})$ (N/m). Following the approach by Lai *et al.* [21], the interior forces t_{int} can be transformed to equivalent membrane stresses $\boldsymbol{q}$ via *natural stresses*. The consistent nodal forces $\boldsymbol{p}$ due to initial stresses $\boldsymbol{\sigma}$ in a Cartesian coordinate system is written as [2]

$$\boldsymbol{p} = \int \mathbf{B}^{\mathrm{T}}\boldsymbol{\sigma}\mathrm{d}V = \int \mathbf{B}^{\mathrm{T}}\boldsymbol{q}\mathrm{d}A \tag{3.12}$$

For a constant strain triangle (CST), [2],

$$\mathbf{B} = \frac{1}{2A}\begin{bmatrix} y_{23} & 0 & y_{31} & 0 & y_{12} & 0 \\ 0 & x_{32} & 0 & x_{13} & 0 & x_{21} \\ x_{32} & y_{23} & x_{13} & y_{31} & x_{21} & y_{12} \end{bmatrix} \tag{3.13}$$

where $x_{ij} = x_i - x_j$ and $y_{ij} = y_i - y_j$ and A is the triangle area. Transforming the consistent Cartesian force components $\boldsymbol{p}$ into skew components, or '*natural forces*', parallel to the edges of the element, yields the triangle side forces, [21]:

$$\begin{pmatrix} t_{12} \\ t_{23} \\ t_{31} \end{pmatrix} = \frac{1}{4A} \begin{bmatrix} \ell_{12} y_{13} y_{23} & \ell_{12} x_{13} x_{23} & \ell_{12}(x_{32} y_{13} + x_{13} y_{32}) \\ \ell_{23} y_{12} y_{13} & \ell_{23} x_{12} x_{13} & \ell_{23}(x_{31} y_{12} + x_{12} y_{31}) \\ \ell_{31} y_{12} y_{32} & \ell_{31} x_{12} x_{32} & \ell_{31}(x_{23} y_{12} + x_{12} y_{23}) \end{bmatrix} \begin{pmatrix} q_x \\ q_y \\ q_{xy} \end{pmatrix} \tag{3.14}$$

Solving Eq. (3.14) for $\boldsymbol{q}$ for an equilateral triangle with side length $\ell$and side 12 parallel to the x-axis, the side force $t_{12} = t_{23} = t_{31} = t_{\mathrm{int}}/2$ yields

$$\boldsymbol{q}_3^{\mathrm{T}} = \begin{pmatrix} \sqrt{3}\frac{t_{\mathrm{int}}}{\ell} & \sqrt{3}\frac{t_{\mathrm{int}}}{\ell} & 0 \end{pmatrix} \tag{3.15}$$

which means that a web with a triangular mesh can be seen as a membrane under uniform tension $q = \sqrt{3} t_{\mathrm{int}}/\ell$.

For a square mesh, the procedure is simpler as the sides are parallel to the axes of the Cartesian coordinate system. For a rectangle with side lengths $2a$ and $2b$ in the x and y directions, respectively,

$$\mathbf{B} = \frac{1}{4ab} \begin{bmatrix} -(b-y) & 0 & (b-y) & 0 & (b+y) & 0 & -(b+y) & 0 \\ 0 & -(a-x) & 0 & -(a+x) & 0 & (a+x) & 0 & (a-x) \\ -(a-x) & -(b-y) & -(a+x) & (b-y) & (a+x) & (b+y) & (a-x) & -(b+y) \end{bmatrix} \tag{3.16}$$

The consistent nodal loads are

$$\begin{pmatrix} p_{1x} \\ p_{1y} \\ p_{2x} \\ p_{2y} \\ p_{3x} \\ p_{3y} \\ p_{4x} \\ p_{4y} \end{pmatrix} = \int_{-b}^{b} \int_{-a}^{a} \mathbf{B}^{\mathrm{T}} \boldsymbol{q} \mathrm{d}x \mathrm{d}y = \begin{pmatrix} -bq_x - aq_{xy} \\ -aq_y - bq_{xy} \\ bq_x - aq_{xy} \\ -aq_y + bq_{xy} \\ bq_x + aq_{xy} \\ aq_y + bq_{xy} \\ -bq_x + aq_{xy} \\ aq_y - bq_{xy} \end{pmatrix} \tag{3.17}$$

For uniform element forces, $t_{ij} = t_{\mathrm{int}}$, in the square-meshed web: $t_{12} = t_{\mathrm{int}}/2 = p_{2x} = -p_{1x}$, $t_{23} = t_{\mathrm{int}}/2 = p_{1y} = -p_{4y}$, $t_{34} = t_{\mathrm{int}}/2 = p_{3x} = -p_{4x}$ and $t_{41} = t_{\mathrm{int}}/2 = p_{4y} = -p_{1y}$. For a square mesh, $\ell_{ij} = \ell$, these conditions yield the consistent nodal loads for a single square element

$$\boldsymbol{q}_4^{\mathrm{T}} = \begin{pmatrix} \frac{t_{\mathrm{int}}}{\ell} & \frac{t_{\mathrm{int}}}{\ell} & 0 \end{pmatrix} \tag{3.18}$$

which is lower than $\boldsymbol{q}_3^{\mathrm{T}}$ by $\sqrt{3}$.

For the hexagonal mesh the procedure is not as straightforward as for the triangular or the square meshes. One way is to assemble six equilateral triangles into a hexagon and compute the six consistent nodal loads at the vertices. The extra, seventh, node in the middle of the hexagon should not have a resulting nodal load due to symmetry. Computing the nodal forces at each vertex of the hexagon and then transforming those to element side forces yield the following conditions

$$t_{12} = t_{45} = \frac{\ell}{2}\left(\sqrt{3}q_x + q_{xy}\right) = \frac{\ell}{2}\left(\sqrt{3}q_y - q_{xy}\right) = t_{\text{int}}/2 \tag{3.19a}$$

$$t_{23} = t_{56} = \frac{\ell}{2}\left(\sqrt{3}q_y + q_{xy}\right) = \frac{\ell}{2}\left(\sqrt{3}q_x - q_{xy}\right) = t_{\text{int}}/2 \tag{3.19b}$$

$$t_{34} = t_{61} = \frac{\ell}{4}\left(\sqrt{3}q_x - 4q_{xy} + \sqrt{3}n_y\right) = \frac{\ell}{4}\left(\sqrt{3}q_x + 4q_{xy} + \sqrt{3}q_y\right) = t_{\text{int}}/2 \tag{3.19c}$$

Solving Eq. (3.19) for the equivalent membrane stresses yields

$$\boldsymbol{q}_6^{\mathrm{T}} = \begin{pmatrix} \frac{1}{\sqrt{3}}\frac{t_{\text{int}}}{\ell} & \frac{1}{\sqrt{3}}\frac{t_{\text{int}}}{\ell} & 0 \end{pmatrix} \tag{3.20}$$

Thus, the equivalent uniform membranes stresses can be written in the general form

$$\boldsymbol{n}_\mu^{\mathrm{T}} = 3^k \begin{pmatrix} \frac{t_{\text{int}}}{\ell} & \frac{t_{\text{int}}}{\ell} & 0 \end{pmatrix} \quad \text{with} \quad k = \frac{1}{12}\left(\mu^2 - 13\mu + 36\right) \tag{3.21}$$

where $\mu = 3, 4$ and 6 for the triangular, square and hexagonal mesh, respectively. As the shear stress $q_{xy} = 0$, the normal membrane stress in each direction is constant, just like a soap film.

3.4.2 Force in edge tether

The transformation from element forces to equivalent membrane stresses makes the determination of the force in the circular edge tether straightforward. The radius R of the edge tether as a function of the side length S and the sag-to-span ratio ϱ is given by (3.3). The axial force in a circular ring subjected to a uniformly distribution radial line load n_0 is [63]

$$t_{\text{et}} = Rq_0 = 3^k \frac{R}{\ell} t_{\text{int}} \tag{3.22}$$

where $k = (\mu^2 - 13\mu + 36)/12$.

3.5 Stresses in a spinning web

A non-spinning web is prestressed by pulling the circular edge tethers, which induce a uniform tension in the web as shown in section 3.4. In such a case there is a direct relation between the radius and force of the edge tether, Eq. (3.22). However, if the web is spinning, the stress will be non-uniform due to the centrifugal force field acting on the whole web. In this case, it becomes possible to have straight edge tethers. It still might be beneficial to have a circular edge tether as the outer parts of the web may not obtain a sufficiently large stress by the centrifugal field alone. In those cases, the non-uniform stress by the centrifugal forces on the web is increased by the uniform stress provided by the circular edge tether.

First, an approximate analysis was performed to investigate the ratio of the web stresses from spinning and those from the circular edge tether. Then, a more thorough analysis by the force method, [40, 55], was done.

3.5.1 Approximate analysis

For a circular membrane of radius r_m that is fully clamped to a hub of radius r_0, the radial stress is [43, 51]

$$\sigma_r(r) = \frac{3+\nu}{8}\rho\omega^2(r_m^2 - r^2)\left(1 + \epsilon\frac{r_0^2}{r^2}\right) \tag{3.23}$$

where

$$\epsilon = \frac{1-\nu}{3+\nu}\left[\frac{3+\nu-\lambda^2(1+\nu)}{1+\nu+\lambda^2(1-\nu)}\right] \tag{3.24}$$

$$\lambda = r_0/r_m \tag{3.25}$$

and ω is the angular velocity. For the special case $r_0 = r = 0$, Eq. (3.23) simplifies to

$$\max(\sigma_r)_{r0=0} = \frac{3+\nu}{8}\rho\omega^2 r_m^2 \tag{3.26}$$

For the Heliogyro solar sail, the radial stress at the root of the blade is [23]

$$\max(\sigma_r)_{\mathrm{HG}} = \frac{1}{2}\rho\omega^2 r_m^2 \tag{3.27}$$

where r_m is the length of the blade. As this stress is slightly higher than that for a circular membranes and independent of the Poisson's ratio, it will be used in the comparison below.

The centrifugal force on the corner mass m_c, at distance r_m from the centre of the web, is

$$F_c = m_c r_m \omega^2 \tag{3.28}$$

This force is equilibrated by the circular edge cables according to Figure 3.5. The distance to the corner mass is

$$r_m = \frac{S}{2\cos\frac{\pi}{n}} \tag{3.29}$$

and the angle between the edge tethers and the symmetry line in Figure 3.5 is

$$\psi = \frac{\pi}{2(6-n)} - \arcsin\left(\frac{4\varrho}{1+4\varrho^2}\right) \tag{3.30}$$

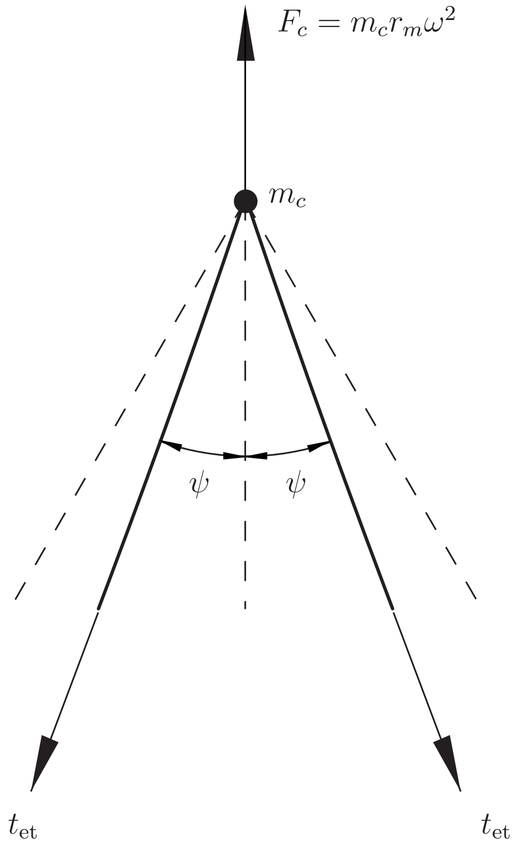

Figure 3.5: Equilibrium between the centrifugal force on the corner mass and the edge tethers.

For a straight edge cable, $\varrho = 0$, the angle ψ is $\pi/6$ for a triangular geometry and $\pi/4$ for a square one. An equilibrium equation in the radial direction yields the edge cable force due to the spinning of the corner mass

$$t_{\text{et},m_c} = \frac{F_c \cos\psi}{2} \tag{3.31}$$

¿From Eq. (3.22), this cable force yields the following uniform membrane stress

$$\sigma_{\omega,m_c} = \frac{t_{\text{et},m_c}}{Rh} = \frac{2\varrho m_c \omega^2}{h(1+4\varrho^2)\cos\frac{\pi}{n}} \cos\left[\frac{\pi}{2(6-n)} - \arcsin\left(\frac{4\varrho}{1+4\varrho^2}\right)\right] \tag{3.32}$$

where h is the thickness of the membrane. Comparing the stress due to the density of the web, (3.27), with that due to the corner masses, (3.32), yields

$$\frac{\sigma_{\omega,\rho}}{\sigma_{\omega,m_c}} = k_\sigma \left(\frac{\rho t S^2}{m_c}\right) \tag{3.33}$$

where

$$k_\sigma = \frac{(1+4\varrho^2)}{16\varrho \cos\frac{\pi}{n} \cos\left[\frac{\pi}{2(6-n)} - \arcsin\left(\frac{4\varrho}{1+4\varrho^2}\right)\right]} \tag{3.34}$$

The factor k_σ approaches infinity as the sag-to-span ratio approaches zero. Assuming that the minimum sag-to-span ratio is 1%, the factor k_σ is approximately 15 for $n = 3$, which yields

$$\max\left(\frac{\sigma_{\omega,\rho}}{\sigma_{\omega,m_c}}\right) \approx 15\left(\frac{\rho h S^2}{m_c}\right) \tag{3.35}$$

The product ρt is the surface density of the equivalent membrane. The surface density of the triangular, square and hexagonal mesh can be written as

$$(\rho t)_\mu = \left[\left(\frac{7}{3\sqrt{3}} - 1\right)\mu^2 + \left(9 - \frac{67}{3\sqrt{3}}\right)\mu + 16\sqrt{3} - 18 + \frac{4}{\sqrt{3}}\right]\frac{A_d \rho_d}{\ell} \tag{3.36}$$

where A_d is the cross-sectional area of the web wire and ρ_d is the density of the wire material. The surface density is largest for the triangular mesh:

$$(\rho t)_{\mu=3} = \frac{2\sqrt{3}A_d\rho_d}{\ell} \tag{3.37}$$

Inserting (3.37) into (3.35) and dropping the “max” notation yields

$$\frac{\sigma_{\omega,\rho}}{\sigma_{\omega,m_c}} \approx 52\frac{S}{\ell}\left(\frac{A_d\rho_d S}{m_c}\right) \tag{3.38}$$

Assuming that the web is manufactured from Phillystran PSAS Z15 strands, which has $A_d\rho_d = 0.19$ g/m by Table 3.2. If $S = 100$ m, $\ell = 0.03$ m and $m_c = 10$ kg, the stress ratio $\sigma_{\omega,\rho}/\sigma_{\omega,m_c} = 329$. Thus, the stress due to the centrifugal force on the web is more than 300 times larger than that created by the corner masses and edge cables close to the hub. Increasing the corner masses to 50 kg only decrease the ratio five times. However, for a smaller web with $S = 10$ m the stress ratio is 100 times smaller at 3.29. *Thus, the effects of curving the edge tethers may be negligible for most elements of a large web, but not for a smaller web.*

3.5.2 Analysis by the force method

The analysis by the force method uses the routines described in [40, 55]. For this analysis it is assumed that the side length $S = 100$ m and that the distance between the web strands $d_c = 30$ mm. The interior web elements are assumed to be made from lightest strand in Table 3.2 (PSAS Z15), which has a length density of 0.19 g/m. The radial and edge tethers are assumed to be made from the strand with a length density of 1.22 g/m. As the number of nodes and elements of a web with 30 mm mesh width is too large for our MATLAB routines, a larger mesh width is used in the computations. However, the cross-sectional area of the web strands are scale up so that the total weight of the web remains constant even though the mesh width changes. The total length for different element lengths are given by Eq. (3.10). As a certain distance between individual elements is required by the crawling robots, the comparison will be made for a constant distance, d_c. The relationship between the element length and mesh width is simply

$$d_c = \begin{cases} \sqrt{3}\ell/2 & \text{if} \quad \mu = 3 \\ \ell & \text{if} \quad \mu = 4 \\ \sqrt{3}\ell & \text{if} \quad \mu = 6 \end{cases} \tag{3.39}$$

For a web with $d_c = 30$ mm, the web strands have a cross-sectional area $A_{\text{int}} = 0.19 \cdot 10^{-3}/1540 = 1.23 \cdot 10^{-7}$ m^2, whereas the cross-sectional area of the tethers is $A_{\text{tether}} = 1.22 \cdot 10^{-3}/1540 = 7.92 \cdot 10^{-7}$ m^2. For example, assume that a square web with a square mesh have a mesh width of 2 m. The total length of the web strands for the 30 mm mesh width is 669 km by (3.10), whereas the total length is 9.97 km for the web with 2 m mesh width. The cross-sectional area for the web strands in the model thus becomes $A_{\text{int}} = 669/9.97 \cdot 1.23 \cdot 10^{-7} = 8.25 \cdot 10^{-6}$ m^2. Note that the cross-sectional area of the tethers does not change. The mass in each corner is 10 kg and the angular velocity is 1 rad/s. The exact value of the angular velocity is not relevant as the ratio of the stresses only depends on the masses and dimensions, Eq. (3.38).

Web with four corners and square mesh (QuadQuad)

The element forces of the QuadQuad web is shown in Figure 3.6(a). It is clear that the large force from the corner masses are transferred through the radial tether and to the last row of interior web elements. Thus, the edge tether is subjected to a smaller load that the web strands, which is unsatisfactory. By decreasing the cross-sectional area of the radial tether by a factor 10^6, it is virtually removed from the calculations. The corner loads are now transferred to the edge tether as intended, 3.6(b).

The magnification of cross-sectional area of the web strand for larger mesh widths to keep the web mass constant should produce mesh-independent stresses in the web. The element forces for four different mesh widths (10, 8, 6 and 4 m) are shown in Figure 3.7. The equivalent radial force intensities (N/m) at the centre elements for the four cases are: (a) 144/10 = 14.4, (b) 133/8 = 16.6, (c) 98/6 = 16.3 and (d) 64/4 = 16 N/m. Equation (3.27) yields

$$n_r = \sigma_r t = \frac{1}{2}\rho t \omega^2 b^2 \approx \frac{1}{2} \cdot \frac{0.19 \cdot 10^{-3} \cdot 2 \cdot 0.030}{0.030^2} \cdot 1^2 \cdot 50^2 = 15.8 \text{ N/m} \tag{3.40}$$

Hence, the equivalent root membrane stresses in the square web is similar to the analytical value. An interesting observation is that the circumferential forces do not change very much with the distance from the centre along the centre line for each segment. However, they decrease in the circumferential direction from the centre line towards the radial tether.

The effect of curving the edge cables are shown in Figure 3.8. The forces in the outer element increase as the sag-to-span ratio increases, whereas the root stress does not change much. Note that in Figure 3.8(d), some elements are compressed, which obviously cannot be accepted. For this case, the stress decreases in a significant portion of the web. This may be explained by the fact that the distance from the centre to the edge along the centre lines is shorter than for the other cases ($\varrho = 0$–5%).

The results of the analysis of the QuadQuad web suggest that a straight edge cable produces an adequate force distribution. Radial tethers are not necessary and if they are used, they should be integrated with the web in non-structural way, i.e. in a way so that they cannot share the load with the web elements, as they would change the load paths in a detrimental way.

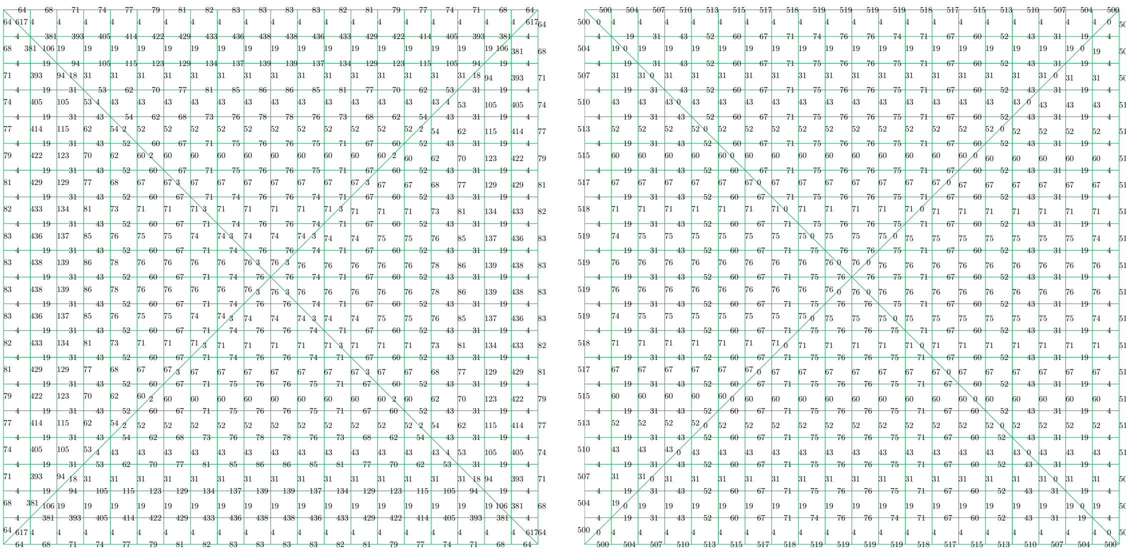

(a) $s = 10$ (b) $s = 10$

Figure 3.6: Element forces (N) in a spinning web with 5 m mesh width: (a) $A_{\text{radial}} = A_{\text{edge}}$ and (b) $A_{\text{radial}} = A_{\text{edge}} \cdot 10^{-6}$ (green denotes tension and red compression).

.

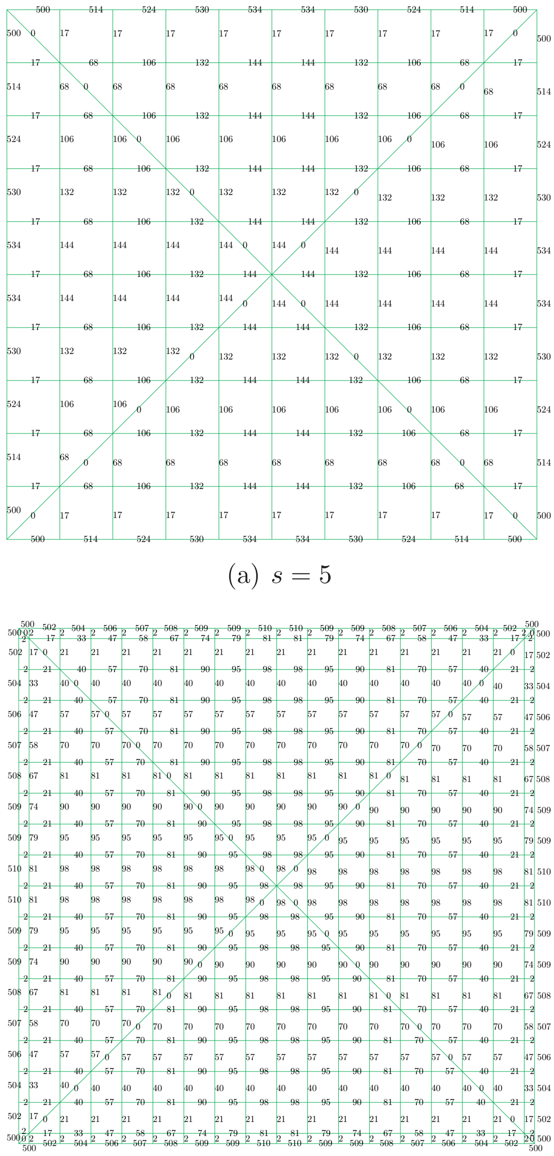

(a) $s = 5$ (b) $s = 7$ (c) $s = 9$ (d) $s = 13$

Figure 3.7: Element forces (N) in a spinning web with different mesh widths: (a) 10, (b) 8, (c) 6 and (d) 4 m (green denotes tension and red compression).

Web with three corners and triangular mesh (TriTri)

The dimensions and properties of the TriTri web are identical to the QuadQuad web above. However, the radial tethers cannot be removed here as they form one side of the triangles; above they could be removed as they formed the diagonals of the squares. As a triangular web has a higher degree of redundancy (static indeterminacy) than a square one and it is thus more difficult to prestress [56]. The results for various TriTri webs are shown in Figure 3.9. From the large number of compressed elements (in red), it is clear that the triangular web cannot be satisfactorily stressed by centrifugal forces. The cause of the prestressing problems is the high degree of static indeterminacy: $s = 89$ for the TriTri web compared to $s = 10$ for the QuadQuad web for the same mesh width. Curving the edge tethers decreases the static indeterminacy slightly, but does not produce a better force distribution. *The only conclusion is that a web with a triangular mesh is very difficult to prestress by spinning and it should thus be avoided in the design of space webs.*

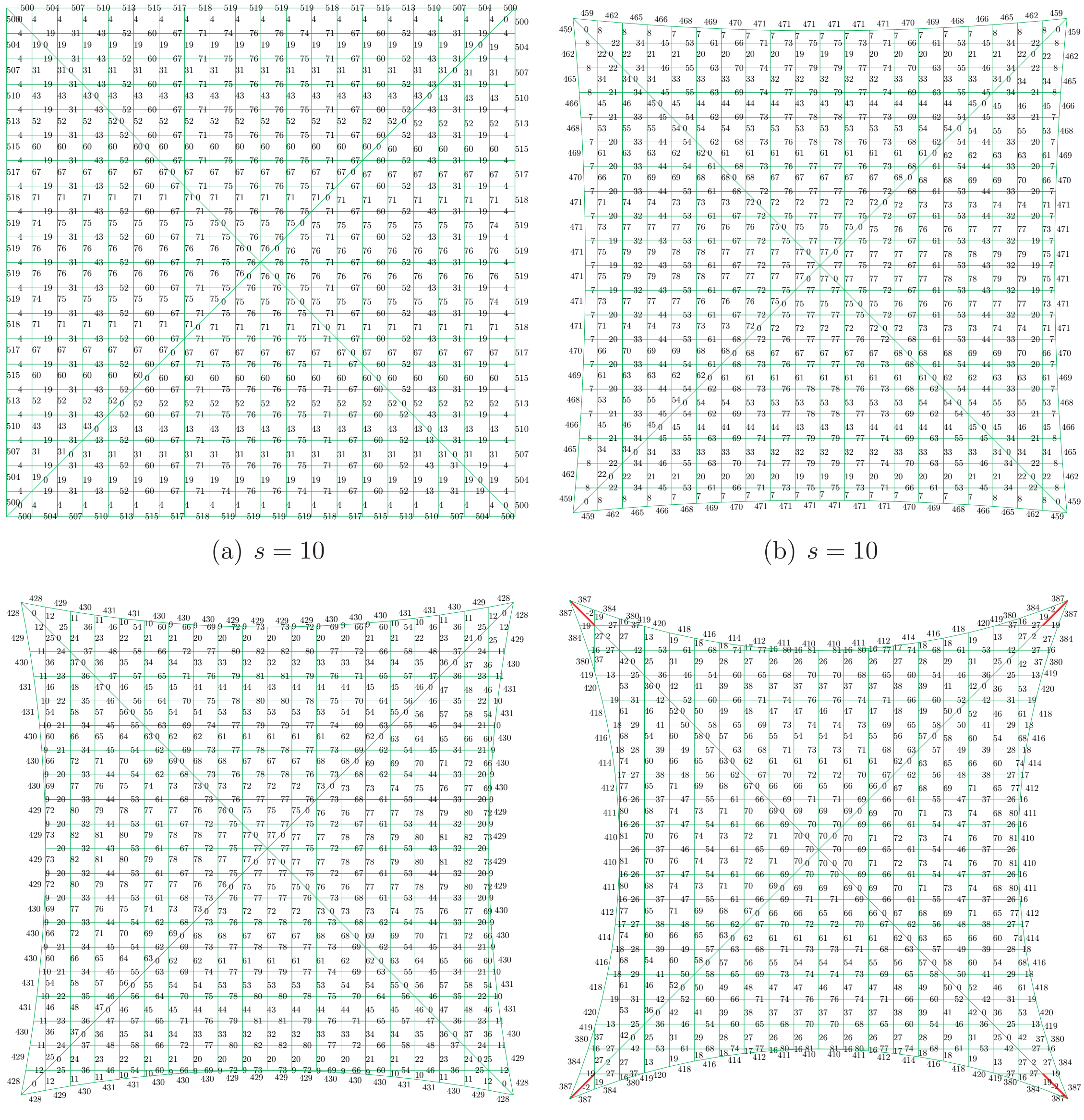

(a) $s = 10$ (b) $s = 10$

(c) $s = 13$ (d) $s = 12$

Figure 3.8: Effect of curving the edge cables (mesh width 5 m): (a) $\varrho = 0\%$, (b) $\varrho = 2.5\%$, (c) $\varrho = 5\%$ and (d) $\varrho = 10\%$ (green denotes tension and red compression).

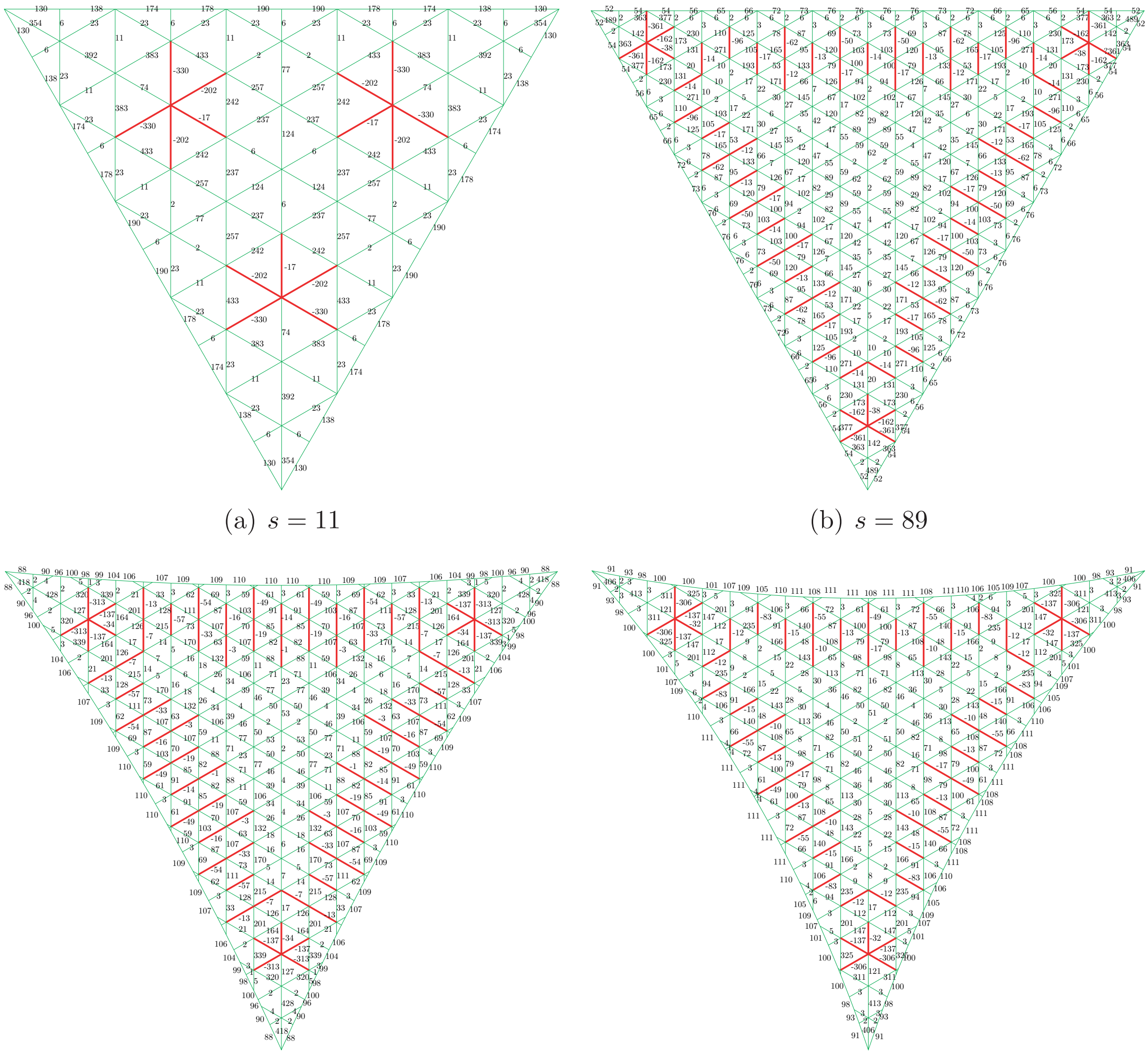

(a) $s = 11$ (b) $s = 89$ (c) $s = 86$, $\varrho = 2.5\%$ (d) $s = 68$, $\varrho = 5\%$

Figure 3.9: Element forces (N) in a spinning web with different mesh widths: (a) 10 and (b)–(d) 5 m (green denotes tension and red compression).

Web with three corners and hexagonal mesh (TriHex)

The hexagonal mesh ought to have greater potential of being prestressed by the centrifugal forces as the degree of static indeterminacy is smaller. However, the mechanisms are no longer orthogonal to the external loads, i.e. the centrifugal loads, which means that the linear force method is not valid for the computation of the element forces. Switching to another method more suited for the analysis of singular systems, e.g. Dynamic Relaxation [60] or Generalised Inverse [53], may yield an accurate solution. This is, however, not required here since the presence of a significant number in-plane mechanisms indicates that the web will undergo severe distortions when subjected to the centrifugal force field. Figure 3.10 shows the 14 in-plane mechanisms (42 mechanisms in total) of a TriHex web with a mesh width of 20.78 m. TriHex webs with mesh widths of 5 and 4 m contain 212 and 350 in-plane mechanisms, respectively. Thus, the problem gets worse quickly as the mesh width decreases. *The conclusion from the analysis of the TriHex web is that it is unsuitable for the space web as it will undergo too severe distortions during spinning due to the presence of a large number of in-plane mechanisms that are activated by the centrifugal forces.*

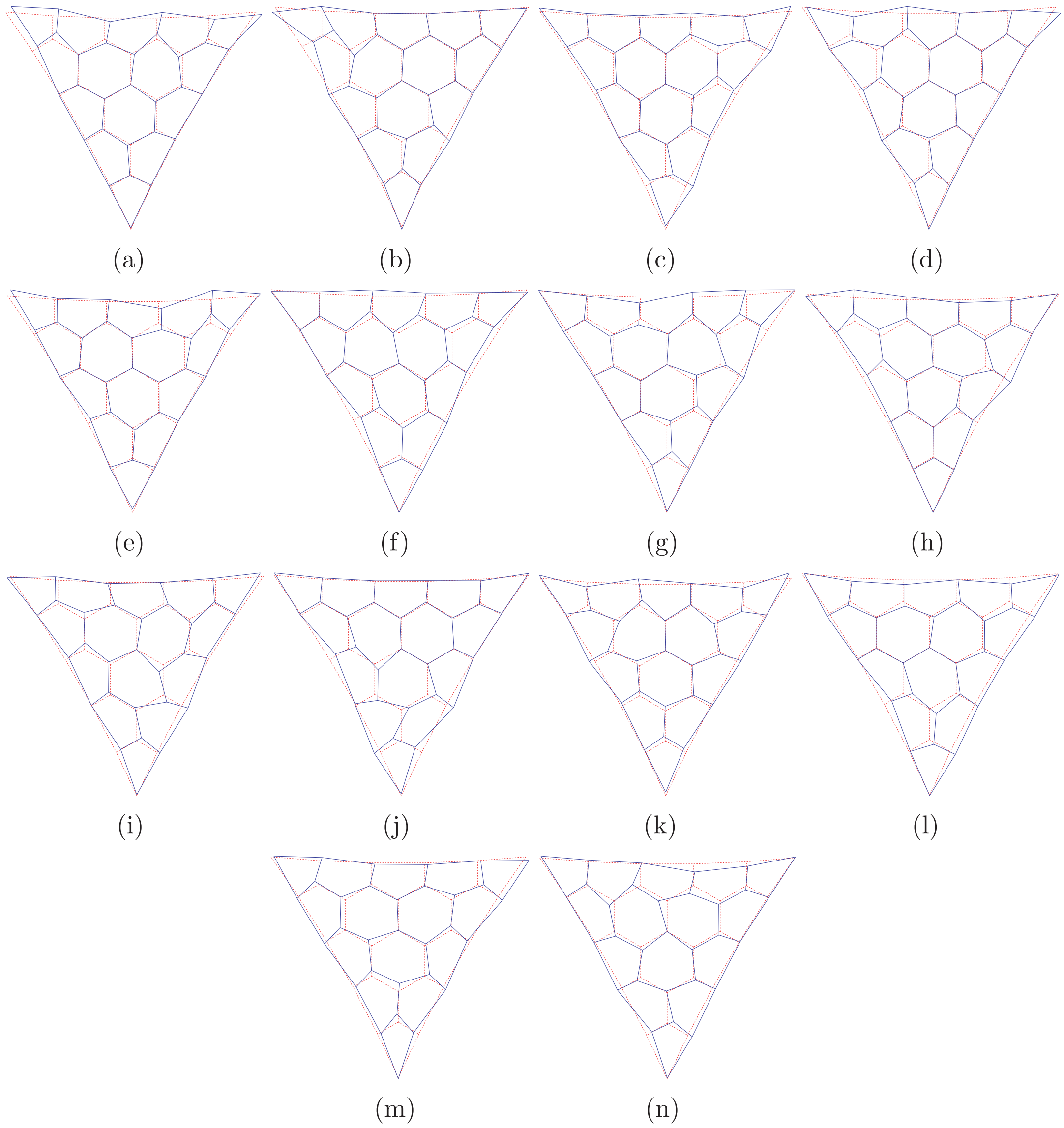

Figure 3.10: The 14 in-plane mechanisms of a TriHex web with 20.78 m mesh width and sag-to-span ratio of 2.5%.

Web with three corners and square mesh (TriQuad)
As both the triangular webs with manufacturing advantages, i.e. TriTri and TriHex, were

discarded due to prestressing and instability problems, it has become necessary to study the triangular web with a square mesh, i.e. TriQuad. Using the same dimensions and material properties as above, the results are shown in Figure 3.11. Figure 3.11(a) shows that some of the radial tether element must be removed as they prevent the formation of tensile forces and create large forces in the web and not in the edge tethers as for the other configuration. Once removed, the forces are in tension everywhere and well distributed, Figure 3.11(b). Curving the edge tether increases the force along the periphery, Figure 3.11(c). Since the vector of centrifugal loads is orthogonal to the subspace of mechanisms, no mechanism is activated and the displacement are kept small, Figure 3.11(d).

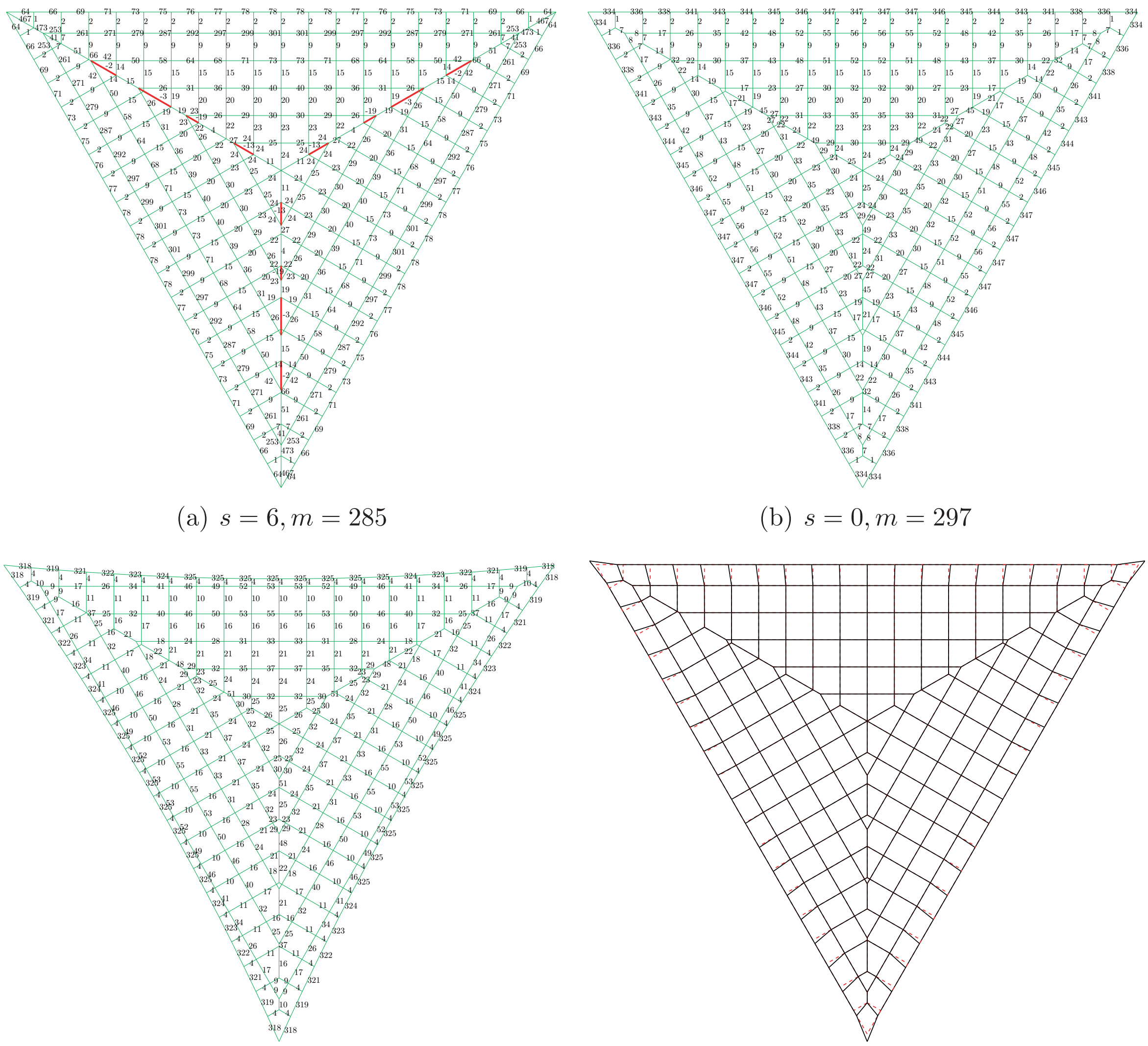

(a) $s = 6, m = 285$

(b) $s = 0, m = 297$

(c) $s = 0, m = 297, \varrho = 2.5\%$

(d) $s = 0, m = 297$

Figure 3.11: A TriQuad spinning web with mesh width 5 m: (a)–(c) element forces and (d) displacements magnified 10 times.

The general conclusion from the prestressing analysis presented above must be that only square meshes will produce a prestressed spinning space web, both for quadratic and triangular geometries.

3.6 Out-of-plane stiffness

A preliminary comparison will be made of the out-of-plane stiffness for the various mesh topologies. The linearised local out-of-plane stiffness for b in-plane bars is [9, 55]:

$$K_\mu = b\frac{t}{\ell} \tag{3.41}$$

Note that the elastic stiffness can be disregarded. For a constant element distance d_c and uniform stress q_0, the out-of-plane stiffness for the various mesh topologies is

$$K_3 = 6\frac{\frac{q_0}{\sqrt{3}}\frac{2}{\sqrt{3}}d_c}{\frac{2}{\sqrt{3}}d_c} \approx 3.464q_0 \tag{3.42a}$$

$$K_4 = 4\frac{q_0 d_c}{d_c} = 4q_0 \tag{3.42b}$$

$$K_6 = 3\frac{\sqrt{3}q_0\frac{d_c}{\sqrt{3}}}{\frac{d_c}{\sqrt{3}}} \approx 5.196q_0 \tag{3.42c}$$

Thus, for identical uniform in-plane stresses, the hexagonal web will be stiffer out-of-plane than both the triangular and the square ones. *Nevertheless, as shown in section 3.5.2, triangular and hexagonal meshes are not adequately stress under the influence of centrifugal forces.*

A global out-of-plane stiffness analysis is performed by inverting the geometric tangent stiffness matrix to obtain the geometric flexibility matrix. Only the centre node is fixed in the analysis. First, an analysis was done with a 100×100 m^2 web and then with a 10×10 m^2 web. The material properties are as in the previous section, the corner masses are 10 kg each and the angular velocity is 1 rad/s. The out-of-plane flexibilities for the 100×100 m^2 web are shown in Figure 3.12. The general trends is that the flexibilities tend to increase as the mesh width decreases, i.e. the web will behave more like a membrane.

An initial analysis of the 10×10 m^2 web showed that the combination of very light web material and small web dimensions yielded too small element forces for a straight edge tether configuration. To increase the forces, the angular velocity was set to 3 rad/s and the edge tether was curved to $\varrho = 2.5\%$. The resulting force distribution is shown in Figure 3.13(a). The uniform force field generated by the edge cable dominates over the centrifugal forces (which can be neglected for small web dimensions). The resulting out-of-plane flexibilities are shown in Figure 3.13(a). By the changes in the angular velocity and edge curvature, the flexibilities are now reasonably low. Exactly what "reasonably low" means is presently not clear; no requirements for the maximum out-of-plane stiffness of a space web has been stated as no mission involving this type of structure has been formulated.

This analysis confirms that for a large web, the forces generated by the curved edge tether can be neglected compared to the forces by the centrifugal force field. In a smaller web, it is the curved edges that prestress the web to an approximately uniform prestress.

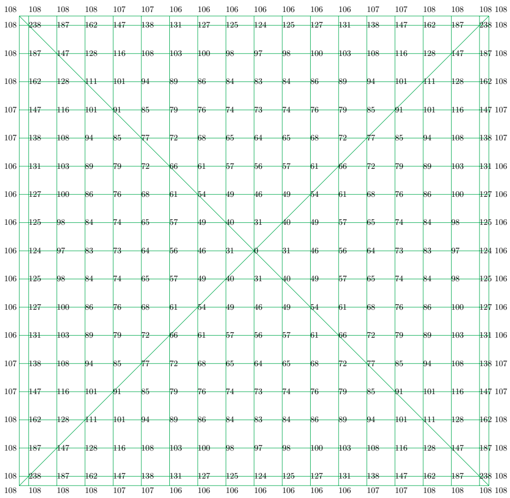

(a) s=9, m=366, max flex = 238 mm/N

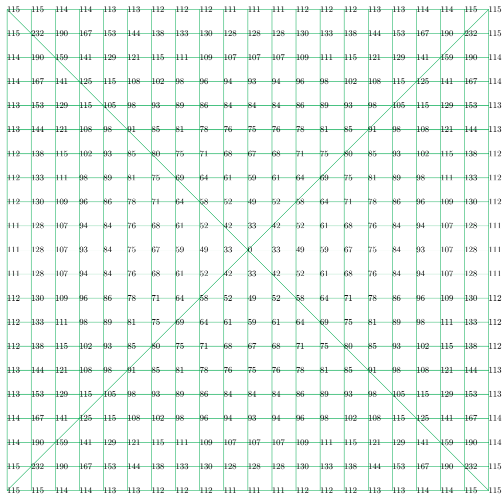

(b) s=10, m=447, max flex = 232 mm/N

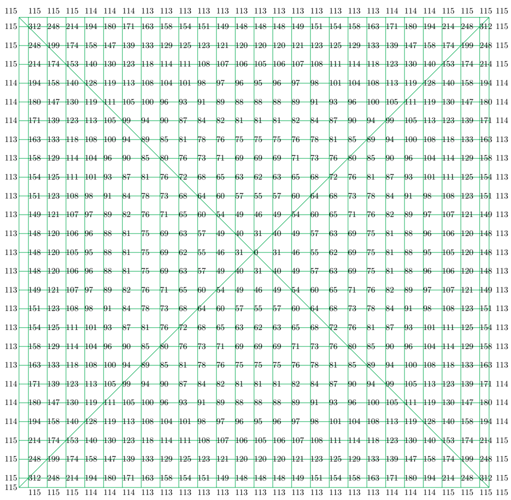

(c) s=13, m=738, max flex = 312 mm/N

(d) s=17, m=1238, max flex = 373 mm/N

Figure 3.12: Out-of-plane flexibilities (mm/N) for a 100 × 100 m^2 spinning web and different mesh widths: (a) 6 m, (b) 5 m, (c) 4 m and (d) 3 m.

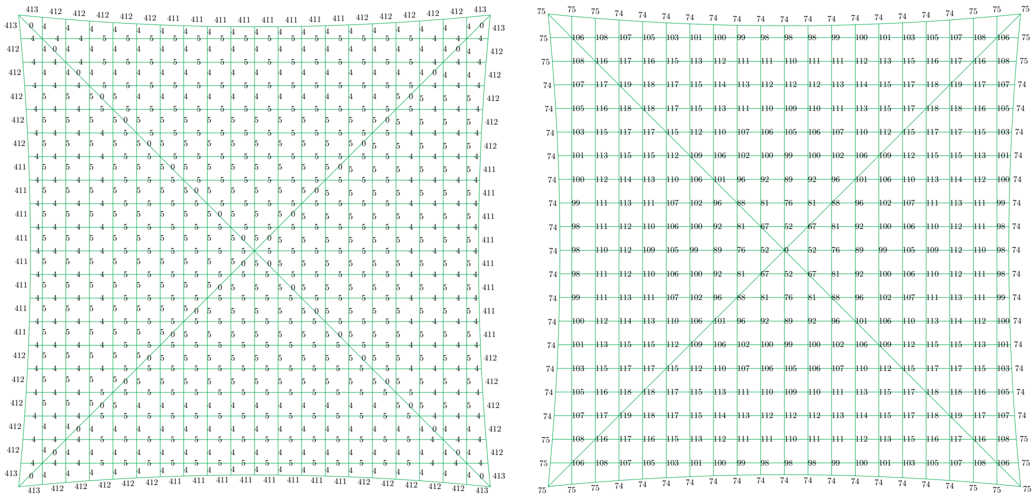

(a) $s = 10, m = 447, \varrho = 2.5\%$ (b) max flex = 119 mm/N

Figure 3.13: Element forces (N) and out-of-plane flexibilities (mm/N) for a 10×10 m^2 spinning web with mesh width 0.5 m.

3.7 Eigenfrequencies and eigenmodes

The eigenfrequencies and free vibration modes of the system are of importance to judge the effects of travelling waves, [4], out-of-plane damping requirements, and other dynamic phenomena, e.g. orbital maneuvering. In this analysis, the material properties and dimensions are the same as in the stress and out-of-plane analyses above with the addition of a mass of 100 kg at the centre node.

The exact tangent stiffness matrix for a stressed three-dimensional truss element with nodes i and j is, [9]:

$$
\begin{aligned}
\boldsymbol{K}^e = & \frac{AE_{ij} - t_{ij}}{\ell_{ij}} \begin{bmatrix} c_x^2 & c_x c_y & c_x c_z & -c_x^2 & -c_x c_y & -c_x c_z \\ c_x c_y & c_y^2 & c_y c_z & -c_x c_y & -c_y^2 & -c_y c_z \\ c_x c_z & c_y c_z & c_z^2 & -c_x c_z & -c_y c_z & -c_z^2 \\ -c_x^2 & -c_x c_y & -c_x c_z & c_x^2 & c_x c_y & c_x c_z \\ -c_x c_y & -c_y^2 & -c_y c_z & c_x c_y & c_y^2 & c_y c_z \\ -c_x c_z & -c_y c_z & -c_z^2 & c_x c_z & c_y c_z & c_z^2 \end{bmatrix} \\
& + \frac{t_{ij}}{\ell_{ij}} \begin{bmatrix} 1 & & & -1 & & \\ & 1 & & & -1 & \\ & & 1 & & & -1 \\ -1 & & & 1 & & \\ & -1 & & & 1 & \\ & & -1 & & & 1 \end{bmatrix}
\end{aligned} \tag{3.43}
$$

where

$$c_x = \frac{x_i - x_j}{\ell_{ij}} \tag{3.44a}$$

$$c_y = \frac{y_i - y_j}{\ell_{ij}} \tag{3.44b}$$

$$c_z = \frac{z_i - z_j}{\ell_{ij}} \tag{3.44c}$$

The consistent mass matrix is [2]:

$$\boldsymbol{M}_C^e = \frac{\rho A_{ij}\ell_{ij}}{6}\begin{bmatrix} 2 & & & 1 & & \\ & 2 & & & 1 & \\ & & 2 & & & 1 \\ 1 & & & 2 & & \\ & 1 & & & 2 & \\ & & 1 & & & 2 \end{bmatrix} \tag{3.45}$$

When computing the eigenfrequencies and eigenmodes of the web it is assumed that the web is completely free in space, i.e. no node is constrained. Hence, six of the frequencies belongs to three global rigid body translations ($f = 0$ Hz) and three rigid body rotations ($f \neq 0$ Hz). The rigid body motions are identified by the eigenmodes and the four lowest non-rigid body motions are plotted.

The eigenfrequencies and corresponding eigenmodes for a 10×10 m^2 (3 rad/s) and the 100×100 m^2 (1 rad/s) QuadQuad webs are shown in Figure 3.14. The element forces are those generated by the centrifugal forces, Figure 3.13(a) for the small web and Figure 3.8 for the large web. It should be noted that the frequency for the rigid body rotations was $f_{10\mathrm{m}} = 0.477$ Hz and $f_{100\mathrm{m}} = 0.159$ Hz. The low eigenfrequencies further confirm the flexible nature of the system. Eigenmodes 3 and 4, Figure 3.14(c) and (d), bear some similarities with in-plane mechanisms, so it is clear that the system has some weak in-plane modes.

3.8 Cable fracture due to micro-meteoroid impact

The risk of micro meteoroid damage to web-like structures was estimated by MacNeal [24]. He observed that design of compression members is usually governed by the elastic stability, whereas for tension members, which can be very thin and long, fracture due to meteoroids will be the critical design consideration [24]. The micro-meteoroid flux in space is

$$N_p = \frac{10^{-17}}{m_p} \quad \text{(particles/m}^2\text{/s)} \tag{3.46}$$

where m_p is the particle mass (kg). The particle mass that will just break the cable is

$$m_p = \frac{4\pi\sigma_u}{v_p^{3/2} v_o^{1/2}}\left(\frac{d}{2.5}\right)^3 \tag{3.47}$$

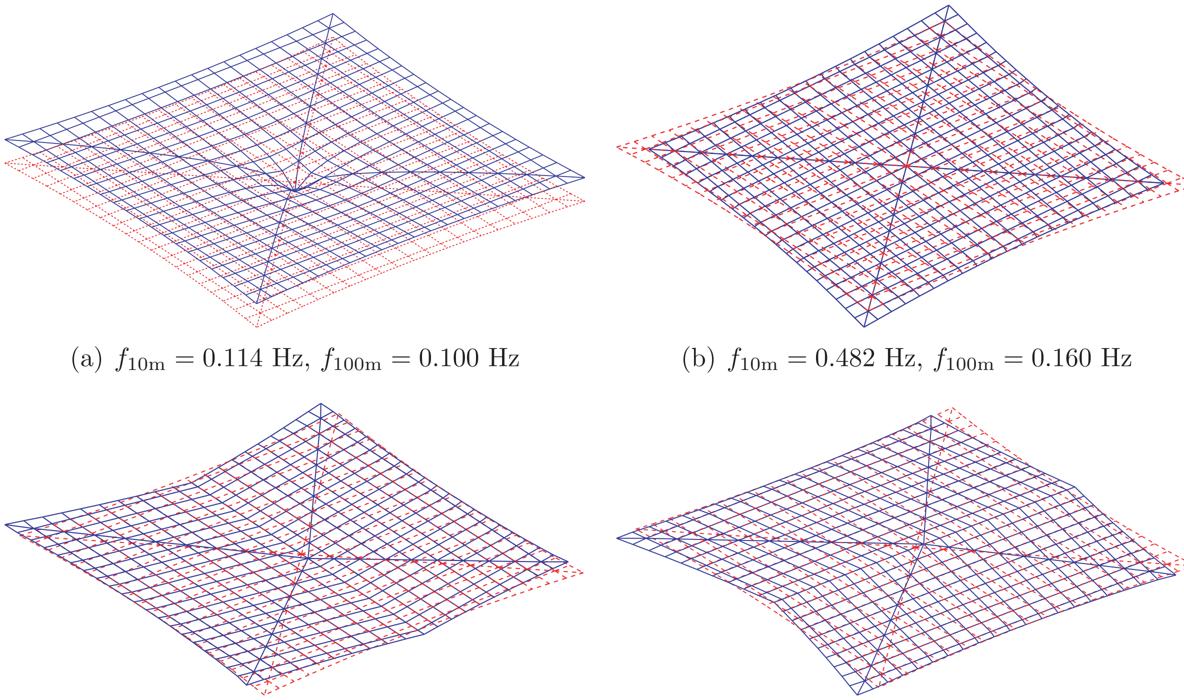

(a) $f_{10\mathrm{m}} = 0.114$ Hz, $f_{100\mathrm{m}} = 0.100$ Hz

(b) $f_{10\mathrm{m}} = 0.482$ Hz, $f_{100\mathrm{m}} = 0.160$ Hz

(c) $f_{10\mathrm{m}} = 0.573$ Hz, $f_{100\mathrm{m}} = 0.219$ Hz

(d) $f_{10\mathrm{m}} = 0.573$ Hz, $f_{100\mathrm{m}} = 0.219$ Hz

Figure 3.14: Four lowest eigenmodes of the QuadQuad web with a sag-to-span ratio of 2.5%: (a) out-of-plane mode,(b) in-plane mode, (c) and (d) similar in-plane mechanism-like modes.

where d is the cable diameter, the mean velocity of meteoroids $v_p = 30$ km/s, the empirical velocity parameter $v_o = 6.5$ km/s and the ultimate strength of the cable material (Zylon®) $\sigma_u = 5.8$ GPa. The number of fractures per unit length of cables per unit time is

$$N_f = \frac{\pi d}{2} N_p \tag{3.48}$$

Combing (3.46)–(3.48) yields the number of fractures for a Zylon® cable:

$$\begin{aligned} N_f &= \frac{1.41 \cdot 10^{-18}}{d^2} \quad \text{(fractures/m/s)} \\ &= \frac{4.46 \cdot 10^{-5}}{d_{\mathrm{mm}}^2} \quad \text{(fractures/m/year)} \end{aligned} \tag{3.49}$$

where d_{mm} is the cable diameter in millimetres.

The space web has a certain degree of redundancy which means that it can still function satisfactorily until a significant portion of the members have been fractured. MacNeal [24] shows that the probability of failure for the structure (or a member composed of several individual elements) is

$$P_f = \left(1 - \mathrm{e}^{-N_f \ell \tau}\right)^s \tag{3.50}$$

where ℓ is the element length, τ is the time and s is the degree of statical indeterminacy (degree of redundancy).

Schuerch and Hedgepeth [49] studied the number of fractures for the LOFT baseline design. A conductor mesh of 2.5 mm wide and 6 μm thick aluminium will experience 450 fractures per year. This equals one fracture per 20×20 m^2 in ten years and will not significantly affect the performance of the LOFT. Fracture of a supporting cable is more critical and the cables were design to produce a single-fracture probability of less than 1% in four years. For the space web, the critical elements are the edge cables, which should be designed using several wires on the local level and as a framework on the global level, Figure 3.15.

For the present space webs, the diameter of the thinnest strand is 0.43 mm, which leads to $4.46 \cdot 10^{-5}/0.43^2 \approx 2.4 \cdot 10^{-4}$ fractures/m/year. For an web element length of 30 mm and a mission time of 10 years, the failure probability due to micro-meteoroids is $P_f = (7.2 \cdot 10^-5)^s$, which is very small. Hence, it can be concluded that the failure risk for a space webs mission is not due to micro-meteoroids.

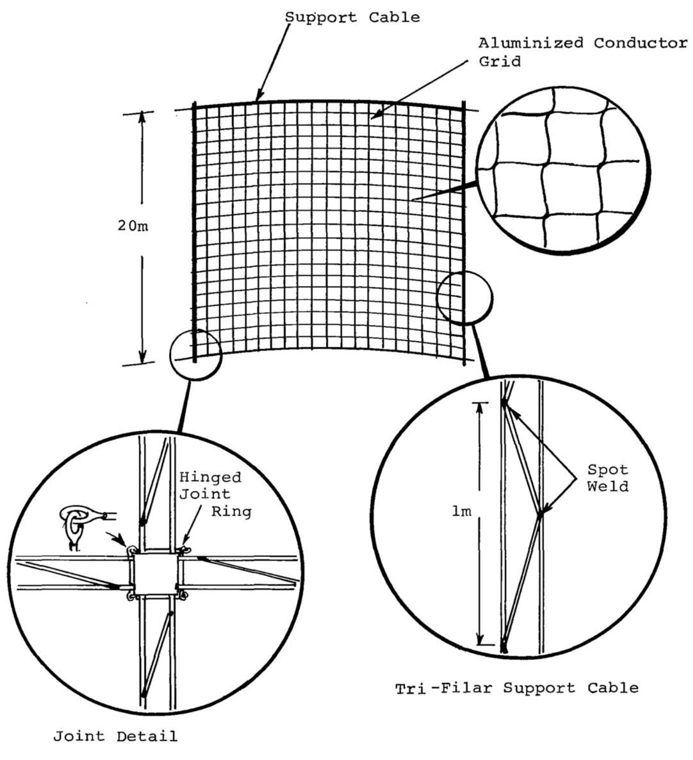

Figure 3.15: Redundant design of the supporting cable in the LOFT antenna, from [49].

3.9 Choice of web architecture

The optimum layout of the web is determined by the following parameters: (i) prestressability, (ii) manufacturability, (iii) mass, (iv) out-of-plane stiffness and (v) eigenfrequencies, but not necessarily in that order. From the analysis above it is clear that only the square mesh is prestressable by centrifugal forces. A square web with a square mesh is better from a manufacturing viewpoint and the out-of-plane stiffness and eigenfrequencies can be adjusted by the angular velocity and corner masses. The remainder of this report will thus only be concerned with the quadratic web with a quadratic mesh.

Chapter 4

Folding patterns for centrifugal deployment

Fundamental to a successful deployment is a good folding pattern. Several folding patterns for large space structures have been proposed for various deployment approaches. A good example is the Miura-Ori [31] for the efficient folding of square solar sails. However, not all of the proposed patterns will work for a deployment driven by centrifugal forces. The literature review below studies the available patterns for spin deployment and identifies the most suitable one for the present application.

4.1 Literature review

4.1.1 Wrapping around a hub

Several studies have dealt with the folding of a circular solar sail by wrapping it around a cylindrical hub, Figure 4.1. The origin of this idea can be traced back to the early 1960s, [10]. Scheel [47] developed a pattern with straight folding lines, Figure 4.2. In 1992, Temple and Oswald from the company Cambridge Consultants performed a study of a 276-m-diameter solar sail. The sail had 36 radial spars emanating from the central hub [10, 28]. Guest and Pellegrino [10] later derived analytical relationships for zero-thickness and thin membranes wrapped around polygonal hubs. Inextensional wrapping around a circular hub is not possible since a curved fold line requires that the membrane is curved in opposite directions [10]. On the other hand, extensional folding around a cylinder is possible, but then the membrane is subjected to localised wrinkling and stretching near the hub [41].

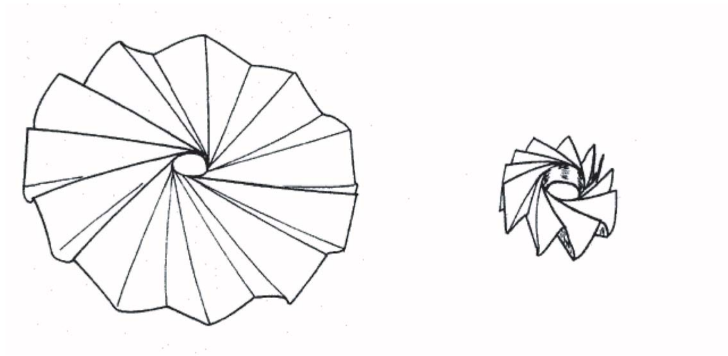

Figure 4.1: Hub-wrapping scheme derived by Guest and Pellegrino, [10].

Recently, Japanese researchers have studied the folding scheme by Scheel [47]. Furuya *et al.* [5] performed deployment experiment of 300-mm-diameter and 12.5 μm thick circular sails. They found that for a given angular velocity, the deployment ratio for a segmented sail folded in a fan-like manner was higher than a single-sheet sail folded according the Scheel pattern. The reason for the higher deployment ratios is that the segmented fan fold pattern generates larger deployment forces than the Scheel pattern. Complete deployment is not possible as the folding of the membrane creates permanent creases which cannot be fully removed. A two-dimensional folding pattern, e.g. Scheel, has a smaller deployment ratio than a two-dimensional one, e.g. fan, due to the constraint of creases [6].

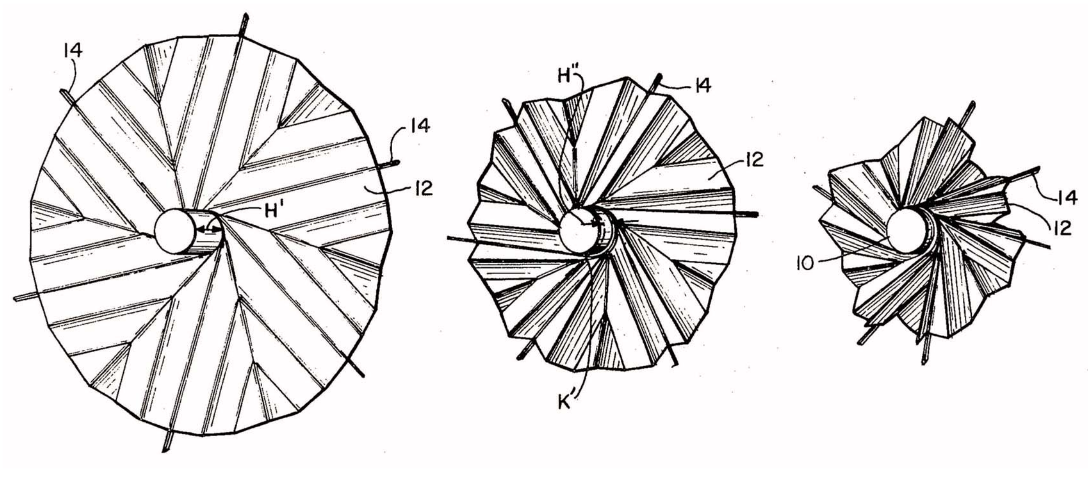

Figure 4.2: Hub-wrapping folding pattern by Scheel [47].

For the present project, the hub-wrapping patterns by Scheel [47] and Guest and Pellegrino [10] have some disadvantages:

- they are developed for circular sheets and not for triangular or square ones, and

- the fold lines do not follow the nodal lines of the web, which makes the development of a folding routine more complicated.

4.1.2 Star pattern

Schuerch and Hedgepeth [49] suggest a folding pattern for the LOFT system where the supporting structure is sheared to be folded into the hub. This pattern produces a star-like shape of the structure being folded, Figure 4.3. For the LOFT system the number of star arms is eight.

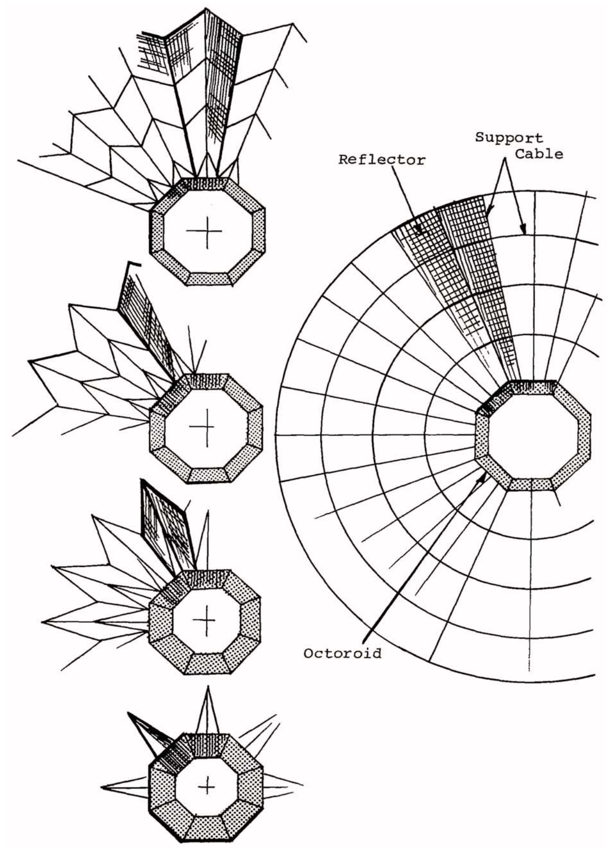

Figure 4.3: Star-shaped folding pattern for the LOFT system, [49].

Melnikov and Koshelev [29] proposed a similar pattern for the folding of spin-deployed circular space structures, Figure 4.4. The arms of the star can then be folded in various ways as discussed in [29]. Two approaches appear especially interesting due to their simplicity: (i) folding of the arms in a zig-zag manner towards the hub or (ii) coiling the arms around the hub as in the hub-wrapping concept. If the arm are folded in a zig-zag manner, the end of the arm must be connected to the hub with a cable so that the deployment rate of the arm end can be controlled. It is seen from Figure 4.4 that the star pattern is not exclusively for circular structures, as the folding is linear towards the hub.

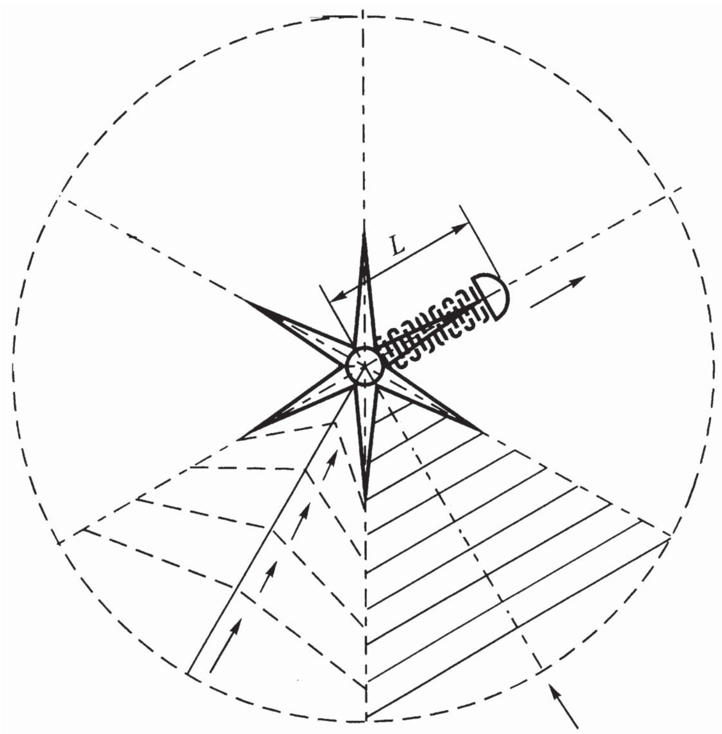

Figure 4.4: Folding of a circular structure towards the hub to obtain a star-like pattern, [29].

4.2 Proposed folding pattern

It was decided that the star pattern was the most suitable one for the space web as the web can be deployed in two stages, which presumably makes it easier to control. Another advantage is the that fold lines coincide with the nodal lines, so that the folding can be done using simple analytical relationships.

Complete star pattern

The first step of the folding is to fold the web into a 'star'-like shape. The y-coordinate of a node on the centre line is described as

$$y = y_0 \sin \frac{\theta}{2} \tag{4.1}$$

where θ is the fold angle along the centre line ($\theta = 180°$ for a fully deployed configuration and $0°$ when completely folded) and y_0 is the y-coordinate of the node in the deployed configuration. Equation (4.1) is the mapping scheme of the nodes along the centre line. For a node i in the first and second quadrants and lying between side lines the mapping scheme is

$$x_i = x_{0i} \cos\phi \tag{4.2}$$

$$y_i = y_{0i} \sin\frac{\theta}{2} + |x_{0i}| \sin\phi \tag{4.3}$$

where

$$\phi = \arccos\left(\frac{\sin\frac{\theta}{2}\cot\frac{\pi}{n} + \sqrt{\tan^2\frac{\pi}{n} + \cos^2\frac{\theta}{2}}}{\tan\frac{\pi}{n}\left(1+\cot^2\frac{\pi}{n}\right)}\right) \tag{4.4}$$

Equations (4.2) and (4.3) describe the movement of a node in the x–y plane during the 'star' folding process. Figure 4.5 shows how nodes at positions 1/4, 1/2 and 3/4 of the fold line moves from the fully deployed to the fully folded configurations; it is evident that the movement is not linear.

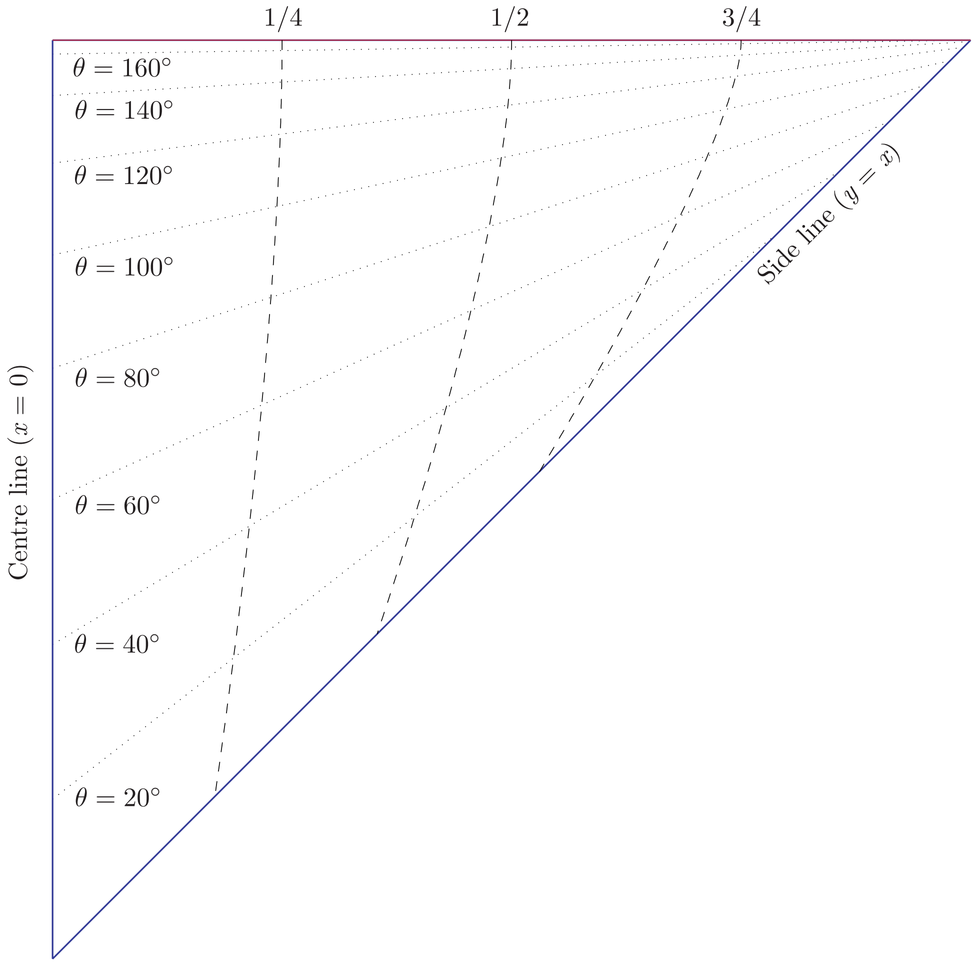

Figure 4.5: Movement of nodes at positions 1/4, 1/2 and 3/4 along the fold line for a square web. Note that the figure shows only one eighth of the quadratic web.

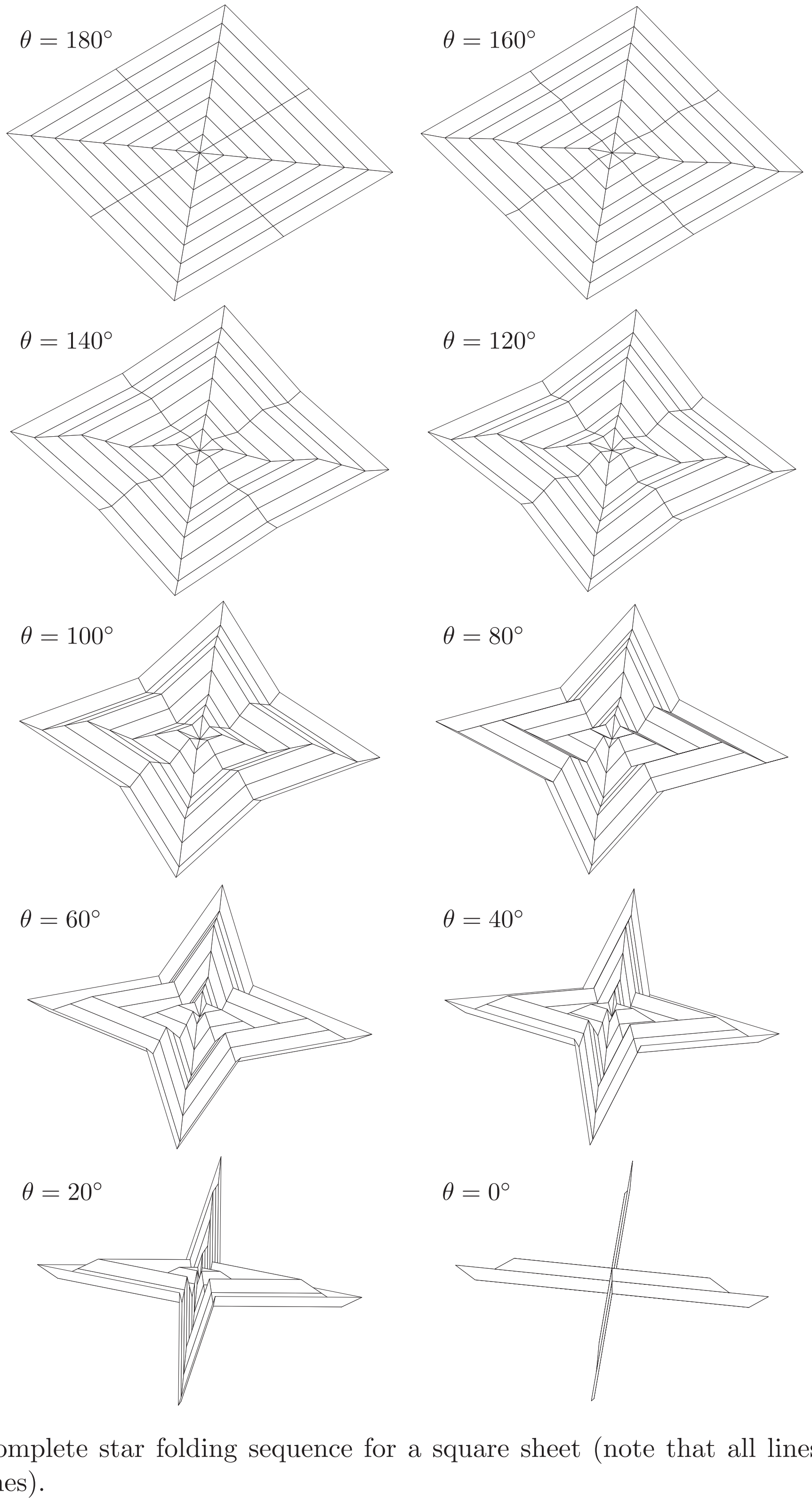

Figure 4.6: Complete star folding sequence for a square sheet (note that all lines are not fold lines).

Since the surface in the z-direction has a zig-zag pattern, the mapping for the z-coordinate is a bit more complex. Assuming that the distance between fold lines is 2Δ in the interior and Δ at the centre and along the edges, the relative position of the node between two fold lines is computed as

$$\chi = y_{0i}/2\Delta - \lfloor y_{0i}/2\Delta \rfloor \tag{4.5}$$

where $\lfloor x \rfloor$ rounds x to the nearest integer towards $-\infty$. The mapping scheme for the z-coordinate becomes

$$z_i = \begin{cases} \pm 2\chi\Delta \cos\dfrac{\theta}{2} & \text{if} \quad \chi \leq 0.5 \\ \pm 2(1-\chi)\Delta \cos\dfrac{\theta}{2} & \text{if} \quad \chi > 0.5 \end{cases} \tag{4.6}$$

where the '$-$' sign holds if $\lfloor y_{0i}/2\Delta \rfloor$ is an even number and the '+' sign otherwise.

In summary, the star pattern is neatly described by analytical relationships which maps the coordinates from a given position of the deployed configuration to a position of the folded configuration described by the single variable θ. In this way, the curved edges of the web can be mapped to the folding pattern even though the edge nodes do not lie on the fold lines.

4.2.1 Incomplete star pattern

If the central satellite is modelled as a point mass with inertia, the complete star mapping scheme, which folds the web towards the centre point, can be used. If, however, the central satellite is modelled with shell elements and its physical dimensions, the complete star mapping cannot be used. In such a case, the star mapping must be modified to have the two innermost rings of elements deployed. The starting configuration for this scheme is the star folding with folding angle $\theta = 0°$ (all nodes of the arms are positioned along straight lines). From this position, the two inner rings of elements are deployed. Note that the incomplete star mapping only works for works for fold angle $\theta = 0$, since the arms have to be completely folded before the two innermost rings can be deployed. The incomplete star mapping scheme is written as

$$x_i = \begin{cases} x_{0i}\cos\phi + 2\Delta \mathrm{sgn}(x_{0i}) \tan\frac{\pi}{n}\left(1 - \sin\frac{\pi}{n}\right) & \text{if} \quad |x_{0i}| > 2\Delta\tan\frac{\pi}{n};\ y_{0i} > 2\Delta \\ x_{0i} & \text{if} \quad |x_{0i}| \leq 2\Delta\tan\frac{\pi}{n} \end{cases} \tag{4.7}$$

and

$$y_i = \begin{cases} y_{0i}\sin\frac{\theta}{2} + |x_{0i}|\sin\phi + 2\Delta\tan\frac{\pi}{n}\left(1 - \cos\frac{\pi}{n}\right) & \text{if} \quad |x_{0i}| > 2\Delta\tan\frac{\pi}{n}; y_{0i} > 2\Delta \\ 2\Delta & \text{if} \quad |x_{0i}| \leq 2\Delta\tan\frac{\pi}{n};\ y_{0i} \geq 2\Delta \\ y_{0i} & \text{if} \quad y_{0i} < 2\Delta \end{cases} \tag{4.8}$$

The z-coordinates are basically unchanged, except for the nodes lying within the first two element rings defined by the y-coordinate:

$$z_i = \begin{cases} \text{Eq. (4.6)} & \text{if} \quad y_{0i} \geq 2\Delta \\ 0 & \text{if} \quad y_{0i} < 2\Delta \end{cases} \tag{4.9}$$

A comparison between the complete and incomplete star mapping schemes is shown in Figure 4.7. In order to facilitate a tight wrapping around the hub, the square deployed part of the web is made circular while preserving the length of the all elements. This last change is very important since it otherwise will be a significant space between the coiled web and the surface of the cylindrical hub.

A disadvantage with the proposed incomplete star pattern is that the size of the deployed inner portion of the web is dependent on the mesh size of the web, which may produces an unrealistically large radius of the stowed package. However, a general folding routine, where the fold lines do not have to coincide with the nodal lines, was deemed too complicated and costly to implement for the present project.

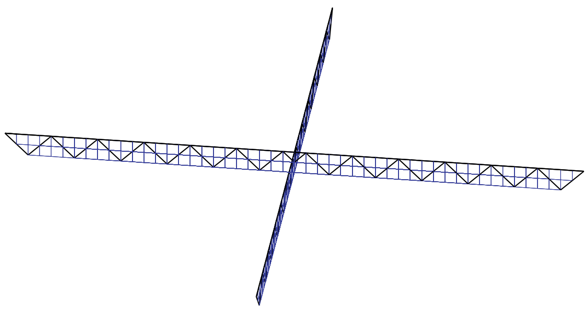

(a)

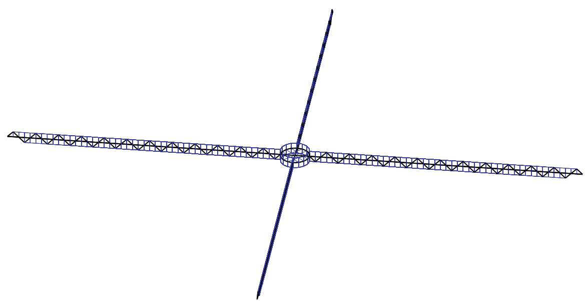

(b)

Figure 4.7: Visual comparison of the (a) complete and (b) incomplete star patterns.

4.2.2 Zig-zag folding of star arms

The second step is to fold the 'star' arms towards the central satellite using zig-zag folds. This step is somewhat simpler than the previous step since the nodes only move in-plane and a variant of the zig-zag folding, Eq. (4.6), can be used. The routine outlined below only works for an equal division between the node along the star arms. The radius from the centre of the web to node i on the star arm is

$$r_i = \sqrt{x_i^2 + y_i^2} \tag{4.10}$$

and the angle of the arm is computed as

$$\beta = \begin{cases} \arcsin \dfrac{y_i}{r_i} & \text{if} \quad \dfrac{x_i}{r_i} \geq 0 \\ \pi - \arcsin \dfrac{y_i}{r_i} & \text{if} \quad \dfrac{x_i}{r_i} < 0 \end{cases} \tag{4.11}$$

The position of the folded node measured along the initial arm orientation is, Figure 4.8,

$$r_{i,1} = r_0 + (r_i - r_0)\sin\frac{\theta}{2} \tag{4.12}$$

where r_0 is the radius of the to the first node on the star arm, Figure 4.8. The distance perpendicular to the initial arm orientation is computed as follows. The relative position of the node between two fold lines is

$$\chi_a = (r_i - r_0)/2\Delta_a - \lfloor (r_i - r_0)/2\Delta_a \rfloor \tag{4.13}$$

which is similar to Eq. (4.5). The movement of the node perpendicular to the initial orientation is thus

$$d_i = \begin{cases} \pm 2\chi_a \Delta_a \cos\dfrac{\theta}{2} & \text{if} \quad \chi_a \leq 0.5 \\ \pm 2(1-\chi_a)\Delta_a \cos\dfrac{\theta}{2} & \text{if} \quad \chi_a > 0.5 \end{cases} \tag{4.14}$$

where the '$-$' sign holds if $\lfloor (r_i - r_0)/2\Delta_a \rfloor$ is an even number and the '+' sign otherwise. The radius of the new node position is

$$r_{i,2} = \sqrt{r_{i,1}^2 + d_i^2} \tag{4.15}$$

and the new angle is

$$\beta_{i,2} = \beta + \arctan\frac{d_i}{r_{i,1}} \tag{4.16}$$

which yields the new node positions:

$$x_{i,2} = r_{i,2}\cos\beta_{i,2} \tag{4.17a}$$

$$y_{i,2} = r_{i,2}\sin\beta_{i,2} \tag{4.17b}$$

$$z_{i,2} = z_i \tag{4.17c}$$

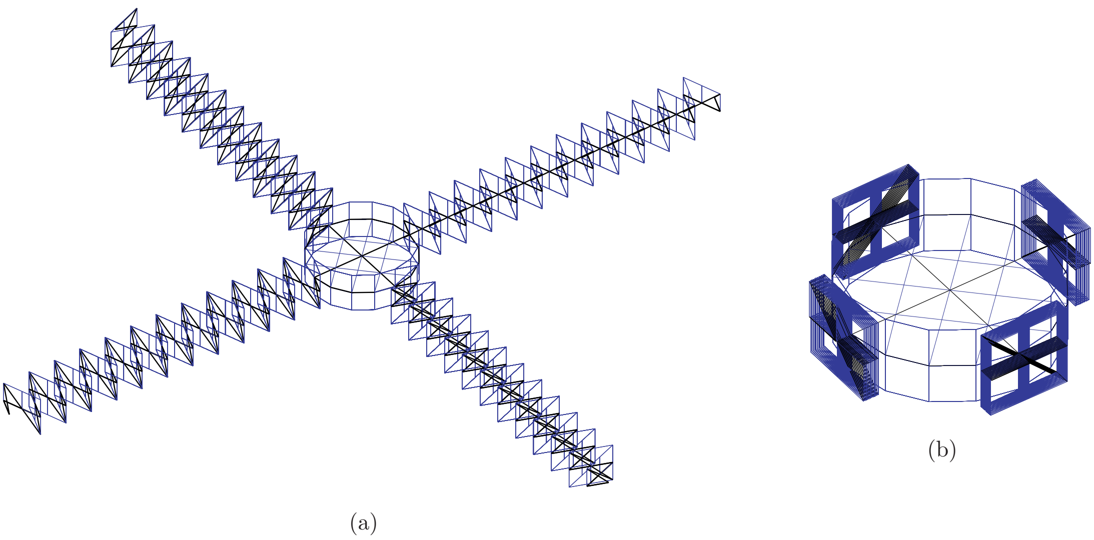

Figure 4.9: Zig-zag folded star arms: (a) 40° and (b) 0° folding angle.

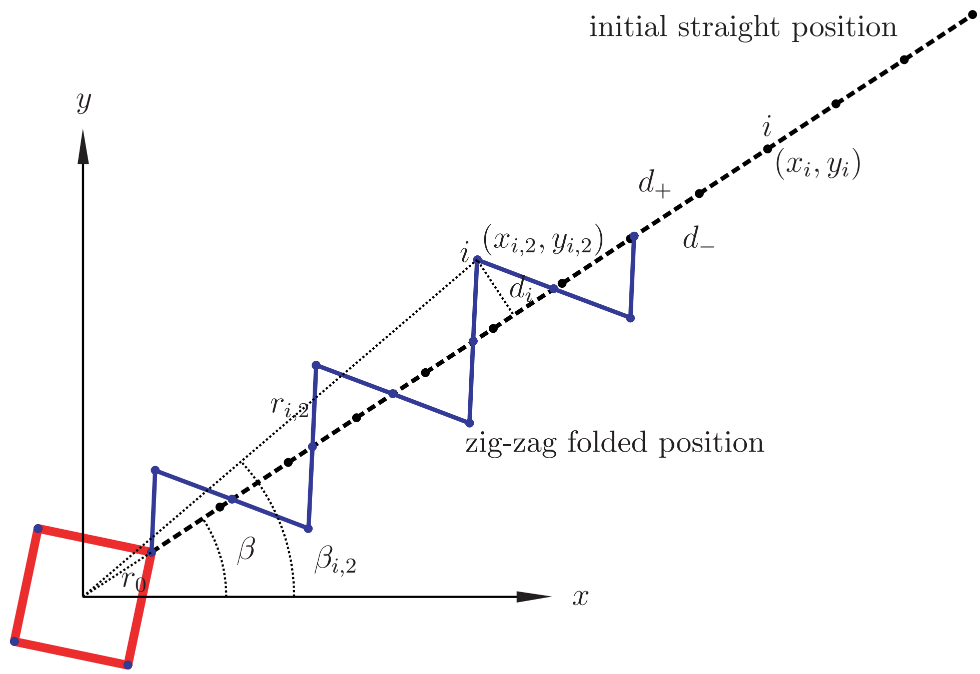

Figure 4.8: Zig-zag folding of a star arm.

4.2.3 Wrap-around folding of star arms

Another folding scheme that is attractive due to its simplicity is the wrap-around or coiling scheme, where the star arms are wrapped around the central satellite. It is important also for this scheme that the folding is done in a polygonal way and not by a smooth curve since the fold lines must be positioned where the nodes are. Otherwise, the elements will become too short for the web to deploy properly. A mapping scheme, which preserves the lengths of all members can be written using the Denavit-Hartenberg convention, [3]. As the movement of the nodes during the folding only is in-plane, the Denavit-Hartenberg transformation matrix can be simplified to

$$\mathbf{A}(\alpha) = \begin{bmatrix} \cos\alpha & -\sin\alpha & 0 & \Delta_w \cos\alpha \\ \sin\alpha & \cos\alpha & 0 & \Delta_w \sin\alpha \\ 0 & 0 & 1 & 0 \\ 0 & 0 & 0 & 1 \end{bmatrix} \tag{4.18}$$

where Δ_w is the distance between the fold lines or mesh width, α_i is the rotation angle relative to the previous segment of the star arm. for the first element, the folding angle is set to $\beta + \alpha_i/2 - \pi/2$ as the whole star arm first must be folded 90° from its initial angle β, which found from Eq. (4.11). The folding of the star arms with $\alpha = 0$ is shown in Figure 4.10(a). To produce a circle of the star arms that encloses the deployed portion of the web, the following value for the relative rotation of the star arm segment must be chosen:

$$\alpha = -\left[\pi - 2\arccos\left(\frac{\Delta_w}{2\sqrt{r_0^2 + \frac{\Delta_w^2}{4}}}\right)\right] \tag{4.19}$$

The x- and y-coordinates of the position of the first node of the star arm ($r_1 = r_0 + \Delta_w$) after folding is found as elements (1,4) and (2,4), respectively, in $\mathbf{A}(\beta - \pi/2 + \alpha/2)$. Similarly, the position of node i is found as positions (1,4) and (2,4) in the resulting matrix from the product $\mathbf{A}(\beta - \pi/2 + \alpha/2)\mathbf{A}(\alpha)^{i-1}$. Applying the Denavit-Hartenberg transformation for all nodes of the star arms yields the folded configuration in Figure 4.10(b). Since the star arms in this position lie on top of each other, problems might arise in the finite element simulations. Therefore, a slight change in the relative rotation angle α is implemented: for node i the relative rotation is set to

$$\alpha_i := \alpha - (i-1)\vartheta \tag{4.20}$$

where ϑ is chosen as percentage of α. It is found that $\vartheta = 0.01\alpha$ yields enough separation between the star arms, Figure 4.10(c). Hence, the x- and y-coordinates for node i is now found at positions (1,4) and (2,4) in the matrix $\mathbf{A}(\beta - \pi/2 + \alpha/2)\mathbf{A}(\alpha_1)...\mathbf{A}(\alpha_{i-1})\mathbf{A}(\alpha_i)$, where α_i is given by (4.20).

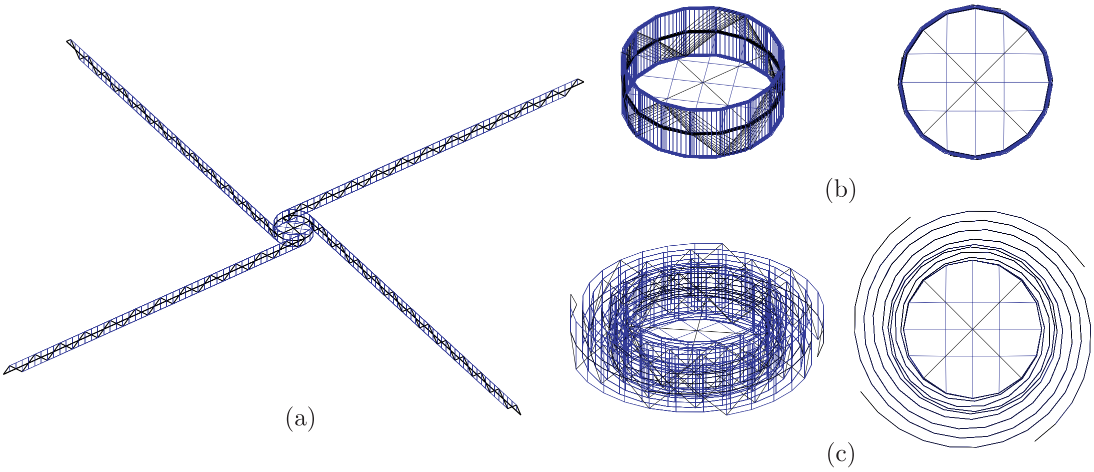

Figure 4.10: Hub-wrapping folding of the star arms: (a) initial 90 ° folding, (b) most compact folding with square (aerial and top views), and (c) with separation between the arms.

Chapter 5

Deployment

The most interesting, but also the most complicated, part of the project is the deployment simulations. This part is divided into three sections: (i) selection of deployment control strategy, (ii) development of an analytical model for quick assessment of the effect of changing various parameters and (iii) deployment simulations with the finite element software LS-DYNA.

5.1 Deployment strategies

The most simple deployment strategy would be to coil the star arms around the centre satellite and then provide a initial angular velocity large enough to deploy the web. However, as the system conserves the angular momentum, the final spin would be too slow, as shown by the following calculation. The total angular momentum before release of the web and the corner masses, Figure 5.1(a), is

$$\mathcal{L}_0 = \left(\frac{m_h}{2} + m_w + 4m_c \right) r_0^2 \omega_0 \tag{5.1}$$

where m_h is the mass of the hub, m_w is the total mass of the web, m_c is the mass at each corner, r_0 is the radius of the hub, and ω_0 is the initial angular velocity. After deployment, Figure 5.1(b), the angular momentum is

$$\mathcal{L}_1 = \left(\frac{m_h}{2} \left(\frac{r_0}{S} \right)^2 + \frac{m_w}{6} + 2m_c \right) S^2 \omega_1 \tag{5.2}$$

The law of the conservation of the angular momentum yields the ratio of the angular velocities after and before the deployment:

$$\frac{\omega_1}{\omega_0} = \frac{\frac{m_h}{2} + m_w + 4m_c}{\frac{m_h}{2} \left(\frac{r_0}{S} \right)^2 + \frac{m_w}{6} + 2m_c} \left(\frac{r_0}{S} \right)^2 \tag{5.3}$$

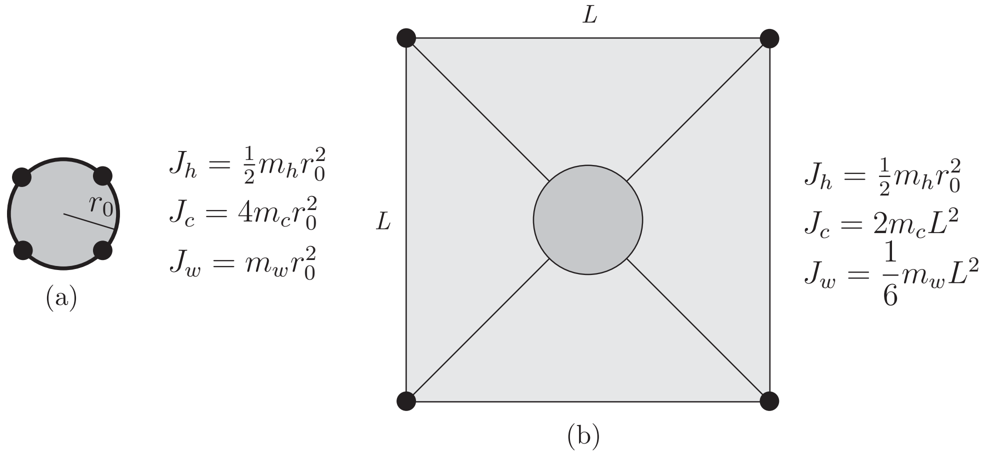

Figure 5.1: Angular momentum of the system: (a) before deployment and (b) after deployment.

Assume that $S = 100$ m, $r_0 = 1$ m, $m_c = 10$ kg and $m_h = 100$ kg. With a 30 mm mesh width, the total weight of the web (including edge tethers) is 122 kg. Inserting these values into (5.3) yields $\omega_1/\omega_0 = 5.26 \cdot 10^{-4}$. Hence, with $\omega_0 = 12.6$ rad/s (2 rps), the final angular velocity will be $6.62 \cdot 10^{-3}$ rad/s or 3.8 revolutions per hour, which is way too slow. Compare this value with that of the 1500-m-diameter LOFT that was designed to spin with one revolution in about 11 minutes, [49]. Decreasing the size of the web to $L = 10$ m and keeping the same hub diameter and masses, except for the mass of the web, which becomes 1.22 kg, yields $\omega_1/\omega_0 = 4.41 \cdot 10^{-2}$. Hence, with an initial spin of 2 rps, the final spin rate is 5.3 rpm. It appears that some adjustments of masses to obtain a desired final angular velocity is possible for a smaller web. However, for a larger one, angular momentum must be added to the system during deployment to obtain a sufficiently high angular velocity for the deployed web. As mentioned in section 2.2, the spin up system of the LOFT was programmed to provide angular momentum until 60% of the structure had been deployed.

Melnikov and Koshelev [29] initially discussed that the angular momentum ideally should be applied both to the central hub and to the periphery of the structure being deployed, e.g. by a pair of diametrically opposite thrusters. Such a layout would require that the thrusters have their own attitude control system to keep the jet motion within the plane of rotation. Melnikov and Koshelev later disregarded this system on grounds of complexity and suggested that the angular momentum should be applied to the central hub. They initially considered several ways of applying this momentum [29]:

- flywheel that initially run at a high speed,
- gas thrusters with different time-dependent control laws for the thrust, and
- electric motors with rigid or drooping characteristics.

The system with a flywheel that runs at a very high speed is similar to the case where the packaged system is first spun and then deployed, as described earlier in this section. For this case, the initial kinetic energy of the stowed system is

$$
\begin{aligned}
\mathcal{E}_0 &= \frac{1}{2}\left(\frac{m_h}{2} + m_w + 4m_c\right) r_0^2 \omega_0^2 \\
&= \frac{1}{2}\left(\frac{100}{2} + 122 + 4 \cdot 10\right) \cdot 1^2 \cdot 12.6^2 \approx 16.83 \text{ kJ}
\end{aligned}
\tag{5.4}
$$

whereas the kinetic energy of the deployed system is

$$
\begin{aligned}
\mathcal{E}_1 &= \frac{1}{2}\left(\frac{m_h}{2}\left(\frac{r_0}{L}\right)^2 + \frac{m_w}{6} + 2m_c\right) L^2 \omega_1^2 \\
&= \frac{1}{2}\left(\frac{100}{2}\left(\frac{1}{100}\right)^2 + \frac{122}{6} + 2 \cdot 10\right) \cdot 100^2 \cdot (6.62 \cdot 10^{-3})^2 \approx 8.84 \text{ J}
\end{aligned}
\tag{5.5}
$$

Since the energy of the system also is conserved, the excessive kinetic energy creates undesirable oscillations and eventually failure of the structure. Therefore, the excessive kinetic energy must be removed from the system during deployment.

When the momentum is provided by thrusters, the angular momentum is accumulated while the system is being rotated. As there is no requirements to compensate this momentum by a counter-rotating systems, Melnikov and Koshelev [29] state that the theoretical solution of a constant or time variable momentum suggests that the deployment becomes oscillatory. Ground testing with gas thrusters is also problematic.

With an electric drive solution, the angular momentum of the system being deployed has to be compensated by, e.g., a counter-rotating flywheel [29]. The drive characteristics of the electric rotor connecting the deploying structures and the counter-rotating systems is fundamental in order to control the deployment. Adjusting the momentum of the electric drive to keep the angular velocity constant leads to the following drawbacks, [29]:

- the centrifugal forces on the structure will be very large at the end of deployment, and
- oscillatory, unstable deployment dynamics with first coiling off and then coiling on again.

Melnikov and Koshelev [29] suggest that a drooping characteristic of the electric drive, i.e. the momentum is increased as the angular velocity is decreased, and vice versa, would eliminate the drawbacks above and provide the following advantages:

- The initial angular velocity could be sufficiently high to initiate deployment,
- a high deployment velocity and a short deployment time is possible,

- the deployment would be smooth without the coiling on–coiling off dynamic phenomena, and
- a low angular velocity at the end of the deployment produces acceptable centrifugal forces.

The drooping characteristic of the electric motor produces a stable, self-controlled system: if the system suddenly was slowed down, the momentum is increased to increase the angular velocity; on the contrary, if the system was accelerated, the momentum would decrease to slow down the rotations.

5.2 Analytical model

Simple analytical models can be used to describe the deployment dynamics qualitatively. First, equations are derived that describe the deployment of an arbitrary number of point masses symmetrically attached around a cylindrical central hub. If the mass of the space web is small compared to the point masses at the ends of the cables this would be a good first model of the deployment. Then, models of the deployment of more complicated space webs are derived or obtained from literature.

The derivation of the equations follows the same principles used by Melnikov and Koshelev [29] to describe the deployment of solid reflectors and tether systems from a rotating central satellite. Hedgepeth [13] also used a similar model for the LOFT system. The analytical models are based on the following basic assumptions:

- The deployment is symmetric relative to the central axis.
- The radial tethers are straight.
- There is no out-of-plane motion.
- Potential energy effects due to gravity and the elasticity in the cables are neglected.
- The energy dissipation caused by deformation, friction and environmental effects is neglected.

Three coordinate systems are required for the model, Figure 5.2. All of them have one axis $\boldsymbol{e}_3^{(i)}$ directed along the axis of rotation and two axis, $\boldsymbol{e}_1^{(i)}$ and $\boldsymbol{e}_2^{(i)}$, in the plane of deployment. The first coordinate system is fixed in space with its origin in the centre of the central satellite. The second coordinate system is rotating with an angular velocity $\omega(t) = \dot{\varphi}_1$ around the same origin as the first. The third system is attached at the periphery of the central satellite, where the radial arm or tether from the central satellite to the end mass is attached. Axis $\boldsymbol{e}_1^{(2)}$ points in the direction of the tether, $\boldsymbol{e}_3^{(2)}$ is parallel to the axis of rotation, and $\boldsymbol{e}_2^{(2)}$ is perpendicular to $\boldsymbol{e}_3^{(2)}$ and $\boldsymbol{e}_1^{(2)}$.

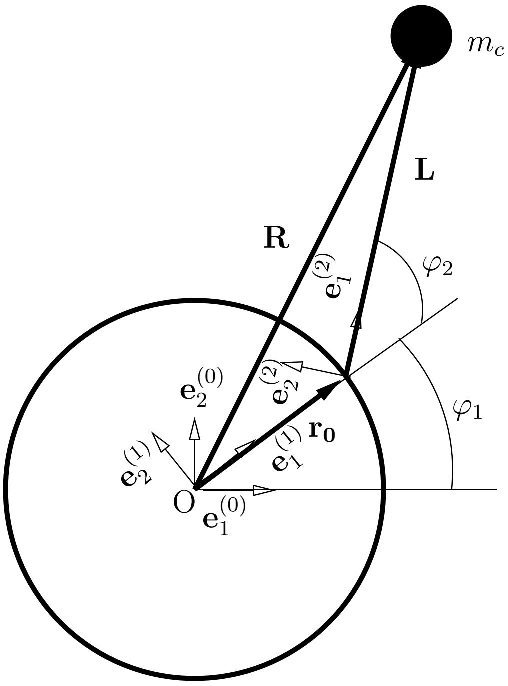

Figure 5.2: The analytical model for a point mass. The description of the equation systems is the same for all the analytical models presented here.

5.2.1 Variation of the angular momentum

Due to the applied momentum and the forces in the tethers, the angular momentum will change. Therefore, the change of angular momentum for the central cylinder around its axis of rotation is:

$$J_z\dot{\omega} = M + nNr_0 \sin\varphi \tag{5.6}$$

where J_z is the moment of inertia of the centre hub around the axis of rotation, M is the applied momentum, n is the number of radial tethers, N is the tensile force in each tether. The moment of inertia for the hub is

$$J_z = \frac{1}{2}m_h r_0^2 \tag{5.7}$$

5.2.2 Model 1: deployment of point mass

This model can be used if the corner masses are much heavier than the space web and the tethers. In any case, it is good to start with the simplest case, a point mass. The equation of motion for a point mass is:

$$m_c\ddot{\boldsymbol{R}} = \boldsymbol{F} \tag{5.8}$$

where $\ddot{\boldsymbol{R}}$ is the acceleration of the point mass and $\boldsymbol{F}$ is the applied force. Projected along axes $\boldsymbol{e}_1^{(2)}$ and $\boldsymbol{e}_2^{(2)}$ respectively, Eq. (5.8) becomes

$$m_c \left[r_0 \left(\omega^2 \cos\varphi - \dot{\omega} \sin\varphi \right) - \ddot{L} + L \left(\omega + \dot{\varphi} \right)^2 \right] = N \tag{5.9a}$$

$$m_c \left[r_0 \left(\dot{\omega} \cos\varphi + \omega^2 \sin\varphi \right) + 2(\omega + \dot{\varphi})\dot{L} + \left(\dot{\omega} + \ddot{\varphi} \right) L \right] = 0 \tag{5.9b}$$

where $\omega = \dot{\varphi}_1$ is the angular velocity of the centre hub, $\varphi = \varphi_2$ is the deflection angle of the tether relative to the radial direction, L is the length of the tether.

5.2.3 Model 2: deployment of distributed masses

If the mass of the space web or the tethers are of importance, a refined model must be used. This model will depend on the folding pattern and the geometry of the space web during the deployment. This requires the introduction of some additional simplifications. Equation (5.6) is kept unchanged, while Eq. (5.9) is changed. For distributed masses the equations of motion are replaced with:

$$\mathrm{d}m \left[r_0 \left(\omega^2 \cos\varphi - \dot{\omega} \sin\varphi \right) - \ddot{l} + l \left(\omega + \dot{\varphi} \right)^2 \right] = \mathrm{d}N \tag{5.10a}$$

$$\mathrm{d}m \left[r_0 \left(\dot{\omega} \cos\varphi + \omega^2 \sin\varphi \right) + 2(\omega + \dot{\varphi})\dot{l} + \left(\dot{\omega} + \ddot{\varphi} \right) l \right] = 0 \tag{5.10b}$$

where l is the length to mass $\mathrm{d}m$. These equations are then integrated over the area or the length, but first an expression for $\mathrm{d}m$ must be derived. $\mathrm{d}m$ is constant along the length of a tether, whereas it varies linearly along the length of a star arm with the folded web. The equations of motion for some interesting cases follow.

5.2.4 Model 2(a): deployment of a tether

For a tether, the line density ρ_L is constant, and $\mathrm{d}m = \rho_L \mathrm{d}l$. The equations of motion (5.10) describing the deployment of a straight tether, become

$$\rho_L L \left[r_0 \left(\omega^2 \cos\varphi - \dot{\omega} \sin\varphi \right) - \ddot{L} + \frac{L}{2} \left(\omega + \dot{\varphi} \right)^2 \right] = N \tag{5.11a}$$

$$r_0 \left(\dot{\omega} \cos\varphi + \omega^2 \sin\varphi \right) + 2(\omega + \dot{\varphi})\dot{L} + 0.5 \left(\dot{\omega} + \ddot{\varphi} \right) L = 0 \tag{5.11b}$$

As the line density of the tether is constant, the direction from which it is fed out is not important.

5.2.5 Model 2(b): deployment of a circular space web

Melnikov and Koshelev [29] used this model for a circular split reflector. Hedgepeth [13] used a similar model for the LOFT system. Here, it is used for a circular space web coiled around the centre hub. As the tension in the tangential direction is small during the deployment, the model originally used for a split membrane/space web can be used also for a solid membrane or a space web. If the web is fed out from spools on, or coiled around, the centre hub, then each sector have the following line density

$$\rho_L = \frac{2\pi\rho_A}{n}(l + L_R - L) \qquad (0 \le l \le L) \tag{5.12}$$

where ρ_A is the surface density of the space web, R is the radius of the circular space web, L is the deployed length of the sector and $L_R = R - r_0$. The resulting equations of motion thus become

$$\frac{2\pi\rho_A}{n}\left[L\left(L_R - \frac{L}{2}\right)\left(r_0\left(\omega^2\cos\varphi - \dot{\omega}\sin\varphi\right) - \ddot{L}\right) + L^2\left(\frac{L_R}{2} - \frac{L}{6}\right)(\omega + \dot{\varphi})^2\right] = N \tag{5.13a}$$

$$\left(L_R - \frac{L}{2}\right)\left[r_0\left(\dot{\omega}\cos\varphi + \omega^2\sin\varphi\right) + 2(\omega + \dot{\varphi})\dot{L}\right] + L^2\left(\frac{L_R}{2} - \frac{L}{6}\right)(\dot{\omega} + \ddot{\varphi}) = 0 \tag{5.13b}$$

5.2.6 Model 2(c): deployment of the space web using the star pattern

The folding into the star pattern was described in the previous section. The deployment is performed in two steps. The dynamics of the first step, the deployment of the arms, is most important. When the arms are deployed, the deployment of the rest of the net should not pose any major problems according to Melnikov and Koshelev [29].

Step 1: deployment of the arms
A space web is first folded into n identical arms positioned symmetrically around the central hub. The arms can be folded, and then deployed, on spools at the end of the arms, in a zig-zag pattern, or coiled around the centre hub. The line density ρ_L of an arm varies linearly, from zero at the tip of the arm. If the arm is fed out from a spool at the tip of the arm, the line density becomes

$$\rho_L = \frac{2m_w}{nH^2}(H - l) \qquad (0 \le l \le L) \tag{5.14}$$

where H is the length of the arm, i.e. $H = S/2$, l is the position on the arm for a small element of size dl. For a quadratic net, Eq. (5.14) is written as

$$\rho_L = 2\rho_A(H - l) \tag{5.15}$$

The mass of the small element of size dl, to be put in Eqs. (5.10) is

$$\mathrm{d}m = \frac{2m_w}{nH^2}(H - l)\mathrm{d}l \tag{5.16}$$

Attached to the end of each arm is the not yet deployed part of the web with mass

$$m_c = \frac{2m_w}{nH^2}\frac{(H-l)^2}{2} \tag{5.17}$$

The resulting equations of motion become

$$\frac{m_w}{n}\left[r_0\left(\omega^2\cos\varphi - \dot{\omega}\sin\varphi\right) - \ddot{L} + \frac{\left(H^2 + \frac{L^2}{3} - HL\right)}{H^2}L\left(\omega+\dot{\varphi}\right)^2\right] = N \tag{5.18a}$$

$$r_0\left(\dot{\omega}\cos\varphi + \omega^2\sin\varphi\right) + 2(\omega+\dot{\varphi})\dot{L} + \frac{\left(H^2 + \frac{L^2}{3} - HL\right)}{H^2}L\left(\dot{\omega}+\ddot{\varphi}\right) = 0 \tag{5.18b}$$

If the arm is initially coiled around the centre hub, the line density becomes

$$\rho_L = \frac{2m_w}{nH^2}(L-l) \qquad (0 \le l \le L) \tag{5.19}$$

The resulting equations of motion become

$$\frac{2m_w}{nH^2}\left[\frac{L^2}{2}\left(r_0\left(\omega^2\cos\varphi - \dot{\omega}\sin\varphi\right) - \ddot{L}\right) + \frac{L^3}{6}\left(\omega+\dot{\varphi}\right)^2\right] = N \tag{5.20a}$$

$$r_0\left(\dot{\omega}\cos\varphi + \omega^2\sin\varphi\right) + 2(\omega+\dot{\varphi})\dot{L} + \frac{L}{3}\left(\dot{\omega}+\ddot{\varphi}\right) = 0 \tag{5.20b}$$

Step 2: deployment of the web from the arms

The second deployment step can be modelled in different ways, depending on the required accuracy. One very rough model is suggested in [29]. However, the second step is less important to control, or preferably, not necessary to control at all [29]. A more accurate, but still not exact expression, can be achieved by assuming an almost linearly varied line density from $l = L$ to $l = L_{\text{tot}}$ and integrating the surface density over the surface from $l = 0$ to $l = L$. The resulting equations of motion would then become

$$C_1\left(r_0\left(\omega^2\cos\varphi - \dot{\omega}\sin\varphi\right) - \ddot{L}\right) + C_2\left(\omega+\dot{\varphi}\right)2 = N \tag{5.21a}$$

$$C_1\left(r_0\left(\dot{\omega}\cos\varphi + \omega 2\sin\varphi\right) + 2(\omega+\dot{\varphi})\dot{L}\right) + C_2\left(\dot{\omega}+\ddot{\varphi}\right) = 0 \tag{5.21b}$$

where

$$
\begin{aligned}
C_1 &= 2\rho_A H^2 \tan\beta \\
C_2 &= \rho_A \frac{L^3}{3}\left(\frac{\sin\beta}{\cos\beta} + \ln|\tan\frac{\beta}{2} + \frac{\pi}{4}|\right) \\
&+ \rho_L \left(\frac{1-\cos^2\beta}{2\cos^2\beta} + \frac{a}{2}\left(a + \frac{L}{\cos^2\beta}\right) + \frac{\dfrac{L^3}{\cos^3\beta} - a^3}{3\left(a - \dfrac{L}{\cos\beta}\right)}\right)
\end{aligned}
\tag{5.22}
$$

$$\beta = \frac{\pi}{n} \tag{5.23}$$

$$H = \frac{L_w}{2} \tag{5.24}$$

$$\gamma = \arcsin\left(\frac{L}{H}\sin\beta\right) \tag{5.25}$$

$$a = H\frac{\sin(\beta+\gamma)}{\sin\beta} \tag{5.26}$$

$$\rho_L = \rho_A \frac{2(L_{\text{tot}}^2 - L^2)\tan\beta}{-L + \dfrac{L}{2\cos\beta + a/2}} \tag{5.27}$$

$$L_{\text{tot}} = \frac{H}{\tan\beta} \tag{5.28}$$

5.2.7 Deployment of coiled up mass or arm

All the equations of motion derived above can also be used to simulate space webs that are coiled up around the centre hub if the following changes are made: $\omega = \omega + \dot{\varphi}$, $L = L - r_0 \max\left(0, |\varphi| - \frac{\pi}{2}\right)$, $\dot{L} = \mp r_0\dot{\varphi}$, $\ddot{L} = \mp r_0\ddot{\varphi}$ and $\varphi \pm \max\left(|\varphi|, \frac{\pi}{2}\right)$.

5.2.8 Numerical solution of the analytical model

The change of angular momentum, Eq. (5.6), can be used together with the two equations of motion, e.g. Eqs. (5.9), to solve the behaviour of the desired deployment. In order to do this, the three equations must be transformed into a system of nonlinear ordinary differential equations (ODE) for the three unknowns $L(t)$, $\varphi(t)$ and $\omega(t)$. If L is known, then the equation of motion in the radial direction can be used to determine N. This will be the case when a control strategy is used for L or when the tether is fully deployed. Similarly, if ω is controlled the equation of change of angular momentum can be used to determine the torque. The nonlinear ODE system is on the form

$$\dot{\boldsymbol{x}} = \boldsymbol{f}(\boldsymbol{x}) \tag{5.29}$$

where $\boldsymbol{x} = \left(L, \dot{L}, \varphi, \dot{\varphi}, \omega\right)^T$ if there is no control. If a control strategy is used, then the control parameters are omitted.

Finally, the system is solved by a 4th and 5th order Runge-Kutta scheme in MATLAB using the routine `ode45`, an ODE solver that uses error control to determine the integration step size.

5.3 Finite element model

The FE model was implemented in two steps. First, a model with only a mother satellite, four daughter satellites and the tethers connecting them was studied to investigate contact and cable behaviour. Then a more realistic model including a space web, including corner masses, and a central satellite was implemented. The node and element geometry and connectivity are generated by MATLAB for a desired configuration with suitable dimensions and meshing. The equations of motion are then solved in LS-DYNA [22] using the explicit central difference integration method.

In the FE model, the cable behaviour is more accurately modelled than in the analytical model, and perturbations from the ideal symmetric deployment can be investigated. The cables and tethers are modelled with a great number of cable elements, i.e. truss elements with a no-compression material. The main differences compared to the analytical model is that the cables can store elastic energy and that they are not constrained to be straight. Another important difference is that forces can be distributed in directions other than the radial. The simulated space web is coarser than the real space web, but the masses of the cables in the model are determined so that the total masses of the ideal and actual space webs are identical.

The coiling up and coiling off phenomena on the centre hub is important to model in the simulations. Therefore, the centre hub is modelled as a rigid body and not a point mass. The corner masses, however, can be modelled as point masses without loosing any important effects.

Contact phenomena will occur because of the large displacements. The contact between the cables and the rigid bodies, at the centre, is modelled using the kinematic constraint method [15]. This method enables reeling up of the space web without contact forces pushing the web away from the rigid bodies, as would be the case with the more common penalty method. If a cable node is within a small distance ϵ from a satellite surface, then the nodal displacements of the slave nodes (the cables) are transformed, on the global equations level, so that the degrees of freedom normal to the master surface (the centre hub) are eliminated. Impact and release conditions are then imposed to ensure conservation of momentum. The contact condition expires when the relative velocity becomes positive again.

Contact will also occur between the cables in the space web. Here, a nodes to surface variant of the penalty method is used. In the case of penetration, equal and opposite forces are applied. This implies a more elastic behaviour which is more realistic for the cable contact.

Damping has not been included in this work. However, damping may be important, especially if it is used as part of the control strategy or to remove excessive energy. LS-DYNA has routines to deal with damping if this will be required at a later stage.

All the nodes are given initial rotations and initial velocities proportional to the distance from the centre of mass. Torque and external forces can also be applied during the deployment.

Finally, one of the main problems to solve is how to fold the membrane around the centre hub in the most realistic way. A folding pattern where the space web is perfectly folded around a circular hub is impossible to create, since the cables must be modelled straight and with a certain length determined by the total computation cost. Also, to fold the cables near the centre hub is not even trivial in reality. Our solution to this problem was to move the nodes nearest, and inside, the centre hub to the periphery of the hub, see Figure 4.10. Initial contacts between cable elements in the space web were disregarded, since higher priority was focused on coiling the space web as near the centre hub as possible in the initial state.

5.4 Control strategies

The dynamics of the space web deployment using centrifugal forces is dependent on a suitable folding pattern and a smart control strategy. Free deployment would be the easiest way to deploy a space web. However, simulations show that this strategy most likely will lead to the reeling up of the net around the central hub again after the initial reeling off. Therefore, some kind of control strategy is necessary.

The control law should be selected so that the space web ends up in the desired configuration at the end of the deployment, within a required time period and with no undesirable oscillations or entanglement of the system. A stable deployment is obtained if the centrifugal force, which is directed radially, is much greater than the Coriolis and inertial forces [29]:

$$m\omega^2 L \gg 2m\dot{L}\omega \tag{5.30}$$

$$m\omega^2 L \gg m\dot{\omega}L \tag{5.31}$$

or re-written as

$$\gamma = \frac{\omega L}{2\dot{L}} \gg 1 \tag{5.32}$$

$$\frac{\omega^2}{\dot{\omega}} \gg 1 \tag{5.33}$$

A large ratio between the centrifugal and Coriolis forces is the most difficult to achieve, and therefore, γ must be observed.

The deployment can be controlled in different ways. The control parameters could be the torque M, the current length L of the tether, the angular velocity ω of the centre hub or the force N, that resists the deployment of each segment.

Several, more or less successful, control strategies have been described in literature. Salama *et al.* [46] linearly increase the angular velocity ω from 0 to ω_{max} during a time period of Δt, and then keep it constant at ω_{max}, to deploy tethers in the first step of unfolding from a star folding. They also take advantage of an estimated structural damping of about 5%.

Melnikov and Koshelev [29] use the torque and the velocity of the cable being fed out as control parameters to deploy the reflector. They examine two different strategies to adjust the momentum: constant angular velocity and increased momentum as the the angular velocity decreases. Constant momentum is also mentioned, but not investigated.

Constant angular velocity would require a low angular velocity at the end, and therefore the angular velocity would have to be low during the entire process. This would imply increased deployment time, and possibly, difficulties to initiate the deployment because of small centrifugal forces. They also showed that deployment according to this scheme gave an oscillatory behaviour, with partial reeling off and reeling up of the reflector.

Instead, they propose increased momentum as the angular velocity decreases. Using this strategy, they obtain a high initial angular velocity, a low angular velocity in the end, short deployment time and a stable and smooth deployment without entanglements and reeling up of the reflector. More exactly, they propose that the momentum should vary according to the law:

$$M = M_0 \left(1 - \frac{\omega}{\omega_0}\right) \tag{5.34}$$

where M_0 is the initial momentum applied to the centre hub and ω_0 is the initial angular velocity of the centre hub. Melnikov and Koshelev [29] found that a higher value of $K = M_0/\omega_0$ produces a more stable deployment. This statement is also confirmed by our studies.

The deployment velocity $\dot{L}$ could be constant, or changed smoothly or stepwise. Using constant deployment velocity Melnikov and Koshelev [29] reported about increased stability with decreased deployment velocity, which is natural since the Coriolis force decreases. The force N can be obtained using a brake on the spools from where the tethers or space web arms are uncoiled. Preliminary studies with the analytical model have shown that it is not necessary to control the deployment velocity when the arms are coiled around the hub if a momentum according to Eq. (5.34) is applied.

5.5 Results

5.5.1 Validation of the analytical model

First, the accuracy of our analytical model is compared with two more complicated models: a mass-spring network model [32] and a finite element model [33]. The folding and deployment of the simulations by Miyasaki are shown in Figure 2.5. In the analytical model n identical circle sectors were used, where n cancels out because of symmetry, see Eqs. (5.6) and (5.13b).

This example should not be favourable for our simple model, as in this example an unrealistically large hub compared with the membrane size makes the effects near the hub more visible. Furthermore, the folding pattern used here, when the whole web is deployed simultaneously is more difficult to describe with the analytical model than the more controllable stepwise deployment of a star folded web.

However, good agreement between the results of the different models was found, Figure 5.3, which shows that the present analytical model is reliable. Obviously, the influence of the centrifugal forces is much greater than the influence of the elastic forces in this case. This is probably true for most applications where centrifugal forces are used for the deployment. Therefore, the analytical model is sufficiently accurate for initial determination of the system dimensions and the control characteristics.

5.5.2 Deployment of coiled up circular net

Figure 5.4(a) shows data from a simulation of the free deployment of a circular space web with radius 10 m. The web is assumed to be folded as in the example above. Again, the web is first coiled off and then coiled up. The centre hub changes direction during the deployment. Therefore, the web is coiled off not only because of the centripetal acceleration, but also because the web and the hub move in different directions.

If a torque according to the control law in Eq. (5.34) is applied, then successful deployment is obtained. The results when $M_0 = 3\omega_0$ are shown in Figure 5.4(b). The deviation angle of the web compared to the centre hub, φ, is stabilised near 0 at the end of the deployment in the stable case. It is also interesting to compare the quotient between the centrifugal and Coriolis forces, γ, in Figures 5.4(a) and 5.4(b). In the stable case, Figure 5.4(b), $|\gamma|$ increases fast initially, while γ only increases linearly in the unstable case, Figure 5.4(a).

No additional deployment velocity control is required in this case. Applying a torque is not trivial, but probably necessary anyway, since conservation of angular momentum implies a very low angular velocity at the fully deployed state when the web is freely deployed.

5.5.3 Deployment of coiled up star folded web

Previously in this study, quadratic space webs folded in the star pattern have been shown to be of certain interest. The initial configuration of the web coiled around the centre hub is shown in Figure 4.10. Several different deployment simulations of a large space web with side 100 m have been performed. The following data has been used in all the simulations: $S = 100$ m, $m_h = 100$ kg, $r_0 = 6.3$ m, $\rho_A = 1.267 \cdot 10^{-2}$ kg/m^2, $m_c = 10$ kg, $E_{ca} = 180 \cdot 10^9$ Pa, $\rho_{ca} = 1540$ kg/m^3, $A_{ca} = 2.5/0.030 \cdot 1.23 \cdot 10^{-7}$ m^2 and $t = 2.5$ m.

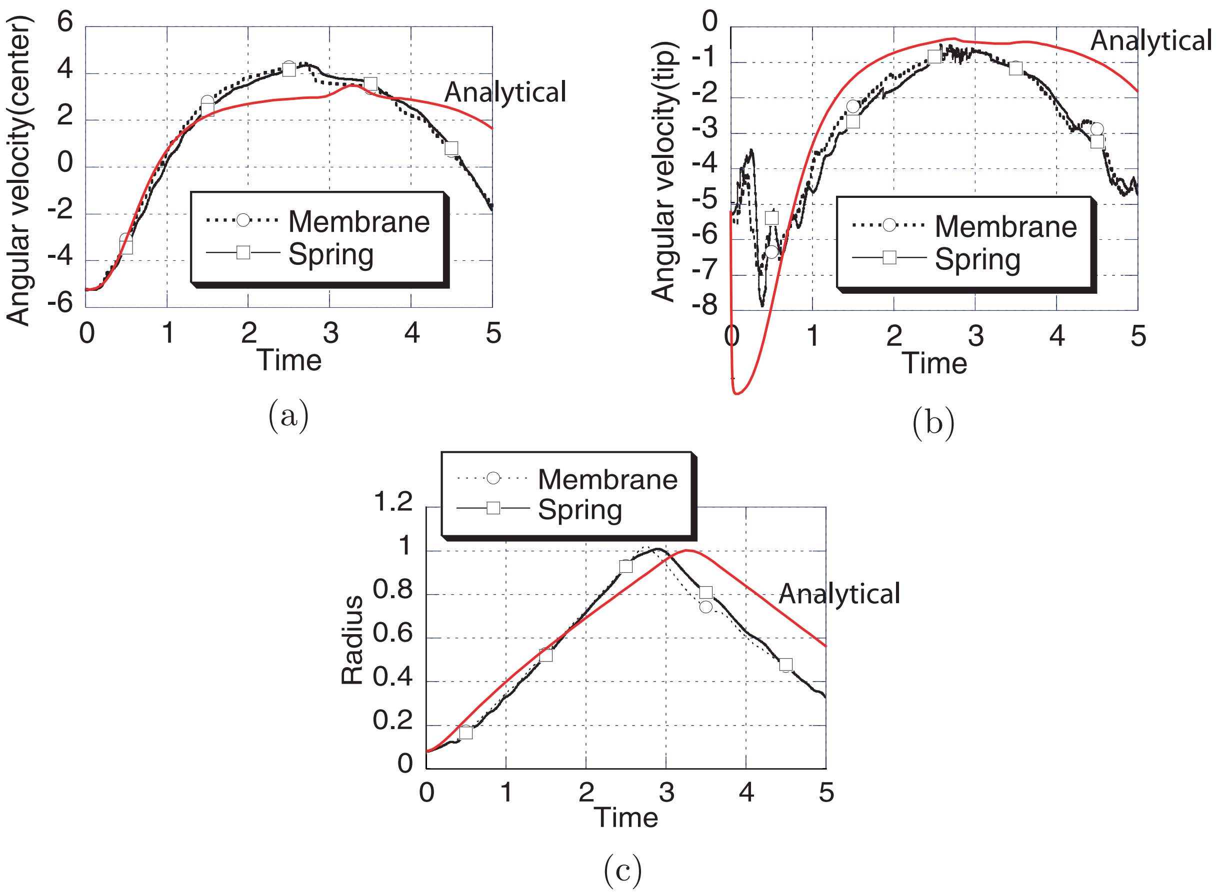

Figure 5.3: Results from a simulation of the deployment of a circular space web using the simple analytical model, a mass-spring network model [32] and a finite element model [33].

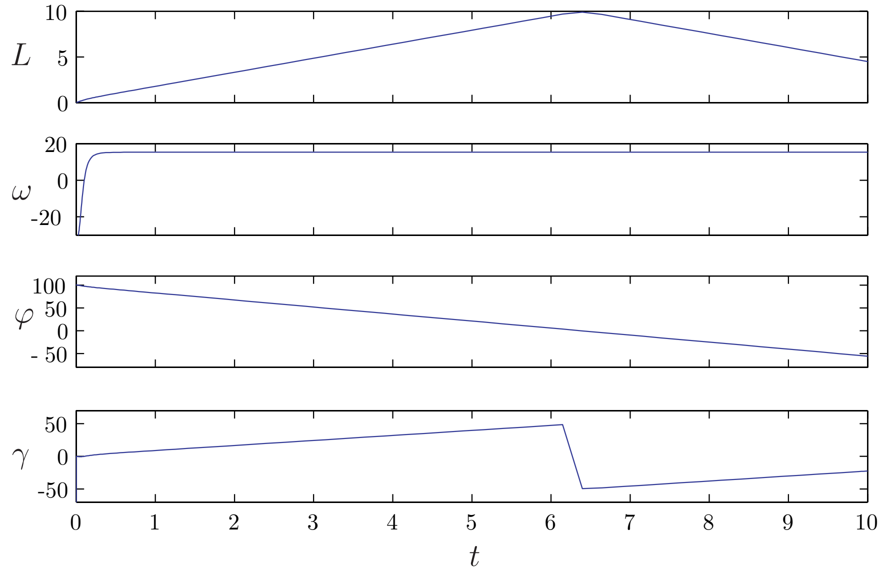

(a) Free

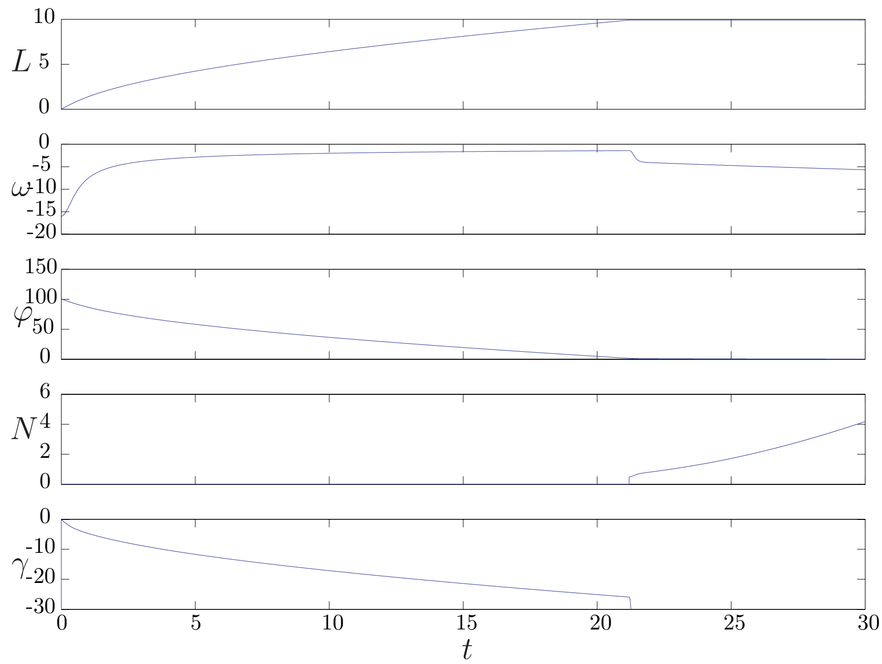

(b) Controlled

Figure 5.4: Analytical solution of the deployment of a circular net with radius 10 m. The free deployment is shown in (a). In (b) A torque, $M = M_0(1 - \frac{\omega}{\omega_0})$, is applied to control the deployment. L is the deployed length of the net. φ is the angle of rotation of the web from the normal to the centre hub and should stabilise near zero at the end of the deployment, γ is the quotient between the centrifugal force and the Coriolis force. $R = 10$ m, $r_0 = 0.1$ m, $m_h = 1$ kg, $\rho_A = 1.267 \cdot 10^{-2}$ kg/m^2, $\omega_0 = 16$ rad/s and $M_0 = 3\omega_0$.

5.5.4 Free deployment of star folded web

First, the free deployment of the whole space web was simulated. The results are shown in Figure 5.5 and 5.6. The arms are deployed first even though no restrictions have been imposed on them to achieve stepwise deployment. But the main problem is the same as for the deployment of the circular web; the web is deployed and then coiled back on the hub again. The coiling off can be described analytically, but not coiling on to the hub.

5.5.5 Free deployment of star arms

To be certain that stepwise deployment will occur, some parts of the web can be held to the centre hub during the deployment of the arms, and then released when the arms are deployed successfully. This course of events also have the advantage that it is easily described analytically. Therefore, the free deployment of only the star arms coiled up around the centre hub was simulated, Figure 5.7. The deployment is initiated by an initial rotational velocity of 8π rad/s on the hub and the web. The star arms are coiled off from the hub, but then coiled up on the centre hub again. The centre hub also change rotational direction during the deployment. The results from the FE simulation can be compared with the analytical model, Figure 5.8. The agreement between the two models is very good for the length of the deployed arm, but not for the rotational velocities.

5.5.6 Controlled deployment of star arms

An applied torque, again using Eq. (5.34), can be used also for the deployment of star arms to stabilise the deployment, see Figure 5.9. Attempts to apply the same torque on the FE model have been performed, but have not been successful due to the sensitivity of correct feedback in the required control strategy. Therefore, a torque that is feedback controlled in the FE model is necessary. This can be performed in the object version of LS-DYNA [22].

The torque applied in the above example is unrealistically high. Hedgepeth used a torque approximately equal to 200 Nm in the simulations of the LOFT [13]. To achieve a stable deployment with applied moments of this order, the deployment velocity must be considerably lower. In reality the hub is smaller, which of course gives lower deployment velocity for a given rotational velocity. Alternatively, it is possible to decrease the initial rotational velocity.

Using a hub with radius 1 m and torque equal to $60\pi \approx 200$ Nm in the analytical model, the deployment characteristics in Figure 5.10 were obtained for different initial rotational velocities ω_0. It can be seen that increased ω_0, i.e. increased deployment velocity, requires higher moment to control the deployment.

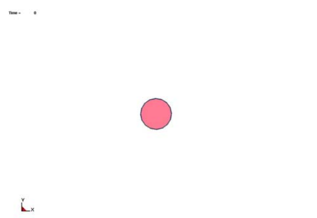

(a) t=0.0

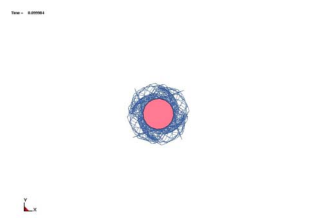

(b) t=0.1

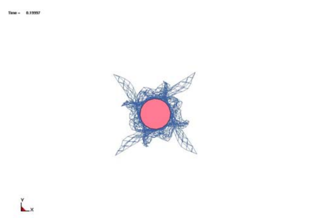

(c) t=0.2

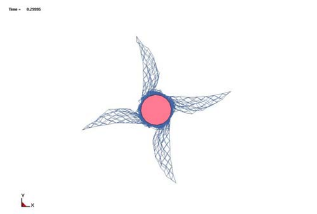

(d) t=0.3

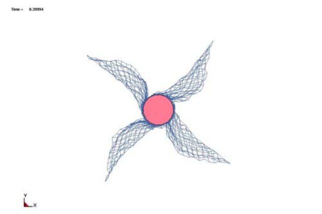

(e) t=0.4

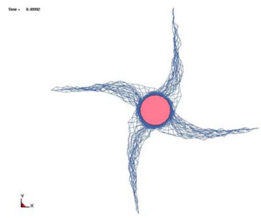

(f) t=0.5

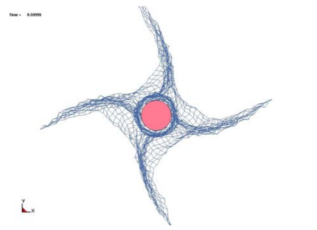

(g) t=0.6

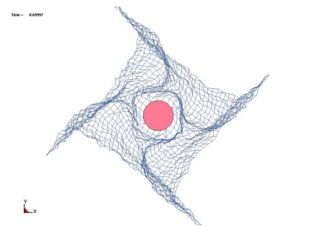

(h) t=0.7

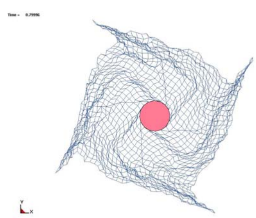

(i) t=0.8

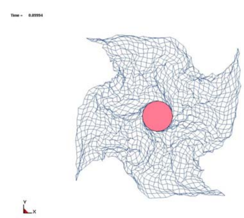

(j) t=0.9

(k) t=1.0

Figure 5.5: The free deployment of a space web folded according to the star pattern and coiled up around the centre hub. The rotation is initiated by an initial rotational velocity $\omega_0 = 8\pi$ rad/s.

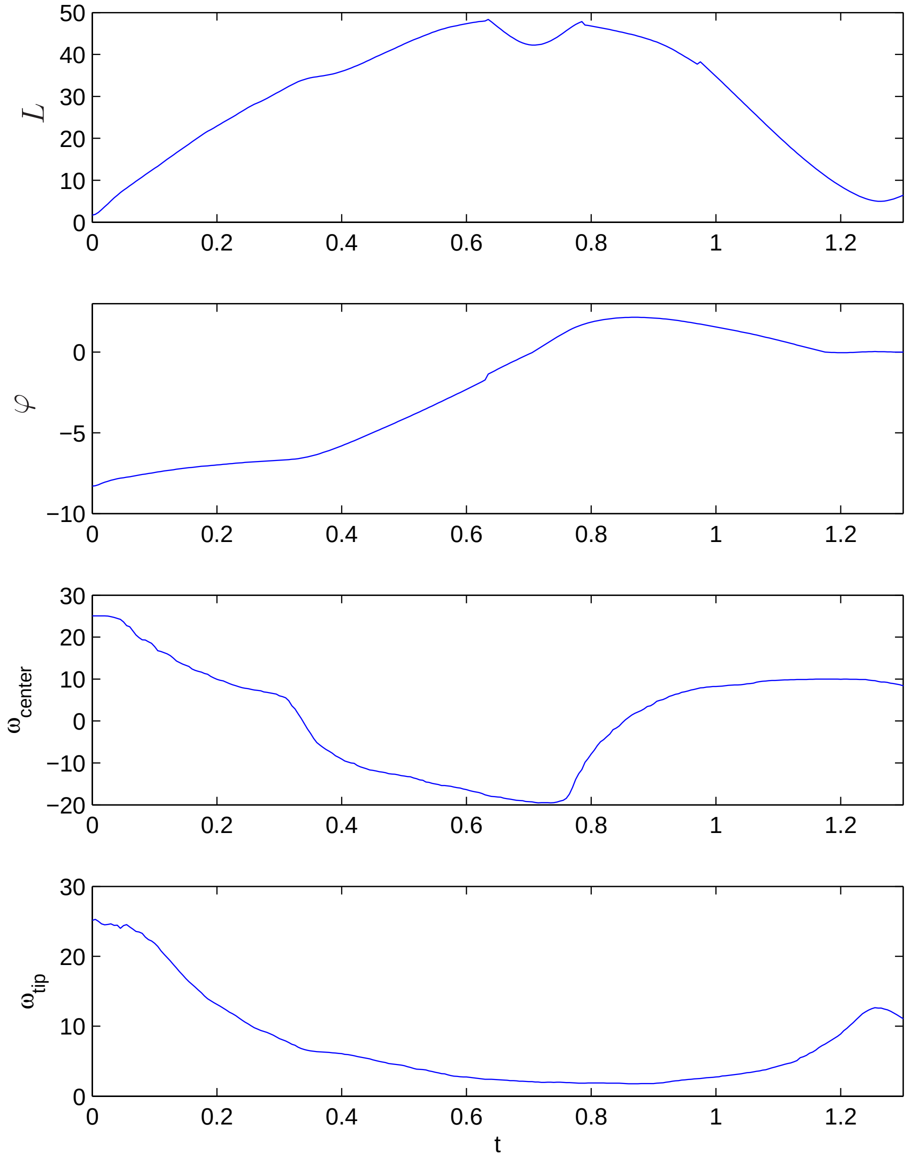

Figure 5.6: The free deployment of a space web folded according to the star pattern and coiled up around the centre hub. The results in the graph have been obtained from the Finite Element model, analytical results cannot be obtained. The four graphs show the length of the deployed arm L, the angular deviation from the radial direction φ, the angular velocity of the inner hub ω_{centre} and the angular velocity of the tip of the arm ω_{tip}.

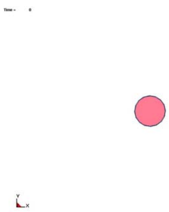

(a) t=0.0

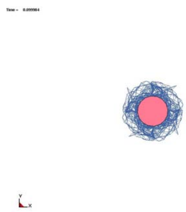

(b) t=0.1

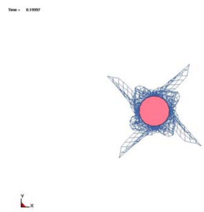

(c) t=0.2

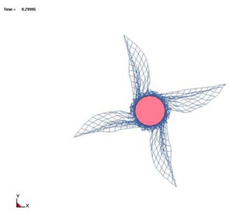

(d) t=0.3

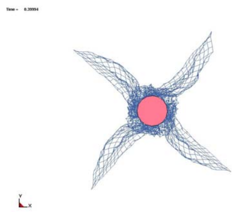

(e) t=0.4

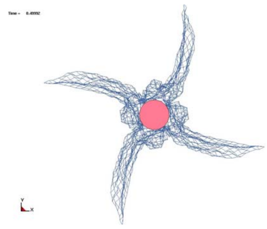

(f) t=0.5

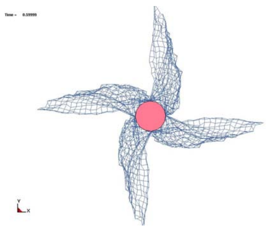

(g) t=0.6

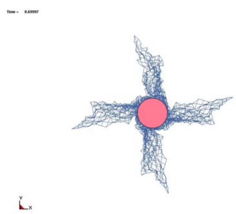

(h) t=0.7

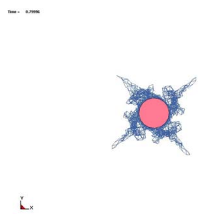

(i) t=0.8

(j) t=0.9

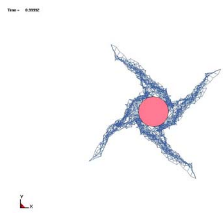

(k) t=1.0

Figure 5.7: The first step of the free deployment, i.e. the deployment of the star arms, of a space web folded according to the star pattern and coiled up around the centre hub. The rotation is initiated by an initial rotational velocity $\omega_0 = 8\pi$ rad/s.

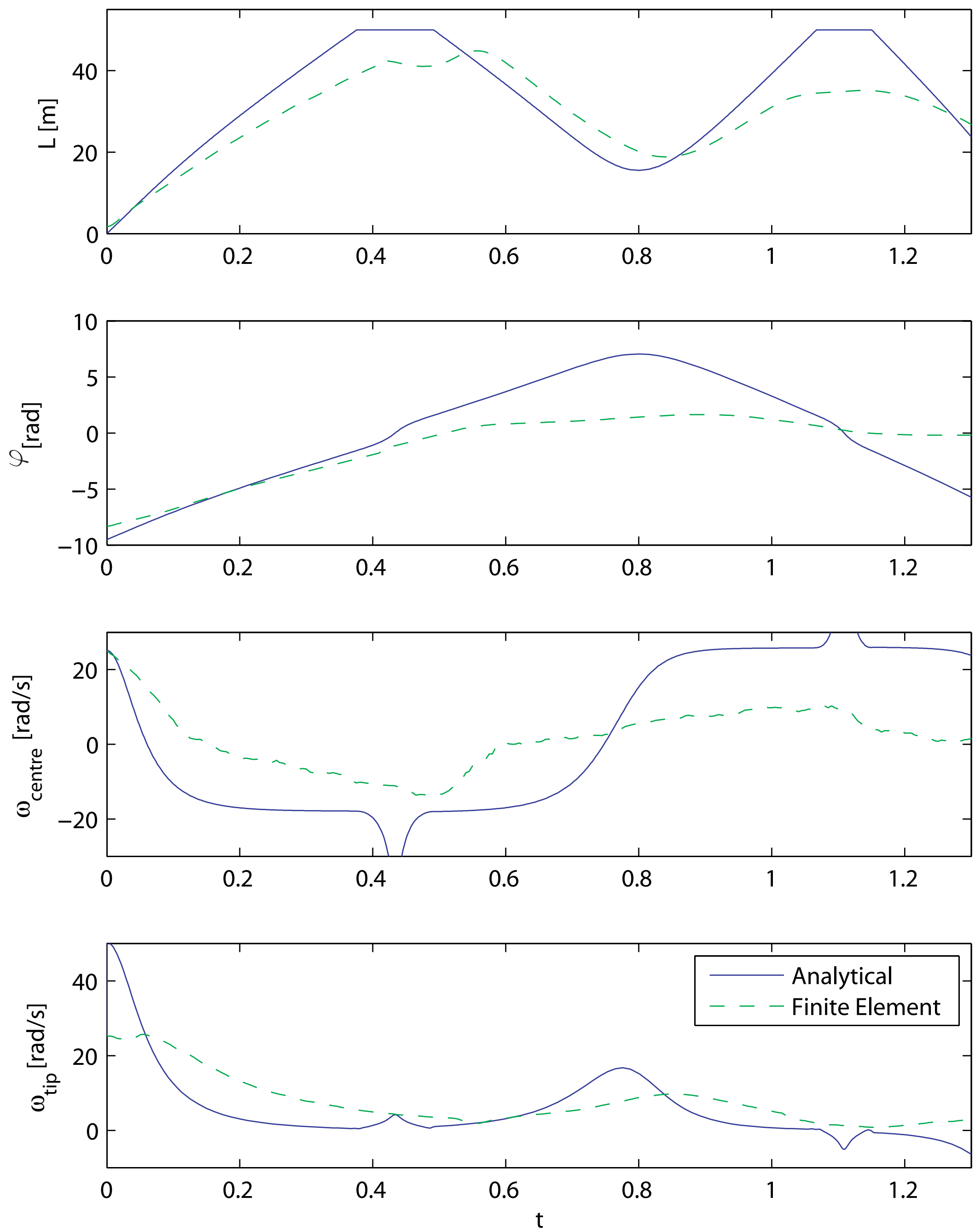

Figure 5.8: The first step of the free deployment, i.e. the deployment of the star arms, of a space web folded according to the star pattern and coiled up around the centre hub. The results obtained with the finite element model can be compared with the results from the analytical model. The four graphs show the length of the deployed arm L, the angular deviation from the radial direction φ, the angular velocity of the inner hub ω_{centre} and the angular velocity of the tip of the arm ω_{tip}. $\omega_0 = 8\pi$ rad/s.

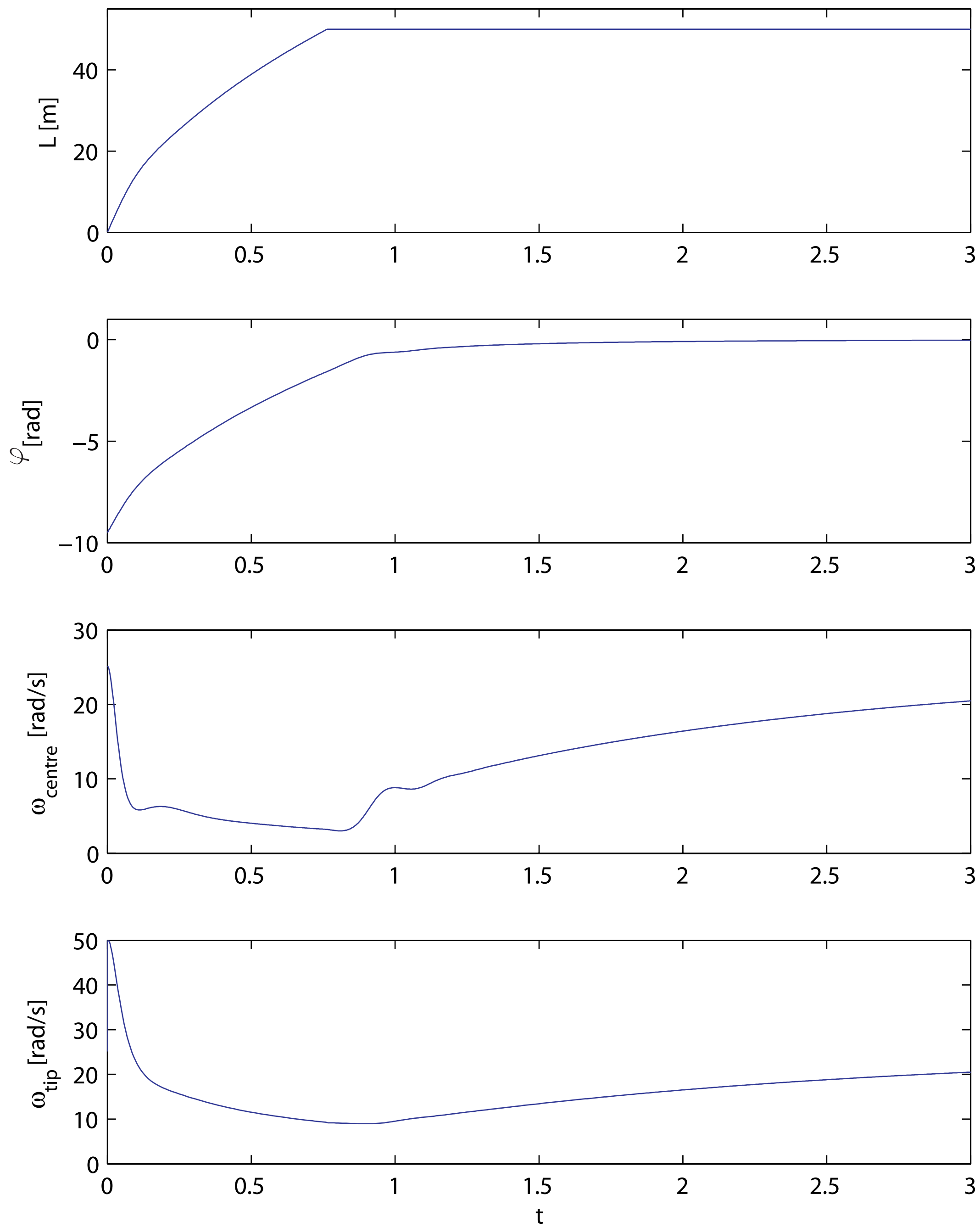

Figure 5.9: The first step of the deployment, i.e. the deployment of the star arms, of a space web folded according to the star pattern and coiled up around the centre hub. A torque is applied according to the control law in Eq. (5.34) with $M_0 = \omega_0 \cdot 10^5$. The four graphs show the length of the deployed arm L, the angular deviation from the radial direction φ, the angular velocity of the inner hub ω_{centre} and the angular velocity of the tip of the arm ω_{tip}.

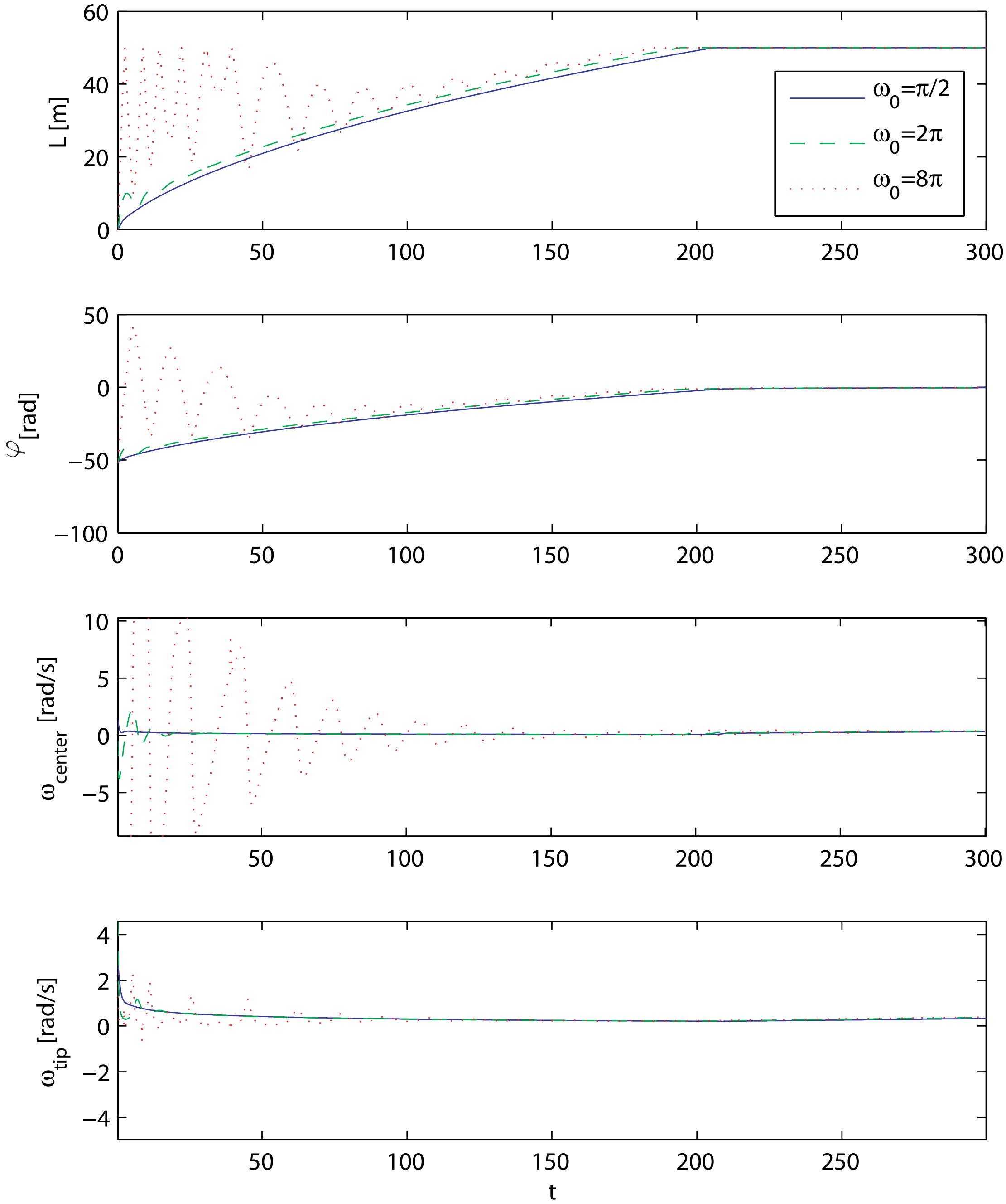

Figure 5.10: The first step of the deployment, i.e. the deployment of the star arms, of a space web folded according to the star pattern and coiled up around the centre hub. A torque is applied according to the control law in Eq. (5.34) with $M_0 = 60\pi$ Nm and $\omega_0 = \pi/2, \pi, 2\pi$ rad/s. The four graphs show the length of the deployed arm L, the angular deviation from the radial direction φ, the angular velocity of the inner hub ω_{centre} and the angular velocity of the tip of the arm ω_{tip}. The stability increases as the initial rotational velocity decreases.

5.5.7 Rotational velocity according to Salama *et al.*

Salama *et al.* [46] propose linearly increasing angular velocity of the inner hub, from 0 at time $t = 0$ to $\omega_{\max}$ at time $t = \Delta t$, and then constant angular velocity $\omega_{\max}$. There is no systematic way to choose these parameters, but using the values $\omega_{\max} = 8\pi$ rad/s and $\Delta t = 2$ s as in the article by Salama *et al.* [46], results in the deployment in Figure (5.11). The arms are coiled off the centre hub, and not coiled back on the hub again. However, there are undesired oscillations in the plane of rotation. The results from the FE simulation can be compared with the results from the analytical model, Figure (5.12). The agreement between the two models is very good during the deployment, but the amplitude and frequency of the above mentioned in-plane oscillations are different.

5.5.8 Differences between the analytical and the FE model

In order to investigate the importance of different effects, simulations were also performed using a stiff material, with Young's modulus $E = 1000E_{\text{Zylon}}$, in the FE model. In the case of linearly increased rotational velocity on the centre hub, Figure 5.13, excellent agreement was obtained between the FE model with stiffer material and the analytical model, Figure 5.14. Therefore, it can be concluded that the difference between the FE model and the analytical model, in this case, is due to the effects of the elasticity in the material when the arms are in tension.

On the other hand, when the same material was used in the case of free deployment simulations, Figure 5.15, no differences were visible compared to when Zylon® was used, Figure 5.8. The reason is of course that the rotational velocity is too small to create enough centrifugal forces to keep the arms in tension. Therefore, the effects of the elasticity is negligible.

Instead, the differences between the two models are explained by the fact that the arms are not straight here, Figure 5.7. However, this is due to the different directions of the rotations of the centre hub and the web, since the centre hub changes direction during the deployment. That is, the coiling off of the arms from the centre hub is not entirely caused by the centripetal acceleration, but also simply because the arms and the hub move in opposite directions. This will not occur during a successful centrifugal force dominated deployment.

The rapid increase, in the analytical model, of the rotational velocity at the tip, from 8π rad/s initially to the double shortly thereafter, is more likely to cause significant differences in interesting realistic cases, Figure 5.15.

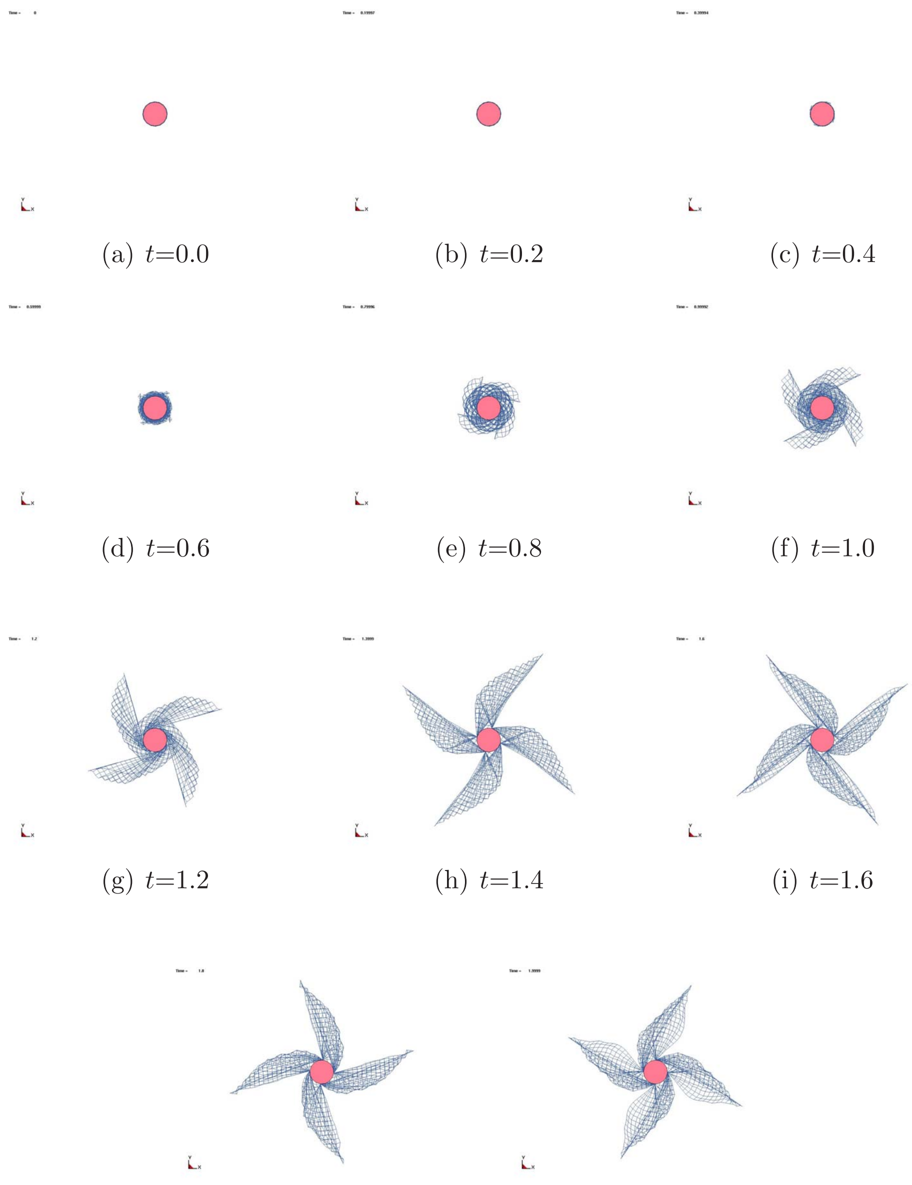

(a) t=0.0 (b) t=0.2 (c) t=0.4
(d) t=0.6 (e) t=0.8 (f) t=1.0
(g) t=1.2 (h) t=1.4 (i) t=1.6
(j) t=1.8 (k) t=2.0

Figure 5.11: The first step of the deployment of a space web folded according to the star pattern and coiled up around the centre hub. The rotational velocity is constrained and varies linearly from 0 at $t = 0$ to 8π rad/s at 2 s.

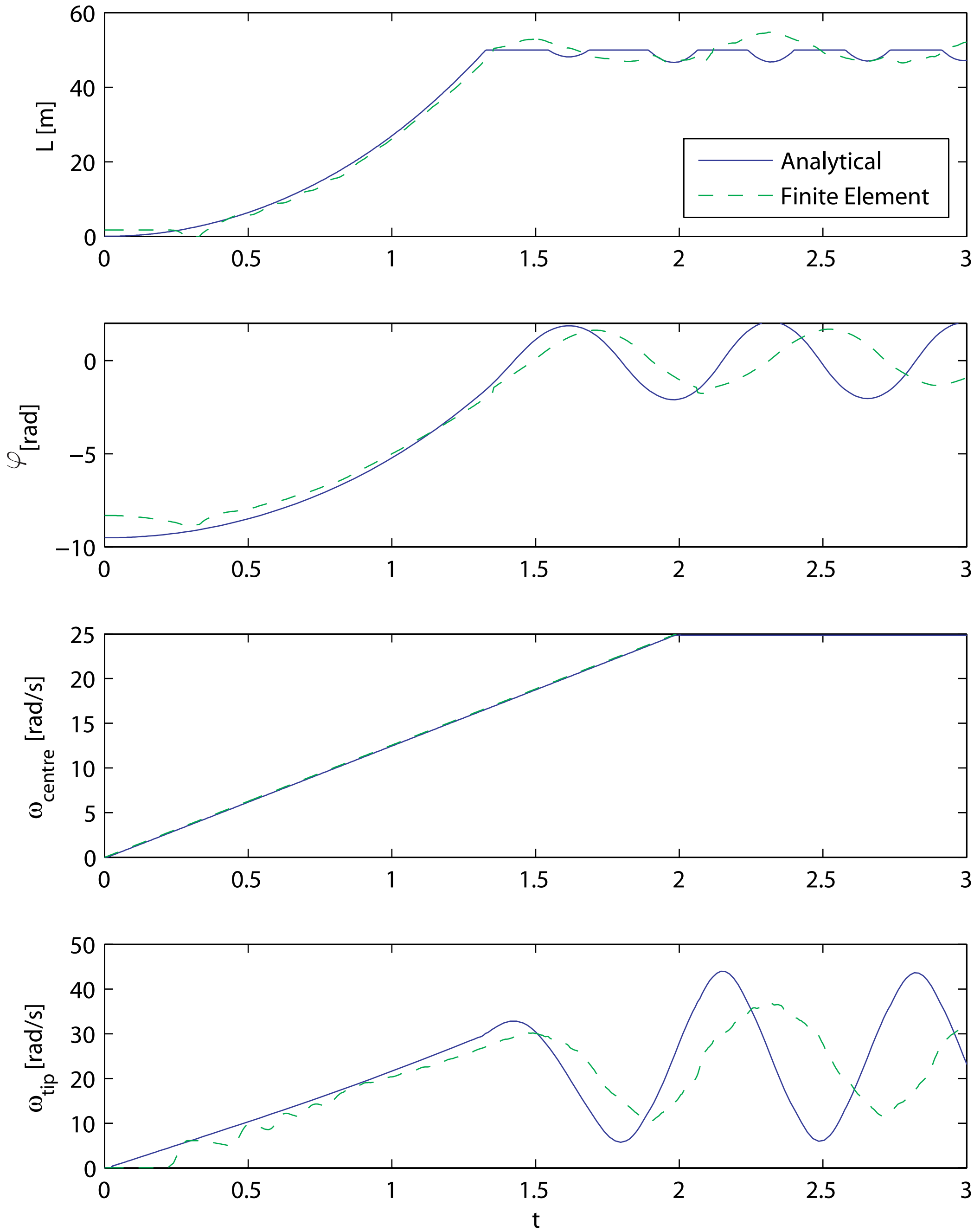

Figure 5.12: The first step of the deployment of a space web folded according to the star pattern and coiled up around the centre hub. The angular velocity is constrained and varies linearly from 0 at $t = 0$ to 8π rad/s at 2 s. The results obtained with the finite element model can be compared with the results from the analytical model. The four graphs show the length of the deployed arm L, the angular deviation from the radial direction φ, the angular velocity of the inner hub ω_{centre} and the angular velocity of the tip of the arm ω_{tip}.

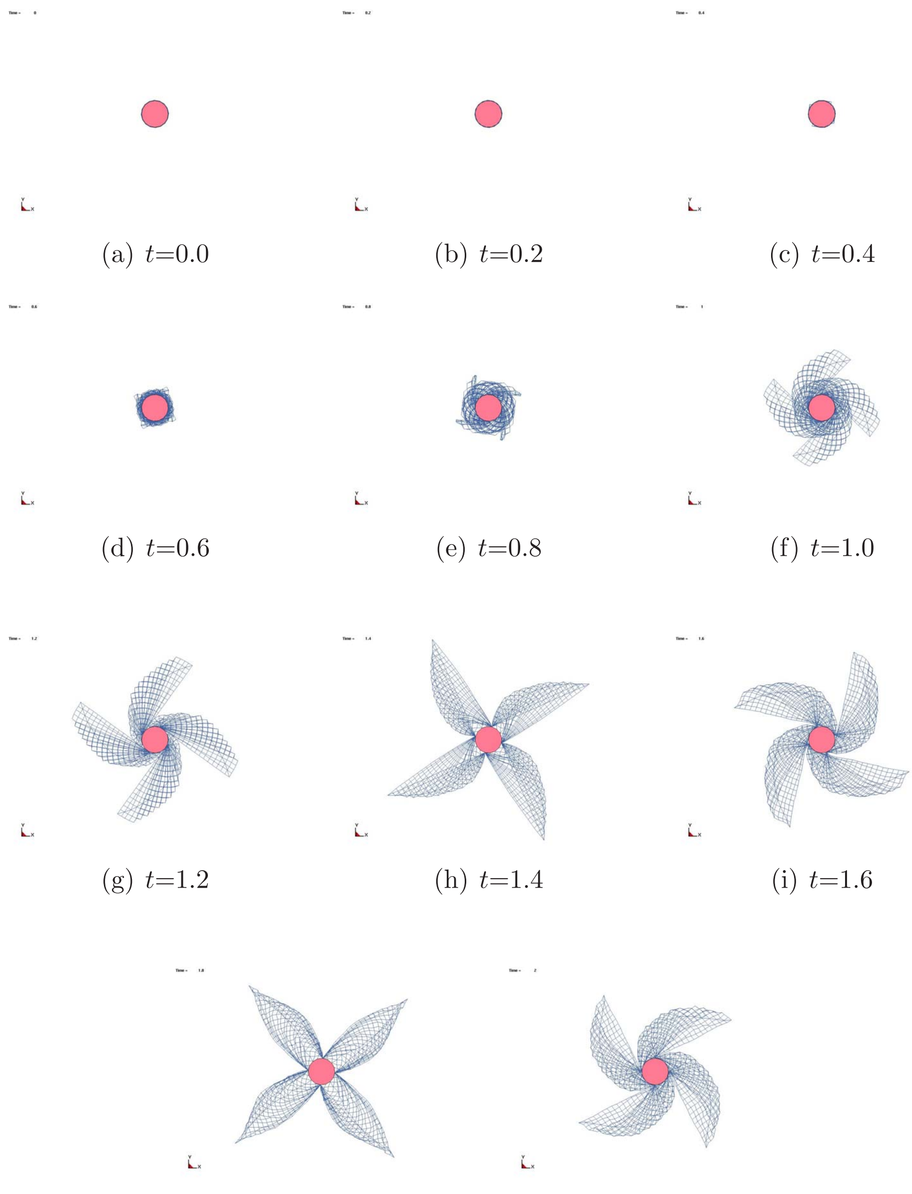

(a) t=0.0 (b) t=0.2 (c) t=0.4
(d) t=0.6 (e) t=0.8 (f) t=1.0
(g) t=1.2 (h) t=1.4 (i) t=1.6
(j) t=1.8 (k) t=2.0

Figure 5.13: The first step of the deployment of a space web folded according to the star pattern and coiled up around the centre hub. The angular velocity is constrained and varies linearly from 0 at $t = 0$ to 8π rad/s at 2 s. The stiffness is 1000 times greater than for Zylon®, see Figure (5.13).

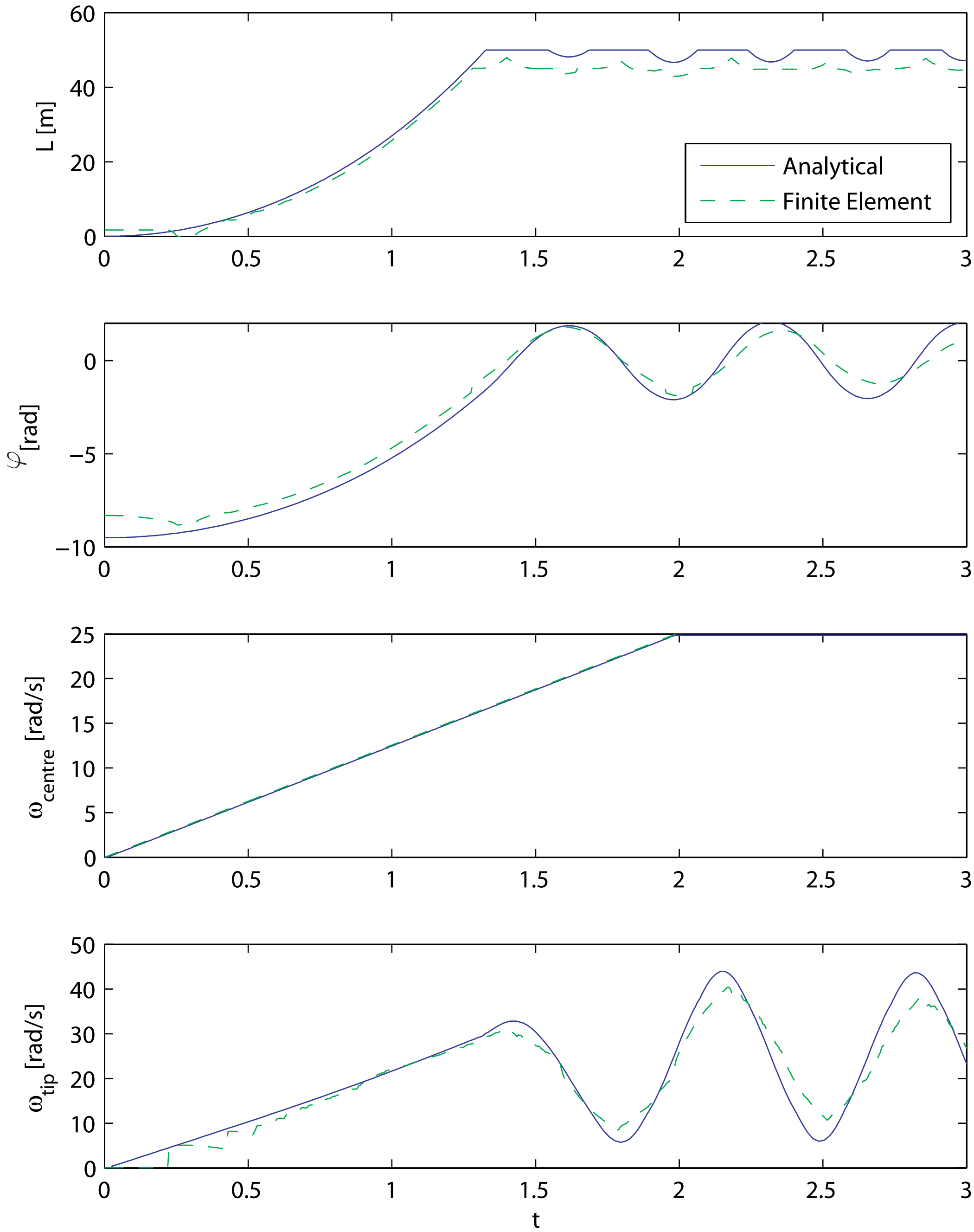

Figure 5.14: The first step of the deployment of a space web folded according to the star pattern and coiled up around the centre hub. The angular velocity is constrained and varies linearly from 0 at $t = 0$ to 8π rad/s at 2 s. The results obtained with the finite element model, with stiff material ($E_{ca} = 1000 E_{\text{Zylon}}$ in Figure (5.14)), can be compared with the results from the analytical model. The four graphs show the length of the deployed arm L, the angular deviation from the radial direction φ , the angular velocity of the inner hub ω_{centre} and the angular velocity of the tip of the arm ω_{tip}.

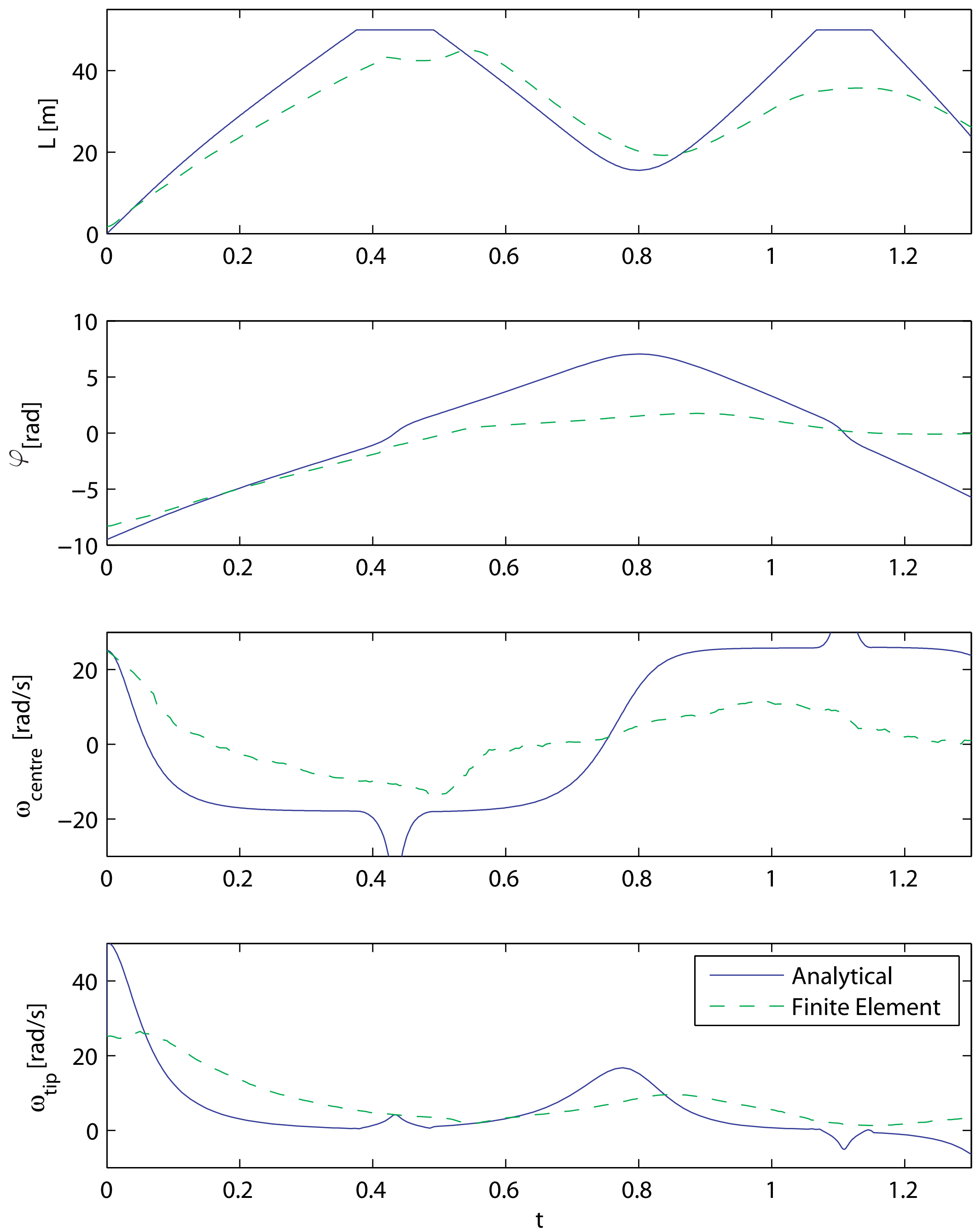

Figure 5.15: The first step of the free deployment of a space web folded according to the star pattern and coiled up around the centre hub. The rotation is initiated by an initial rotational velocity $\omega_0 = 8\pi$ rad/s. The results obtained with the finite element model, with stiff material ($E_{cable} = 1000E_{\mathrm{Zylon}}$), can be compared with the results from the analytical model. The four graphs show the length of the deployed arm L, the angular deviation from the radial direction φ, the angular velocity of the inner hub ω_{centre} and the angular velocity of the tip of the arm ω_{tip}.

Chapter 6

Conclusions

The main conclusions from the respective chapters are as follows.

6.1 Web design

- Only a web with a quadratic mesh topology can be adequately prestressed by spinning. A triangular mesh will contain slack element whereas the hexagonal mesh will be severely distorted.
- If very low element forces in the regions close to the edges can be accepted, it is not required to have curved edges.
- If radial tether must be used to control the deployment, they should have no load bearing function after deployment, since they prevent the web from being fully prestressed.

6.2 Folding pattern

- The two stage star folding pattern makes it possible to deploy the web in two distinctive stages to achieve more control.
- The star folding pattern is also of advantage from a modelling point of view since it can be described with simple equations, mapping the web from the deployed to a fully folded configuration.
- For the second deployment stage, coiling the arms around the hub was chosen in favour of a radial zig-zag scheme. The coiling scheme does require additional tethers that control the deployment rate of the star arms, which is required in the zig-zag scheme.

6.3 Deployment

- An analytical model, originally developed by Melnikov and Koshelev [29] and then slightly modified, and a finite element model implemented in LS-DYNA have been developed. The models have then been used to, mainly, simulate the deployment of space webs folded in star arms and then coiled around a centre hub.

- The analytical and the finite element models produce almost identical results when the arms are straight, i.e. when energy is transferred from the hub to the arms, and a stiff material is used, i.e. no elasticity is involved. When material data for Zylon® is used, then the deployment is still similar, but different oscillatory behaviour occurs after the arms have been fully deployed.

- Both the analytical and finite element models show that free deployment, at least without damping, is not possible.

- To stabilise the deployment, a torque can be applied to the central hub. The torque control law implies that the moment increases when the angular velocity of the hub decreases and vice versa. However, greater maximum moment is required if higher deployment velocity is desired.

Bibliography

[1] Calladine, C. R. Buckminster Fuller's "tensegrity" structures and Clerk Maxwell's rules for the construction of stiff frames. *International Journal of Solids and Structures 14*, 2 (1978), 161–172.

[2] Cook, R. D., Malkus, D. S., Plesha, M. E., and Witt, R. J. *Concepts and applications of finite element analysis*, fourth ed. John Wiley & Sons, New York, 2002.

[3] Denavit, J., and Hartenberg, R. S. A kinematic notation for lower-pair mechanisms based on matrices. *Journal of Applied Mechanics, Transactions of the ASME 22* (1955), 215–221.

[4] Eversman, W. Some equilibrium and free vibration problems associated with centrifugally stabilized disk and shell structures. NASA Contractor Report, NASA CR-1178, 1968.

[5] Furuya, H., Inoue, Y., and Masuoka, T. Concept and deployment characteristics of rotationally skew fold membrane for spinning solar sail. In *Proc. 14th Workshop on Astrodynamics and Flight Mechanics* (Tokyo, July 26–27 2004). Paper A-3.

[6] Furuya, H., Miyazaki, Y. K., and Takeuchi, H. Deployment characteristics of creased membrane for solar sail on geometrical configuration and fold pattern. In *Proc. 44th AIAA/ASME/ASCE/AHS/ASC Structures, Structural Dynamics, and Materials Conf.* (Norfolk, VA, USA, 7–10 April 2003). AIAA 2003-1908.

[7] Gittemeier, K. A., Hawk, C. W., Finckenor, M. M., and Watts, E. Space environmental effects on coated tether materials. In *Proc. 41st AIAA/ASME/SAE/ASEE Joint Propulsion Conf.* (Tucson, AZ, USA, 10–13 July 2005). AIAA-2005-4433.

[8] Grossman, J. Solar sailing: the next space craze? *Engineering & Science*, 4 (2000), 18–29.

[9] Guest, S. D. The stiffness of prestressed frameworks: a unified approach. *International Journal of Solids and Structures 43* (2006), 842–854.

[10] Guest, S. D., and Pellegrino, S. Inextensional wrapping of flat membranes. In *Proc. 1st Int. Conf. on Structural Morphology* (Montpellier, France, 7–11 September 1992), R. Motro and T. Wester, Eds., pp. 203–215.

[11] Hearle, J. W. S., Ed. *High-performance fibers.* Woodhead publishing, Cambridge, UK, 2001.

[12] Hearth, D. P., and Boyer, W. J. Flexibility of space structures makes design shaky. *Aerospace America 23*, 5 (1985), 100–103.

[13] Hedgepeth, J. M. Dynamics of a large spin-stiffened deployable paraboloidal antenna. *Journal of Spacecraft and Rockets 7*, 9 (1970), 1043–1048.

[14] Hedgepeth, J. M. Accuracy potentials for large space antenna reflectors with passive structure. *Journal of Spacecraft and Rockets 19*, 3 (1982), 211–217.

[15] Hughes, T., Taylor, R., Sackman, J., Curnier, A., and Kanoknukulchai, W. A finite element method for a class of contact-impact problems. *Comput. Methods Appl. Mech. Engrg. 8* (1976), 249–276.

[16] Institute for Handling Devices and Robotics, Vienna University of Technology. Sps (solar power satellite)—roby space, September 4 2006. Online Internet: http://www.ihrt.tuwien.ac.at/robyspace/.

[17] Kanemitsu, T., Matsumoto, S., Namba, H., Sato, T., Tadokoro, H., Oura, T., Takagi, K., Aoki, S., and Kaya, N. Self-deployable antenna using centrifugal force. In *IUTAM-IASS Symp. on Deployable Structures: Theory and Applications* (Cambridge, UK, 6–9 September 1998), S. Pellegrino and S. D. Guest, Eds., Kluwer Academic Publishers, Dordrecht, The Netherlands, 2000, pp. 173–182.

[18] Kaya, N., Iwashita, M., Nakasuka, S., Summerer, L., and Mankins, J. Crawling robots on large web in rocket experiment on Furoshiki deployment. In *Proc. 55th Int. Astronomical Congress* (Vancouver, Canada, 4–8 October 2004). IAC-04-R3.

[19] Kyser, A. C. The uniform-stress spinning filamentary disk. NASA Contractor Report, NASA CR-106, 1964.

[20] Kyser, A. C. Uniform-stress spinning filamentary disk. *AIAA Journal 3*, 7 (1965), 1313–1316.

[21] Lai, C.-Y., You, Z., and Pellegrino, S. Shape of deployable reflectors. *Journal of Aerospace Engineering 11*, 3 (July 1998), 73–80.

[22] Livermore software technology corporation. *LS-DYNA Keyword user's manual, version 970.* Livermore, CA, USA, April 2003.

[23] MacNeal, R. H. The Heliogyro: an interplanetary flying machine. Astro Research Corporation, ARC-R-249, March 1967.

[24] MacNeal, R. H. Meteoroid damage to filamentary structures. NASA CR-869, September 1967.

[25] Masumoto, S., Omagari, K., Yamanaka, T., and Matunaga, S. System configuration of tethered spinning solar sail for orbital experiment: numerical simulation and ground experiment. In *Proc. 25th International Symposium on Space Technology and Science (ISTS)* (Kanazawa City, Japan, June 4–11 2006). Paper D-21.

[26] Matunaga, S., Mori, O., Nakaya, K., Iai, M., Omagari, K., and Yabe, H. New spinning deployment method of large thin membranes with tether control. In *Proc. 54th International Astronautical Congress* (Bremen, Germany, September 29–October 3 2003). Paper IAC-03-A.4.01.

[27] Matunaga, S., Yabe, H., Nakaya, K., Iai, M., Omagari, K., and Mori, O. Membrane deployment for spinning formation-flight solar sail. In *Proc. 14th Workshop on Astrodynamics and Flight Mechanics* (Tokyo, July 26–27 2004). Paper A-11.

[28] McInnes, C. *Solar sailing: technology, dynamics and mission applications.* Praxis Publishing, Chichester, UK, 1989.

[29] Melnikov, V. M., and Koshelev, V. A. *Large space structures formed by centrifugal forces*, vol. 4 of *Earth Space Institute Book Series.* Gordon and Breach Science Publishers, India, 1998.

[30] Mitsugi, J., Natori, M., and Miura, K. Preliminary evaluation of the spinning solar sail. In *Proc. 28th AIAA/ASME/ASCE/AHS/ASC Structures, Structural Dynamics, and Materials Conf.* (Monterey, CA, USA, April 1987). AIAA-1987-742.

[31] Miura, K. Method of packaging and deployment of large membranes in space. In *Proc. 31st Int. Astronautical Congress* (Tokyo, 21–28 September 1980). IAF-80-A31.

[32] Miyazaki, Y., and Iwai, Y. Dynamics model of solar sail membrane. In *Proc. 14th Workshop on Astrodynamics and Flight Mechanics* (Tokyo, July 26–27 2004). Paper A-6.

[33] Miyazaki, Y., and Nakamura, Y. Dynamic analysis of deployable cable-membrane structures with adler-mikulas-hedgepeth-00 slackening members. In *Proc. 21st International Symposium on Space Technology and Science* (Tokyo, May 1998). ISTS 98-b-13.

[34] Mori, O., Tsuda, Y., Nishimura, Y., and Kawaguchi, J. Deployment dynamics of clover type solar sail. In *Proc. 14th Workshop on Astrodynamics and Flight Mechanics* (Tokyo, July 26–27 2004). Paper A-5.

[35] Nakashnio, K., and Natori, M. C. Shape characteristics of spin-stabilised structures under microgravity environment. In *Proc. 42nd AIAA/ASME/ASCE/AHS/ASC Structures, Structural Dynamics, and Materials Conf.* (Seattle, WA, USA, 16–19 April 2001). AIAA-2001-1344.

[36] Nakasuka, S., Aoki, T., Ikeda, I., Tsuda, Y., and Kawakatsu, Y. "Furoshiki Satellite"—a large membrane structure as a novel space system. *Acta Astronautica 48*, 5–12 (2001), 461–468.

[37] Nakasuka, S., Funase, R., Nakada, K., Kaya, N., and Mankins, J. C. Large membrane "Furoshiki Satellite" applied to phased array antenna and its sounding rocket experiment. *Acta Astronautica 58* (2006), 395–400.

[38] Nakasuka, S., and Kaya, N. Quick release on experiment results of mesh deployment and phased array antenna by S-310-36, September 4 2006. Online Internet: http://www.isas.ac.jp/e/forefront/2006/nakasuka/.

[39] Onoda, J., Takeuchi, S., and Aoki, Y. A preliminary investigation of a spin-stabilised solar sail. In *Proc. 45th AIAA/ASME/ASCE/AHS/ASC Structures, Structural Dynamics, and Materials Conf.* (Palm Springs, CA, USA, April 19–22 2004). AIAA 2004-1511.

[40] Pellegrino, S. Structural computations with the singular value decomposition of the equilibrium matrix. *International Journal of Solids and Structures 30*, 21 (1993), 3025–3035.

[41] Pellegrino, S., Ed. *Deployable Structures*, vol. No. 412 of *CISM Courses and Lectures*. Springer-Verlag, 2001.

[42] Phillystran, Inc. Phillystran strength members Zylon (PBO), 5 July 2006. Online Internet: http://www.phillystran.com/190.pdf.

[43] Pickett, W. L., Pratt, W. D., Larson, M. L., Redlin, D. M., and Hinkle, J. D. Testing of centrifugally deployed membrane dynamics in an ambient ground environment. In *Proc. 43rd AIAA/ASME/ASCE/AHS/ASC Structures, Structural Dynamics, and Materials Conf.* (Denver, CO, USA, 22–25 April 2002). AIAA 2002-1241.

[44] Robbins, Jr., W. M. The feasibility of an orbiting 1500-meter radio telescope. NASA CR-792, Astro Research Corporation, 1967.

[45] Robbins, Jr., W. M. Spinning paraboloidal tension networks. NASA CR-873, Astro Research Corporation, 1967.

[46] Salama, M., White, C., and Leland, R. Ground demonstration of a spinning solar sail deployment concept. *Journal of Spacecraft and Rockets 40*, 1 (2003), 9–14.

[47] Scheel, H. W. Space-saving storage of flexible sheets. United States Patent, US 3,848,821, November 19, 1974.

[48] Schek, H. The force densities method for form finding and computation of general networks. *Comput. Methods Appl. Mech. Engrg. 3* (1974), 115–134.

[49] Schuerch, H. U., and Hedgepeth, J. M. Large low-frequency orbiting radio telescope. NASA Contractor Report, NASA CR-1201, October 1968.

[50] Seely, L. G., Zimmerman, M., and McLaughlin, J. The use of Zylon fibers in ULDB tendons. *Advances in Space Research 33* (2004), 1736–1740.

[51] Simmonds, J. G. Axisymmetric, transverse vibrations of a spinning membrane clamped at its center. *AIAA Journal 1*, 5 (1963), 1224–1225.

[52] Souza, D. M. *Space sailing.* Lerner Publications, Minneapolis, USA, 1993.

[53] Tanami, T., and Hangai, Y. Direct and modal analyses for shape-finding of unstable structures. In *Spatial, Lattice and Tension structures, Proc. IASS-ASCE Int. Symp. 1994* (Atlanta, USA, 1994), J. F. Abel, J. W. Leonard, and C. U. Penalba, Eds., ASCE, pp. 714–723.

[54] Thomson, M. W. The AstroMesh deployable reflector. In *Proc. 5thh Int. Mobile Satellite Conf. (IMSC '97)* (Pasadena, CA, USA, 16–18 June 1997), pp. 393–398.

[55] Tibert, A. G. *Deployable Tensegrity Structures for Space Applications.* PhD thesis, Royal Institute of Technology, Stockholm, Sweden, 2002.

[56] Tibert, A. G. Optimal design of tension truss antennas. In *Proc. 44th AIAA/ASME/ASCE/AHS/ASC Structures, Structural Dynamics, and Materials Conf.* (Norfolk, VA, USA, 7–10 April 2003). AIAA-2003-1629.

[57] Tibert, G. *Numerical analyses of cable roof structures.* Licentiate thesis, Royal Institute of Technology, Stockholm, Sweden, 1999.

[58] Toyobo Co. Ltd. PBO fiber Zylon (technical information, revised 2005.6), 5 July 2006. Online Internet: http://www.toyobo.co.jp.

[59] Tsuda, Y., Nakaya, K., Mori, O., and Yamamoto, T. Microsatellite-class solar sail demonstrator — mission design and development status. In *Proc. 25th International Symposium on Space Technology and Science (ISTS)* (Kanazawa City, Japan, June 4–11 2006). Paper K-37.

[60] Underwood, P. Dynamic relaxation. In *Computational Methods for Transient Analysis* (1983), T. Belytschko and T. J. R. Hughes, Eds., vol. 1, North-Holland, pp. 245–265.

[61] Watanabe, H., Natori, M. C., Okuizumi, N., and Higuchi, K. Folding of a circular membrane considering the thickness. In *Proc. 14th Workshop on Astrodynamics and Flight Mechanics* (Tokyo, July 26–27 2004). Paper A-4.

[62] Wright, J. L. *Space sailing.* Gordon and Breach Science Publications, Philadelphia, USA, 1992.

[63] Young, W. C., and Budynas, R. G. *Roark's formulas for stress and strain*, 7th ed. McGraw-Hill, Singapore, 2002.